

**BAND GAP ENGINEERING OF TiO₂
NANOTUBES FOR PHOTOCATALYTIC
HYDROGEN GENERATION**

By

PREETHI L K

Enrolment No.: PHYS 02 2012 04 008

Indira Gandhi Centre for Atomic Research, Kalpakkam, India.

*A thesis submitted to the
Board of Studies in Physical Sciences*

*In partial fulfillment of requirements
for the Degree of*

DOCTOR OF PHILOSOPHY

of

HOMI BHABHA NATIONAL INSTITUTE



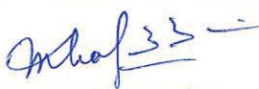
OCTOBER, 2017

Homi Bhabha National Institute

Recommendations of the Viva Voce Committee

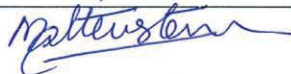
As members of the Viva Voce Committee, we certify that we have read the dissertation prepared by **Preethi L K** entitled "**Band Gap Engineering of TiO₂ Nanotubes for Photocatalytic Hydrogen Generation**" and recommend that it may be accepted as fulfilling the thesis requirement for the award of Degree of Doctor of Philosophy.

Chairman - Prof. M. Kamruddin



Date: 25/5/18

Guide / Convener - Dr. Tom Mathews



Date: 25/05/2018

External Examiner – Dr. N Sandhyarani



Date: 25/5/2018

Member 1- Dr. M. Joseph



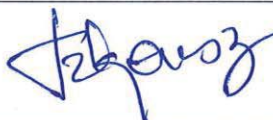
Date: 25/5

Member 2- Dr. Arun K Prasad



Date: 25/5/2018

Technological Advisor - Dr. R. Krishnan



Date: 25/05/2018

Final approval and acceptance of this thesis is contingent upon the candidate's submission of the final copies of the thesis to HBNI.

I/~~We~~ hereby certify that I/~~we~~ have read this thesis prepared under my/~~our~~ direction and recommend that it may be accepted as fulfilling the thesis requirement.

Date: 25/05/2018

Place: IGCAR, Kalpakkam



Guide

STATEMENT BY AUTHOR

This dissertation has been submitted in partial fulfillment of requirements for an advanced degree at Homi Bhabha National Institute (HBNI) and is deposited in the Library to be made available to borrowers under rules of the HBNI.

Brief quotations from this dissertation are allowable without special permission, provided that accurate acknowledgement of source is made. Requests for permission for extended quotation from or reproduction of this manuscript in whole or in part may be granted by the Competent Authority of HBNI when in his or her judgment the proposed use of the material is in the interests of scholarship. In all other instances, however, permission must be obtained from the author.



Preethi L K

DECLARATION

I, hereby declare that the investigation presented in the thesis has been carried out by me. The work is original and has not been submitted earlier as a whole or in part for a degree / diploma at this or any other Institution / University.


Preethi L K

LIST OF PUBLICATIONS ARISING FROM THE THESIS

Publications in Journals / Preprints

1. “Marginally hydrogenated triphasic TiO₂ nanotubes for efficient charge transfer towards effective visible light photocatalytic hydrogen generation”
Preethi L. K., Tom Mathews, Lukasz Walczak, Chinnakonda S. Gopinath.
Energy Technology, (2017) 1 - 10.
2. “Band alignment and charge transfer pathway in three phase anatase-rutile-brookite TiO₂ nanotubes : An efficient photocatalyst for water splitting”
Preethi L. K., Tom Mathews, Mangla Nand, S. N. Jha, Chinnakonda S. Gopinath.
Applied Catalysis B: Environmental, (2017), 218, 9 -19.
3. “Nitrogen doped anatase-rutile heterostructured nanotubes for enhanced photocatalytic hydrogen production: promising structure for sustainable fuel production”
L.K. Preethi, R. P. Antony, T Mathews, S.C.J. Loo, Lydia H. Wong, S. Dash.
International Journal of Hydrogen Energy, (2016), 41, 5865-77.
4. “A study on doped heterojunctions in TiO₂ nanotubes: An efficient photocatalyst for solar water splitting”
Preethi L. K., Rajini P Antony, Tom Mathews, Lukasz Walczak, Chinnakonda S. Gopinath.
Scientific Reports, (2017), 7, 1 -15.
5. “Rutile to brookite phase transformation in triphasic TiO₂ nanotubes synthesis: A detailed comparison on their photocatalytic water splitting”
Preethi L. K., Tom Mathews, Chinnakonda S. Gopinath.
Communicated to Nature Catalysis

Conferences

1. “Phase tuned TiO₂ nanotubes for enhanced photocatalytic hydrogen generation: Anatase → Anatase-Rutile → Anatase-Rutile-Brookite” (*Poster presentation*)
Preethi. L. K. and T Mathews, 45th Jaszowiec International School and Conference on the Physics of Semiconductors, 18-24 June (2016), Szczyrk, Poland.
2. “Band gap engineering of anatase-rutile TiO₂ nanotubes for potential application in photocatalytic water splitting” (*Poster presentation*)

Preethi. L. K., Rajini P Antony, Tom Mathews and S. Dash, *Emerging Trends in Advanced Functional Materials (ETA FM)*, 18-21 Jan (2016), Institute of Physics (IOP), Bhubaneswar, India.

Others Publications (Not included in Thesis)

1. “Optical transmittance and electrocatalytic efficacy of chronoamperometrically and chrono-potentiometrically deposited platinum electrodes, towards tri-iodide ion reduction, for DSSC application”

L.K. Preethi, Rajini P Antony, Tom Mathews, S. Dash, A. K. Tyagi.
Journal of Nanoscience and Nanotechnology, (2016), 1, 10087-96.

2. “Enhanced electrocatalytic activity of Pt-TiO₂ nanotube composites towards methanol oxidation in acid and alkaline media”

L.K. Preethi, Rajini P Antony, Tom Mathews, S. Dash, A. K. Tyagi.
Journal of Nanoscience and Nanotechnology, (2016), 16, 10117-24.

3. “Efficient electrocatalytic performance of thermally exfoliated reduced graphene oxide-Pt hybrid”

Rajini P A, L K Preethi, Bhavana Gupta, Tom Mathews, S. Dash, A K Tyagi.
Materials Research Bulletin, (2015), 70, 60 – 67.

Others Conferences (Not included in Thesis)

1. “High temperature ammonia annealed TiO₂ nanotubular arrays: Synthesis, characterization and Mott-Schottky analysis for potential application in photocatalytic water splitting” (*Oral Presentation*)

L.K. Preethi, Rajini P Antony, Tom Mathews, S. Dash and A. K. Tyagi,
International Conference on Nanomaterials and Nanotechnology (Nano15), 7-10 Dec (2015), KSR Campus - Tiruchengode, India.

2. “High temperature ammonia annealed TiO₂ nanotube powders: Synthesis, characterization and Mott-Schottky analysis for potential application in photocatalytic water splitting” (*Oral Presentation*)

L.K. Preethi, Rajini P Antony, Tom Mathews, S. Dash and A. K. Tyagi,
International Conference on Electron Microscopy & XXXVI annual meeting of Electron Microscope Society of India (EMSI), 8 – 10 July (2015), Mumbai, India.

L. K. Preethi
(PREETHI, L. K.)

**Dedicated
To
My Daddy & Amba..**

Acknowledgements

It would not have been possible for me to prepare my doctoral thesis without the support of a number of wonderful people. I thank all, for making my thesis possible today.

First and foremost, I thank all my teachers who come across in my life as each one of them imparted in one way or the other, the essence of education in varying energies, with which I have come to this level.

I would like to express my deep sense of gratitude to my research supervisor **Dr Tom Mathews**, for his apt guidance, constant support, friendly and easy going nature which made my PhD days wonderful and stress-free. I owe him sincerely for rendering me freedom in thinking and executing my own research ideas, for always being available to any length of discussions, for being helpful at any circumstances, for his simple teaching and kindness. Like the flowers blossom when the sun shines, my mind untangles from complex knot to a simple thread after every discussion with Dr Tom, as he delineates any sort of problem, simple to the core.

I do not have words to render thanks to my senior, **Dr. Rajini P Antony**, for her immense love and support till this day. I owe her sincerely for shaping my PhD carrier as a mentor and I surrender all my credits to her.

I owe **Dr. Sitaram Dash**, Former Head, Thin Films & Coatings Section, and head SND IGCAR, for his consistent encouragement with dutiful management in providing me the necessary infrastructure and resources to accomplish my research work effortlessly. I specially thank him for his simplicity, sincerity and professional attitude that deeply influenced me.

I would like to extend my heartfelt thanks to **Dr A K Bhaduri**, Director, IGCAR, **Dr. S A V Satya Murty** and **Dr. P R Vasudeva Rao**, former Directors of IGCAR for allowing me to pursue research in this prestigious institution and for providing favorable circumstances to research scholars

I thank **Dr. G. Amarendra**, Director, Materials Science Group, **Dr. Sandip Dhara**, Head and **Dr A K Tyagi**, Former Head, Surface and Nanoscience Division, for supporting and motivating research scholars like me throughout our PhD career. My special thanks to **Dr. Sandip Dhara** for extending the Raman and Photoluminescence spectroscopic facilities.

I would like to thank **Dr. N V Chandra Shekar**, Dean, and **Dr. B V R Tata**, Former Dean, Physical Sciences, HBNI, for their constant support and evaluation of my research progress.

I wish to sincerely thank the Doctoral Committee Chairman **Dr. M Kamruddin** and the members **Dr R Krishnan**, **Dr Arun K Prasad** and **Dr. M Joseph**, for evaluating my doctoral research periodically and providing

valuable suggestions which greatly helped me to enhance the quality of my research work.

I wish to whole heartedly thank **Dr. Aji Kumar, Shri Magudapathy, Dr. S Kalavathy, Dr. Sarguna, Dr. Amirtha pandian and Mrs. Clinsha** of IGCAR, **Mr. Manglanand** of RRCAT, **Dr. Walszak Lukas** of Prevac Poland, for extending the facilities for my research work without them the dissertation would have been impossible.

I am deeply grateful to **Dr. C S Gopinath**, Head, Catalysis division, National Chemical Laboratory, Pune, for offering me a godsend opportunity to work on photocatalytic water splitting reactor at the most needed time. I owe him for his constant support, extended slot allocation, timely correction of the manuscripts and fruitful suggestions. I also wish to thank his students for helping me in using the photocatalysis set up. I am also very much delighted to thank his wife **Mrs. Jothi Gopinath** for her kindness and friendship. I could never forget those pleasant times being with them undifferentiated on evenings during every trip to NCL, Pune, which helped me a lot to relieve from experimental stress. I wish to thank **Mr. Ram Sundar**, NCL for his brotherly support and care without him the stay in NCL would have been troublesome.

I would like to thank **Dr. S N Jha** for providing synchrotron facility to characterize my sample which resulted in high impact publications.

I owe **Dr M Saibaba**, for his support to research scholars at each stage of their PhD carrier. I specially thank him for facilitating me with a stay in family quarters. The guidance, care, encouragement and affection given during the past five years by **Dr. S Ilango, Dr. R Ramaseshan, Dr. R Krishnan, Dr. Gomathi Natarajan, Mr. P A Manoj Kumar, Dr S Tripurasundari** is acknowledged with gratitude.

I specially thank my friends and their families: **Srinivasan** and his mother; **Rama Balaji** and her Mother in law for helping me in numerous ways during my stay at Kalpakkam.

I wish to express my appreciation to all my friends and colleagues in IGCAR, especially **Srinivasan, Sivadasan, Yadagiri, Sumathi G, Sumathi V, Prema, Sravanthi, Kamali, Amutha, Sathya, Santanu Parida, Raktima Basu, Binay, Subrato Ghosh, Anil Kumar, Padmalochan Panda, Jeyanthi, Reshmi, Vairavel, Lakshmanan, Irshad, Shraddha, Radhikesh, Sivakumar, Ashok, Jose Martina** and many for their friendship, valuable suggestions, consideration and services which made my days beautiful in IGCAR. Their timely help during my research work will remain green in my mind for ever.

I wish to thank various offices in IGCAR and its staff, All Cafeterias, cosmetic workers, watchmen, security personals, JRF Enclave office, GSO, DAE Hospital, DAE Bus drivers etc for providing me a clean, safe and comfortable

stay in Kalpakkam and IGCAR. Your services are ever remembered at the bottom of my heart.

There is no formality of thanks between close friends. Hence I wish to cherish the moments I had with my best friend **Raghavendra**, whose shoulders were always there ready to lean on during my ups and downs of my doctoral research carrier. Through him I got introduced to many new friends, the moments with them are always relished. I owe **Janani**, my soul mate, for shaping my character, pointing out my abilities in most difficult junctures and teaching me the practicalities of life. Most of all, I owe for all her sacrifices which cannot be repaid by any means.

Even though I thank tons of wonderful souls, the acknowledgements would not satisfy me unless and until I mention some special individuals here who are my family members. Today what I am now is because of my parents **Kuppusamy** and **Jothi** who are my backbones. I will never have the words of appreciation for their selfless love, support, patience, encouragement and many other endless sacrifices. At this point of time, I would like to express my sincere and deep gratitude to my husband **Madhanmohan** for his love, enormous adjustments and unconventional attitude, co-operative and friendly gestures, which made my research life smooth. I wish to remember my brothers **Hari** and **Prem**, my grandparents **Chandra** (Late) and **Muthukrishnan**, and other members of my family at this point of time, for their unconditional love and blessings. I hope this thesis would make them proud.

Finally I thank one and all who have helped me directly or indirectly for the successful completion of my thesis.

CONTENTS

	Page No.
SYNOPSIS	I
LIST OF FIGURES	X
LIST OF TABLES	XIII
LIST OF ABBREVIATIONS	XIV
CHAPTER 1 Introduction	1
1.1 Present Scenario in Energy production	3
1.2 Photocatalysis	4
1.2.1 Artificial photosynthesis	4
1.2.2 Reaction mechanism of photocatalytic water splitting	6
1.2.3 Requirements of an efficient photocatalyst	7
1.2.4 Investigation of materials for photocatalytic water splitting	8
1.3 TiO ₂ and its Properties	9
1.3.1 Crystalline phases of TiO ₂	9
1.3.2 Stability and phase transformation	11
1.3.3 Physiochemical properties	12
1.3.4 Drawbacks of TiO ₂ for photocatalytic water splitting	13
1.4 Photocatalyst Modification Techniques to Enhance H ₂ production	14
1.4.1 Suppressing backward reaction	14
1.4.2 Tuning the band gap for visible light absorption	16
1.4.3 Suppressing charge carrier recombination	19
1.5 Mixed Phase TiO ₂	21
1.5.1 Synthesis and application of mixed phase TiO ₂	21
1.5.2 Challenges in using mixed phase TiO ₂ as a photocatalyst for water splitting	23
1.6 Motivation and Research Objectives	24
CHAPTER 2 Experimental Techniques	27
2.1 Introduction	29
2.2 Rapid Breakdown Anodization (RBA)	29
2.3 X-Ray Diffraction (XRD)	30
2.4 Raman Spectroscopy	34
2.5 Field Emission Scanning Electron Microscopy (FESEM)	36
2.6 Transmission Electron Microscopy (TEM)	37
2.7 Ultraviolet-Visible Absorption Spectroscopy	40
2.8 Photoluminescence (PL) Spectroscopy	41
2.9 X-ray Photoelectron Spectroscopy (XPS)	45
2.10 Ultra-violet Photoelectron Spectroscopy (UPS)	47
2.11 Electron Paramagnetic Resonance Spectroscopy (EPR)	49
2.12 Mott-Schottky Analysis	52
2.13 Photocatalytic Hydrogen Generation by Water Splitting	55
2.14 Summary	57

CHAPTER 3	Synthesis and Characterization of Band Engineered TiO₂ Heterojunctions	59
3.1	Introduction	61
3.2	Synthesis of Triphase TiO ₂ Nanotubes	64
3.2.1	Effect of synthesis voltage	64
3.2.1.1	Phase evolution	66
3.2.1.1.1	XRD analysis	66
3.2.1.1.2	Raman spectra analysis	69
3.2.1.2	Structural analysis	70
3.2.1.3	Band gap analysis	72
3.2.2	Effect of electrolyte concentration	73
3.2.2.1	Phase evolution	74
3.2.2.1.1	XRD analysis	74
3.2.2.1.2	Raman spectra analysis	75
3.2.2.2	Structural analysis	77
3.2.2.3	Band gap analysis	78
3.3	Synthesis of Nitrogen Doped Triphase TiO ₂ for Visible Light Activity	79
3.3.1	Effect of N doping in triphase composition	80
3.3.1.1	XRD analysis	80
3.3.1.2	Raman spectra analysis	82
3.3.2	Structural analysis	84
3.3.3	Band gap analysis	86
3.4	Synthesis of Hydrogenated TiO ₂ for Visible Light Activity	87
3.4.1	Effect of hydrogenation in phase composition	87
3.4.1.1	XRD analysis	87
3.4.1.2	Raman spectra analysis	89
3.4.2	Structural analysis	90
3.4.3	Band gap analysis	92
3.5	Summary	94
	Photocatalytic Hydrogen Generation Efficiency	
CHAPTER 4	of Triphase Heterojunctions and Their Band Alignment	97
4.1	Introduction	99
4.2	Photocatalytic Water Splitting	100
4.2.1	TiO ₂ nanotubes synthesized at different voltages	100
4.2.2	TiO ₂ nanotubes synthesized at different electrolyte concentrations	101
4.3	Charge Separation Efficiency	103
4.3.1	TiO ₂ nanotubes synthesized at different voltages	103
4.3.1.1	Mott-Schottky analysis	103
4.3.1.2	Photoluminescence	105
4.3.2	TiO ₂ nanotubes synthesized at different electrolyte concentrations	106
4.3.2.1	Mott-Schottky analysis	106
4.3.2.2	Photoluminescence	107

4.4	Energy Band Alignment and Charge Transfer Pathway in Triphase TiO ₂ Nanotubes	109
4.4.1	PL spectra in detail	109
4.4.2	Synchrotron valence band edge analysis	112
4.4.3	Possible band diagrams	113
4.6	Summary	116
Photocatalytic Hydrogen Generation		
CHAPTER 5	Efficiency of Doped Triphase Heterojunctions and Their Band Alignment	117
5.1	Introduction	119
5.2	Photocatalytic Water Splitting	119
5.3	Charge Separation Efficiency	121
5.4	Energy Band Alignment and Charge Transfer Pathway in N - Doped Triphase TiO ₂ Nanotubes	123
5.4.1	XPS and UPS analysis	123
5.4.2	Photoluminescence	128
5.4.3	Effect of N doping in triphase TiO ₂ nanotubes	131
5.4.4	Charge transfer mechanism	132
5.4.5	Synchrotron valence band edge spectra	133
5.5	Summary	134
Photocatalytic Hydrogen Generation		
CHAPTER 6	Efficiency of Defect Induced Triphase Heterojunctions and Their Band Alignment	137
6.1	Introduction	139
6.2	Photocatalytic Water Splitting	139
6.3	Charge Separation Efficiency	141
6.4	Energy Band Alignment and Charge Transfer Pathway in Hydrogenated Triphase TiO ₂ Nanotubes	143
6.4.1	XPS and UPS analysis	143
6.4.2	Photoluminescence	145
6.4.3	EPR analysis	147
6.4.4	Charge transfer mechanism	148
6.5	Summary	150
CHAPTER 7	Summary And Scope Of Future Work	151
7.1	Conclusions	153
7.2	Future Aspects	155
REFERENCES		159

SYNOPSIS

Global demand for energy and its consumption has been rising significantly due to the rapid expansion in economy throughout the nations. Traditional fossil fuel sources such as petroleum, natural gas and coal are still the primary source of power. However, fossil fuel reserve is finite and the continual staggering usage of fossil fuels will gradually result in its depletion. Besides, the combustion of fossil fuels also emits polluting greenhouse gasses strongly believed to be responsible for global warming^{1,2}. Due to these reasons, generation of cheap, clean and renewable energy as an alternative energy source to fossil fuel is becoming more viable and gradually gaining attention from various stakeholders.

Solar energy, on the other hand is clean and environmentally friendly. Its source is virtually inexhaustible and has potential of fulfilling the ever increasing global energy demand. Silicon as well as organic-based photovoltaics has been widely used to tap the potential of solar energy. Another method of harvesting solar energy is through the use of photocatalysts to undergo water splitting reaction, discovered by Fujishima and Honda in the year 1972³. Upon absorbing photons, photocatalysts are able to chemically split water molecules (H_2O) to H_2 and O_2 gases. The significance of photocatalytic water splitting is the generation of H_2 gas via a cheap and clean manner. H_2 can be used to generate energy in hydrogen combustion engines or fuel cells which do not result in any toxic or greenhouse gas emission but produces water instead^{4,5}. However, H_2 does not occur naturally and needs to be artificially produced. Unfortunately, the existing methods to produce hydrogen either generate unwanted greenhouse gases or energy intensive hence costly⁶⁻⁸. Based on these reasons, the alternative approach for H_2 production through the photocatalytic splitting of

water reactions seems to be a more feasible option for the purpose of clean energy generation.

Many semiconducting materials such as oxides⁹⁻¹¹, nitrides^{12,13} and sulphides^{14,15} have been studied for water splitting. Among them, TiO₂, whose band edges suitably aligned with water redox potentials is widely studied for water splitting due to its stable, inexpensive and non-corrosive nature. There are three major crystal phases of titania such as anatase, rutile and brookite. All of these have larger electronic band gaps in the range of 3 - 3.2 eV, which limits their photocatalytic activity in the ultraviolet (UV) region. Given that, the utilization of such radiation accounts to less than 5% of the entire solar energy even if TiO₂ is very efficient in absorbing the whole span of UV light for water splitting. Efficient absorption of natural solar light for a photocatalytic process thus lies in tuning the band gap response of titania to the visible region. Another major concern regarding TiO₂ is it suffers high electron hole recombination, which limits its activity towards water splitting. Therefore, in order to make an efficient TiO₂ photocatalyst, decreasing its band gap, at the same time, inhibiting the recombination of photogenerated electrons and holes will be the sensible solution.

Several attempts were involved to enhance the visible light absorption of TiO₂. Among which a major portion of research is devoted to metals^{16,17} and non metals^{18,19} doping of titania. Although it was successful in tailoring the optical properties to visible region, the dopants often act as recombination centers affecting the photocatalytic efficiency^{20,21}. Recently, dopant free defective TiO₂ has triggered extensive research interest due to the efficient engineering of band gap, towards visible light to infrared absorption^{22,23}.

Hydrogenation of TiO₂ is one of such attempts which produced black/brown titania, whose band offsets shifted to match equivalently with the water redox potential^{24,25}.

Meanwhile titania surface has been modified by various means such as coupling with a narrow band gap semiconductor^{26,27}, metal nanoparticles loading^{28,29} and so on to reduce the recombination of photogenerated charge carriers. Among the modifications adopted, introducing the phase junctions in titania is proved to be the effective strategy to inhibit the fast recombination of excited charge carriers³⁰. This is because the photocatalytic activity of TiO₂ is not only attributed to the energy band characteristics but also sensitive to the phase composition. Recent reports demonstrated that biphasic titania junctions such as anatase-rutile^{30,31}, anatase-brookite^{32,33}, rutile-brookite³⁴ outperform that of the individual phase titania. Very recently it has been reported that the anatase-rutile-brookite (ARB) tri-phase TiO₂ is more efficient than biphasic titania nanoparticles due to the favourable energy band edge alignment of three phases inhibiting the recombination^{33,35}. However synthesizing triphase TiO₂ is difficult as it requires either multiple steps of rigorous reactions and/ extreme thermal treatment. Similarly, unlike anatase-rutile biphasic system, studies on charge transfer characteristics in ARB triphase system has not yet come to the spotlight to determine the underlying physics behind the high efficiency of the triphase system. To understand the actual reactivity of triphase TiO₂ nanostructures in photocatalytic water splitting, research work on the facile synthesis of TiO₂ nanoparticles having three phases in single entity as well as a clear cut picture of the charge transfer mechanism in triphase system is highly appreciable.

Therefore in order to obtain a high quantum efficient visible light water splitting photocatalyst, a novel and simple synthesis technique to prepare triphase TiO₂ nanotube

powders which does not require the use of expensive, time consuming thermal or hydrothermal or rigorous acidic treatments is proposed and executed. The anatase, anatase-rutile and anatase-rutile-brookite TiO₂ nanotube powders were obtained by tuning the potential in electrochemical anodization technique. Similarly, triphase to biphasic transformation was observed with the change in electrolyte concentration during the synthesis. The nanotube powders with various phase compositions are used in photocatalytic water splitting experiments to compare the efficiency of single, bi- and triphasic TiO₂ nanotubes. For the first time, a band diagram is proposed for ARB system with the possible electron transfer pathway. In addition to these studies, modifications of triphasic TiO₂ such as doping of nitrogen and hydrogen annealing were adapted to induce visible light activity. Thus in general, the dissertation focuses on synthesis of triphasic TiO₂ nanotubes, its charge transfer properties as well as band gap engineering in triphasic nanotubes, to develop a high quantum efficient solar water splitting photocatalyst. In this process of band engineering in heterostructured TiO₂, the phase transformations are observed which are also studied in detail. The studies included in the thesis are organized into seven chapters and the contents of each chapter are summarized as follows:

Chapter 1: Introduction

The Chapter 1 discusses the present scenario in generation of hydrogen as a fuel, the scope of hydrogen generation by photocatalytic water splitting technique, the significance of titania as an effective water splitting photocatalyst and its properties. The brief outline on various advantages and shortcomings of titania as a photocatalyst is also presented. The necessity for band gap engineering of titania is briefly presented. The modifications adapted

on titania till date to transform it an efficient photocatalyst and their counter effect on photocatalytic reactions are also discussed. The possibilities of enhanced photocatalytic activity by triphase titania and its modified form are briefly described. The objective and overview of the present thesis are briefed at the end of the Chapter 1.

Chapter 2: Experimental Techniques

The Chapter 2 deals with the experimental techniques and procedures employed for the synthesis, characterization and evaluation of the band gap engineered titania nanotubes in detail. The major characterization techniques for morphological, structural, elemental, energy band gap, band edge, vibrational and luminescence studies are briefly discussed. In addition, the basic features of the hydrogen generation reactor are also presented.

Chapter 3: Synthesis and Characterization of Band Engineered TiO₂ heterojunctions

The Chapter 3 discusses the facile synthesis of anatase-rutile-brookite triphase TiO₂ nanotube photocatalyst using Rapid Breakdown Anodization (RBA) technique for high quantum efficiency in solar assisted water splitting reactions. The effect of DC voltage and electrolyte concentration towards the synthesis of triphase TiO₂ nanotubes are discussed in detail. It is observed that the change in synthesis voltage and electrolyte concentration alters phase composition of TiO₂ nanotubes. As the synthesis voltage is increased, the obtained TiO₂ nanotubes undergo phase transition from anatase (A) to anatase-rutile (AR) to anatase-rutile-brookite (ARB). Similarly, with respect to electrolyte concentration, the TiO₂ nanotubes transforms from anatase-rutile-brookite (ARB) to anatase-brookite (AB) phase

composition. It is observed from HRTEM that all the phases present in single TiO₂ nanotube, giving rise to many heterojunctions.

This chapter also covers the synthesis of visible light active triphase heterojunctions with high quantum efficiency. In order to tune the band gap, triphase TiO₂ nanotubes are modified in two ways such as nitrogen doping and hydrogenation. It is observed that as the nitrogen doping concentration increases, the triphase TiO₂ undergo transformation to biphasic composition, with a gradual decrement in band gap. In case of hydrogenation of triphase TiO₂ nanotubes, the crystallinity increases with annealing temperature with a reduction in band gap as well as change in phase composition.

This chapter hence briefly discuss about the facile synthesis of triphase TiO₂ nanotubes; and effects of experimental conditions, nitrogen doping and hydrogenation on crystallinity, phase composition, morphology and optical band gap of triphase TiO₂ nanotubes.

Chapter 4: Photocatalytic Hydrogen Generation Efficiency of Triphase Heterojunctions and Their Band Alignment

The water splitting efficiencies of TiO₂ nanotubes obtained with variation in synthesis voltage and electrolyte concentration under one sun conditions are discussed in detail. It is found that the triphase TiO₂ is more efficient than biphasic (AR, AB) and single phase (A) nanotubes in generating hydrogen by photocatalytic water splitting. The transfer pathway of photoexcited charge carriers in triphase TiO₂ nanotubes are determined using PL spectra and the synchrotron radiation assisted valence band edge analysis. From the analyses, it is demonstrated that the most probable charge transfer pathway of the excited

electron is from rutile to anatase to brookite. The hydrogen generated by ARB nanotubes is nearly twice that of anatase TiO₂ nanotubes and 1.6 times that of anatase-rutile nanotubes under 4 hours of one sun illumination. Similarly, the hydrogen generated by ARB nanotubes is 1.25 times that of AB nanotubes under the same conditions.

Chapter 5: Photocatalytic Hydrogen Generation Efficiency of Doped Triphase Heterojunctions and Their Band Alignment

This chapter demonstrates the ability of nitrogen doped triphase TiO₂ nanotubes (N-TiO₂) as a visible light active photocatalyst for water splitting with high quantum efficiency. The detailed analyses of all the N-TiO₂ nanotubes demonstrate that, excess nitrogen doping induces brookite to anatase phase transformation with increase in N 2*p* density of states. The changes in density of defect states (Ti³⁺ / oxygen vacancies/N 2*p*) into the band gap of TiO₂ with changes in nitrogen doping are found to be critical in determining the photocatalytic activity of Nt-TiO₂. Among the nitrogen doped triphase TiO₂ samples, the sample with optimum N doping is found to be 7.5 times efficient in photocatalytic hydrogen generation compared to pristine triphasic TiO₂. The hydrogen generation results also indicate that nitrogen doped triphase TiO₂ nanotubes perform better than biphasic nanotubes.

The effects of nitrogen doping in triphase TiO₂ nanotubes at various concentrations are discussed using band diagram. The band alignment and charge transfer pathway of N-TiO₂ is discussed based on synchrotron valence band edge analysis. The presence of nitrogen doping induced defect states below the conduction band edges of each phase and N 2*p* states above the valence band edge of each phase facilitates the easy transfer of excited electrons to the neighbor phase conduction band without recombining, thus readily available for water splitting reactions. In general the present findings imply that optimal nitrogen

doped multiphase TiO₂ nanotubes can result in high quantum efficient visible light photocatalyst.

Chapter 6: Photocatalytic Hydrogen Generation Efficiency of Defect Induced Triphase Heterojunctions and Their Band Alignment

The chapter demonstrates the ability of defect induced triphase TiO₂ nanotubes (H-TiO₂) through hydrogenation as a visible light active photocatalyst for water splitting with high quantum efficiency. It has been observed that the concentration of Ti³⁺ and oxygen vacancies; and their distribution increases significantly with respect to hydrogen annealing temperature. Such changes in defects are found to be critical in enhancing the photocatalytic activity of H-TiO₂. The triphase TiO₂ nanotubes annealed under hydrogen atm. at 450 °C is found to be 16 times efficient compared to pristine TiO₂ in photocatalytic water splitting. Such an increase in photocatalytic activity is explained from the triphase band diagram with defect states below the conduction band of each phase which facilitate the easy transfer of charge carriers from one phase to another. This study showed that the well designed multiphase construction with oxygen vacancies could enhance the photocatalytic activity tremendously. These investigations might provide new insights into the photocatalytic ability of hydrogenated triphase TiO₂ and pave the way for further studies on defective triphase metal oxides for high quantum efficient visible light photocatalytic applications.

Chapter 7: Brief Summary of Thesis and Scope of Future Work

In Chapter 7, the major findings of the thesis are summarized and the directions for future work on pristine and band gap engineered triphase TiO₂ nanostructures are proposed.

References

1. Steinberg, M., *International Journal of Hydrogen Energy* (1999) **24** (8), 771
2. Ward, J. D., and Nel, W. P., *Energy Policy* (2011) **39** (11), 7464
3. Fujishima, A., and Honda, K., *Nature* (1972) **238** (5358), 37
4. Haas, F., *et al.*, *International Journal of Hydrogen Energy* (2005) **30** (5), 555
5. Hotza, D., and Diniz da Costa, J. C., *International Journal of Hydrogen Energy* (2008) **33** (19), 4915
6. Solomon, B. D., and Banerjee, A., *Energy Policy* (2006) **34** (7), 781
7. Guan, J., *et al.*, *Renewable Energy* (2007) **32** (15), 2502
8. Caetano de Souza, A. C., *et al.*, *Journal of Fuel Cell Science and Technology* (2006) **3** (3), 346
9. Nian, J.-N., *et al.*, *International Journal of Hydrogen Energy* (2008) **33** (12), 2897
10. Antony, R. P., *et al.*, *International Journal of Hydrogen Energy* (2012) **37** (10), 8268
11. Teng, F., *et al.*, *ChemCatChem* (2014) **6** (3), 842
12. Zhang, B., *et al.*, *Chemistry of Materials* (2016) **28** (19), 6934
13. Nurlaela, E., *et al.*, *Materials for Renewable and Sustainable Energy* (2016) **5** (4), 18
14. Luo, P., *et al.*, *ACS Applied Materials & Interfaces* (2017) **9** (3), 2500
15. Bedoya-Lora, F., *et al.*, *Electrochemistry Communications* (2016) **68**, 19
16. Melvin, A. A., *et al.*, *Nanoscale* (2015) **7** (32), 13477
17. Patra, K. K., and Gopinath, C. S., *ChemCatChem* (2016) **8** (20), 3294
18. Naik, B., *et al.*, *The Journal of Physical Chemistry C* (2010) **114** (45), 19473
19. Sivaranjani, K., *et al.*, *ChemCatChem* (2014) **6** (2), 522
20. Torres, G. R., *et al.*, *The Journal of Physical Chemistry B* (2004) **108** (19), 5995
21. Hoffmann, M. R., *et al.*, *Chemical Reviews* (1995) **95** (1), 69
22. Bessergenev, V. G., *et al.*, *Applied Catalysis A: General* (2015) **500**, 40
23. Jiang, X., *et al.*, *The Journal of Physical Chemistry C* (2012) **116** (42), 22619
24. Leshuk, T., *et al.*, *ACS Applied Materials & Interfaces* (2013) **5** (6), 1892
25. Liu, N., *et al.*, *Nano Lett* (2014) **14** (6), 3309
26. Li, C.-J., *et al.*, *Journal of Nanoscience and Nanotechnology* (2012) **12** (3), 2496
27. Li, C.-J., *et al.*, *Materials Research Bulletin* (2012) **47** (2), 333
28. Serpone, N., *The Journal of Physical Chemistry B* (2006) **110** (48), 24287
29. Zhang, K., *et al.*, *Small* (2013) **9** (14), 2452
30. Li, G., and Gray, K. A., *Chemical Physics* (2007) **339** (1–3), 173
31. Preethi, L. K., *et al.*, *International Journal of Hydrogen Energy* (2016) **41** (14), 5865
32. Zhao, H., *et al.*, *Journal of Materials Chemistry A* (2013) **1** (28), 8209
33. Mutuma, B. K., *et al.*, *Journal of Colloid and Interface Science* (2015) **442**, 1
34. Xu, H., and Zhang, L., *The Journal of Physical Chemistry C* (2009) **113** (5), 1785
35. Kaplan, R., *et al.*, *Applied Catalysis B: Environmental* (2016) **181**, 465

Introduction

***“Alternative energy is a future idea, whose time is past
Renewable energy is a future idea, whose time has come”***

- Bill Penden

The depleting fossil fuel reserves and its serious environmental impact have emphasized the issue of sustainable development of the human society. Hydrogen fuel by solar water splitting is a promising alternative to conventional fossil fuels, which is of great potential to relieve the energy and environmental issues and bring an energy revolution in a clean and sustainable manner. In view of this, the present chapter discusses the current scenario in fuel reserves and demonstrates the basic principles of artificial photosynthesis. Recent impressive progresses and advancements in photocatalytic water splitting using some promising materials are presented. The importance of TiO₂ and its suitability for water splitting reaction is demonstrated with emphasis on its physicochemical properties and their concerned drawbacks. In addition, various engineering strategies for enhancing the efficiency of hydrogen generation, including light harvesting, and charge carriers separation of TiO₂ have been outlined and discussed. Finally, the chapter is concluded with the objective of the presented thesis.

1.1 Present Scenario in Energy Production

Global energy demands and its consumption have been rising significantly due to the rapid expansion in economy throughout the nations. It is also expected that these issues will be accompanied by a steady increase in cost of energy and renewed concerns regarding energy security and climate change¹. Traditional fossil fuel sources such as petroleum, natural gas and coal are still the primary source of power. However, fossil fuel reserve is finite and the continual staggering usage of fossil fuels will gradually result in its depletion. Besides, the combustion of fossil fuels emits polluting greenhouse gasses strongly believed to be responsible for global warming^{1,2}. Even, the growth of hydrocarbon feed stocks demands vis-à-vis of available fossil fuel resources. This led the world community to search for new alternate fuels. Otherwise, it will make the life on earth unsustainable in the medium and long range². Due to these reasons, generation of cost effective, clean and renewable energy as an alternative to fossil fuel is gradually gaining attention from various stakeholders. Recent studies suggest that the direct use of hydrogen as a fuel provides a clean and affordable energy supply³. Hydrogen, a colorless and odorless gas, is the simplest and most abundant (occupying about 75% of the universe mass) element in the universe. Although hydrogen does not occur naturally, it can always be found with other elements such as water and organic compounds⁴.

In recent years, hydrogen is being produced in large quantities for commercial and industrial purposes. Major portion of hydrogen produced for industrial utilization is through natural gas reforming, coal gasification and electrolysis. About 96% of worlds' hydrogen is currently produced from natural gas, oil or coal (48% from natural gas, 30% from oil, 18% from coal, and the remaining 4% via water electrolysis)⁵. These methods of hydrogen

production demands huge infrastructure and significant energy resources. Unfortunately, the existing methods to produce hydrogen either generate unwanted greenhouse gases or are energy intensive⁶⁻⁸. Because of these drawbacks, the alternative approach for H₂ production through photocatalytic splitting of water seems to be a more feasible option. The significance of photocatalytic water splitting lies in the generation of H₂ under solar irradiation in a cost effective and clean manner. Hydrogen can be used to generate energy in combustion engines or fuel cells that do not result in any toxic or greenhouse gas emission but produces water instead^{4,5}.

1.2 Photocatalysis

Photocatalysis is the acceleration of a photoreaction in the presence of a catalyst leading to generation of highly reactive radical species, by using solar energy⁹. This process has the ability to oxidize the organic material and even mineralize the intermediates into non-hazardous compounds. Photocatalytic reactions are initiated when a semiconductor catalyst is illuminated by light (photon) with energy equal to or greater than the semiconductor band gap energy ($h\nu \geq \Delta E_g$). Among various applications of photocatalysis, water splitting to generate hydrogen is found to be of great interest among researchers for its potential to replace conventional fuel sources for green energy.

1.2.1 Artificial photosynthesis

Water splitting into hydrogen and oxygen using photon energy is accompanied by a large positive change in Gibbs free energy (+237 kJ/mol) and hence it is an uphill reaction. Similar reactions occur in green plants, which are termed as photosynthesis^{10,11}. Therefore

water splitting with the aid of solar energy is termed as artificial photosynthesis. As pure water does not absorb solar radiation, its splitting needs a photo-semiconductor capable of efficiently absorbing solar energy and then splitting the molecule in an indirect way. The photo-semiconductors are termed as photocatalysts and the water splitting using them is termed as photocatalytic water splitting.

There are two subtypes of photocatalysis which are termed as homogeneous and heterogeneous catalysis. In homogeneous photocatalysis, both the catalyst and the reactants in the chemical system are in the same phase, whereas in heterogeneous catalysis, they are of different phases. Even though the use of homogeneous catalysts is advantageous in elucidating the detailed catalytic mechanisms such as detecting active intermediates for water oxidation; heterogeneous catalyst makes a strong impact because of its practical applications due to its high photocatalytic activity. This brought numerous reports on the study of photochemistry of heterogeneous catalysis which blends principles of physics, chemistry and engineering¹²⁻¹⁵.

The photoassisted water splitting using heterogeneous photocatalysts can be performed under two different configurations. They are (i) photoelectrochemical systems in which two electrodes, with one having the photocatalyst on its surface, in aqueous electrolyte performing oxidation/reduction reactions respectively and (2) particulate photocatalytic systems where the powder photocatalysts are suspended in aqueous solution and redox reactions takes place at its surface. Comparing the two configurations, particulate photocatalysis is advantageous as it is simple, cost effective and do not require expensive transparent electrodes and electrical energy. However it faces difficulty in separation of

generated hydrogen and oxygen due to the possibility of reverse reaction¹¹, which are suppressed by introducing alcohols, aldehydes etc.^{16,17}.

The first demonstration of photoelectrolysis of water using titania and platinum electrodes was performed by Fujishima and Honda¹⁸. During photo-irradiation with photons of energy greater than the band gap of TiO₂, under direct current, oxygen and hydrogen are evolved at TiO₂ and Pt electrodes respectively¹⁸. This discovery inspired researchers across globe leading to extensive research on hydrogen generation by water splitting using a wide variety of semiconductor photocatalyst that continues till date.

1.2.2 Reaction mechanism of photocatalytic water splitting

“A photocatalyst is a material (usually semiconductor) that absorbs photons, generating electron/hole pairs that assist in accelerating the desired reaction”. The schematic representation of water splitting reaction by a semiconductor is shown in Figure 1.1.

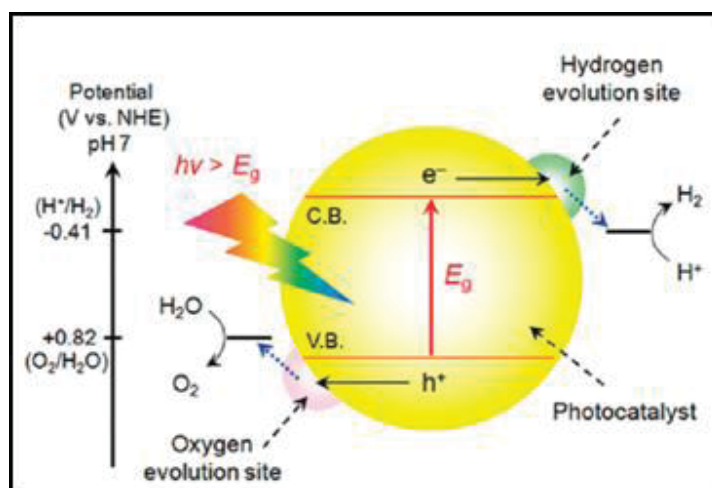
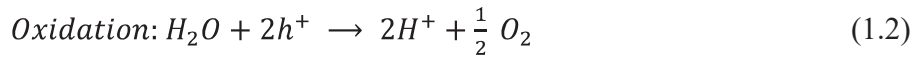


Figure 1.1 Schematic representation of photocatalytic water splitting

To generate hydrogen through splitting water, the CB and VB edges of any semiconductor photocatalyst should be well matched with the redox potential of water as shown in Figure 1.1. During light illumination, the photocatalyst generate electron-hole pairs which undergoes reduction and oxidation reactions in water by the following sequence:



For a better water splitting efficiency, the CB edge should be higher than hydrogen reduction level (E_{H_2/H_2O}) while the VB edge should be lower than water oxidation level (E_{O_2/H_2O}). Therefore, the minimum photon energy thermodynamically required to drive a water splitting reaction is 1.23 eV^{19,20}. From the viewpoint of thermodynamics, in addition to the above mentioned energy, an additional electric potential of the electrons (at least 0.6 eV) is required to electrolyze water smoothly under one sun condition. Therefore, the minimum band gap required for water splitting is around 2 eV. The theoretical water splitting efficiency increases when the band gap of semiconductors is close to 2 eV²¹. But, most of the semiconductors have band gap larger than 2 eV, so the activity under visible light is limited. Therefore it is necessary to engineer the band gap to suit this requirement.

1.2.3 Requirements of an efficient photocatalyst

A semiconductor material becomes an efficient water splitting photocatalyst only when it satisfies several functional requirements with respect to semiconducting and electrochemical properties including²² (1) appropriate visible light absorption with band gap around 2.0 - 2.2 eV and band edge potentials suitable for overall water splitting; (2) ability to separate photo-excited electrons from reactive holes once formed; (3) minimization of energy losses related to charge transport and electron-hole recombination; (4) chemical stability to chemical and photocorrosion; (5) kinetically suitable electron transfer properties from photocatalysts' surface to water; and (6) low production cost. However most semiconductors with suitable band edge positioning with respect to water redox potential, are found to be UV light active which spans only 5% of the entire solar spectrum. So far, the maximum apparent solar to hydrogen conversion efficiency records only 16%²³. The low solar to hydrogen conversion efficiency is still the "bottleneck" for solar water splitting. Consequently, the design of efficient semiconductor photocatalytic systems for production of molecular hydrogen from water is one of the foremost challenges in the development of solar hydrogen economy²².

1.2.4 Investigation of materials for photocatalytic water splitting

A large number of semiconductor materials have been studied for photochemical and photoelectrochemical process in the last four decades. Many types of semiconductors such as oxides, nitride, sulphides, carbides and phosphides etc. have been investigated till date. Many of these materials are reported to possess better water splitting capability along with one or the other disadvantages. A few important materials that are prevalently studied for water splitting reactions are metal oxides such as TiO_2 ^{17,24}, ZnO ²⁵, SnO_2 ^{26,27}, WO_3 ^{28,29}, Fe_2O_3 ^{30,31}, and RuO_2 ^{32,33}, compounds such as GaAs ³⁴, CdTe ^{35,36} and CdSe ^{37,38}, sulphides such

as CdS³⁹, ZnS^{40,41}, GaS⁴² and metal (oxy) sulphide^{43,44}, metal (oxy) nitride⁴⁵, tantalates^{46,47}, niobates⁴⁸, tungsten based materials^{49,50}, metal oxides with d⁰ and d¹⁰ electronic configuration³², perovskite type materials⁵¹, inorganic complexes^{52,53} etc.

Among these materials, titania become a prominent one because of its favorable band gap, high chemical and photoelectrochemical stability, biological inertness, low cost, ease in preparation methods, etc⁵⁴. A lot of studies with its modified forms are still been carried out.

1.3 TiO₂ and its Properties

Titanium dioxide (TiO₂), also known as titania, a white inorganic solid substance, belongs to the family of transition metal oxide. Titanium which is the ninth most common element in the earth's crust, is thermally stable, chemically inert, bio-compatible, non flammable and nonhazardous. Titania has been investigated for over 45 years due to its photoelectric and photochemical properties. After the demonstration of water splitting into H₂ and O₂ by defective titania¹⁸, the understanding of the reaction mechanism opened up a large number of applications of titania including volatile organic compound decomposition, disinfection in hospitals, purification of air/water, dye sensitized solar cells, organic synthesis, cancer therapy etc.

1.3.1 Crystalline phases of TiO₂

TiO₂ has several types of crystalline forms some of them are anatase, rutile, brookite, TiO₂-B, TiO₂-R, TiO₂-H, TiO₂-II and TiO₂-III⁵⁵. Among these, rutile, anatase and brookite are naturally occurring phases at atmospheric pressure and have been studied extensively for

various applications⁵⁶⁻⁵⁹. The other five phases occur at high pressure hence they are of minor significance for research and development applications⁶⁰⁻⁶³. Hence from now we focus only on anatase, rutile and brookite phases of titania.

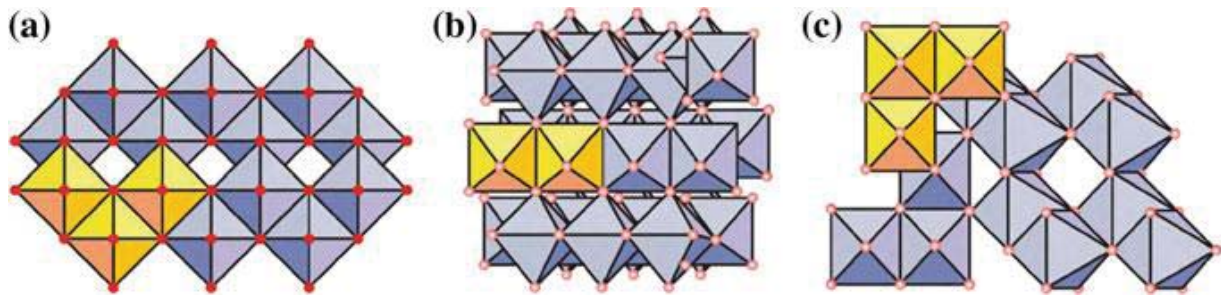


Figure 1.2 Crystalline structures of (a) anatase, (b) brookite and (c) rutile

Table 1.1 Physical and structural properties of anatase, brookite and rutile phases

Property	Anatase	Brookite	Rutile
Molecular weight (g/mol)	79.9	79.9	79.9
Crystal structure	Tetragonal	Orthorhombic	Tetragonal
Point group	4/mnm	Mnm	4/mnm
SpaceGroup	I41/amd	Pbca	P4 ₂ /mnm
Unit Cell	a = b = 3.784, c = 9.515 Volume = 136.25	a = 5.455, b = 9.181, c = 5.142 Volume = 257.38	a = b = 4.593, c = 2.959 Volume = 62.07
Density (g/cm ³)	3.894	4.123	4.25
Band gap (eV)	3.23	3.14	3.02

In TiO₂, each titanium ion (Ti⁴⁺) is bonded to six oxygen ions (O²⁻) forming a TiO₆ octahedron configuration. The differences in physical, structural and optical properties of the three phases of titania are attributed to the difference in the arrangement of these octahedral units and the assembly pattern of the octahedral chains⁶⁴. Anatase has a tetragonal structure

in which the octahedral units share their edges. Brookite belongs to orthorhombic crystal system in which both the vertices (corners) and the edges are shared by the octahedral units, whereas, in rutile, the octahedra share the vertices to give a tetragonal structure. The representative unit cells are illustrated in Figure 1.2 and the physical/structural properties are listed in Table 1.1.

1.3.2 Stability and phase transformation

Thermodynamically, rutile is the stable form of TiO₂, whereas anatase and brookite are metastable and are readily transformed to rutile phase under heat treatment (>400 °C). The presence of unintentional impurities or intentional dopants has a strong effect on the kinetics of the phase transition⁶⁵. Various results have been reported stating that dopants can have the effect of hindering or enhancing the phase transition. In the case of substitutional solid solution formation, dopant ions can enter the lattice and influence the level of oxygen vacancies, thereby promoting or inhibiting the transformation. In the case of interstitial solid solution formation, lattice constraint may result in destabilisation or stabilisation, depending on size, valence, and content effects, again promoting or inhibiting the transformation. If the solubility limit of impurities or dopants is exceeded, then their precipitation can facilitate the phase transformation through heterogeneous nucleation^{66,67}. Similarly, reductive atmosphere such as H₂ and Cl₂ accelerate the transformation and gases that are conducive to Ti interstitial formation decelerate the phase transformation⁶⁸. The synthesis of TiO₂ nanoparticles in general results in anatase phase especially when the preparation takes place in aqueous media⁶⁹. This is due to the close proximity of the surface energy of the three phases. Anatase is more stable at crystallite

sizes below 11 nm, brookite at crystal sizes between 11 and 35 nm, and rutile with the crystal sizes ≥ 35 nm⁷⁰.

1.3.3 Physiochemical properties

TiO₂ is an n-type wide band gap semiconductor, whose valance band is composed of 2*p* orbitals of oxygen hybridized with the 3*d* orbitals of titanium, while the CB is composed mainly of 3*d* orbitals of titanium⁶⁴. Among the three phases, anatase and rutile are the most studied crystalline forms with respect to photocatalysis because they can be easily prepared in pure form from titanium precursors⁵⁹. Brookite is often observed as a by-product in sol-gel synthesis at low temperature. Pure brookite without rutile or anatase is rather difficult to be prepared so that, until recently, its photocatalytic behavior has not been studied in detail⁵⁹.

After the discovery of Fujishima and Honda, the concept of hydrogen generation by photocatalytic water splitting has been a rife in the research community. This stimulated several reports on water splitting by using different phases of TiO₂ and their photochemistry are being reported till date⁷¹⁻⁷⁴. This includes the study of variety of TiO₂ structures ranging from small particles such as powders, clusters and colloids to large single crystals that supports oxidative and reductive reactions of many type of organic and inorganic adsorbates. This is followed by the studies on the effect of various morphologies, pore sizes, phases and synthesis methods on their photocatalytic activities. Specifically, research on the various architectures of TiO₂ such as nanorods/nanotubes^{16,56,75-80}, nanospheres⁸¹⁻⁸³, nanowires^{84,85}, nanocrystalline particulates⁸⁶⁻⁸⁸ and thin films⁸⁹⁻⁹¹ has been extensively carried out. Some of the most common synthesis methods followed to synthesize various nanostructures are chemical vapor deposition (CVD)^{92,93}, hydrothermal^{87,94}, pulsed laser deposition^{95,96}, sol-

gel^{97,98}, atomic layer deposition (ALD)^{99,100}, anodization^{101,102} etc. Due to the significance of porosity in TiO₂ nanostructures, macro-porous¹⁰³, meso-porous^{104,105}, and micro-porous^{106,107} TiO₂ nanomaterials are synthesized as they play a significant part in determining the effective surface area of the catalyst during reactions.

All these physicochemical properties, decide the scale of photocatalytic activity of TiO₂. Titania with large surface area possess high photocatalytic reaction rates because of the presence of large concentration of active sites¹⁰⁸. However, a high surface area is prone to surface charge pair (electron-hole) recombination due to the presence of large amount of crystalline defects, leading to poor performance in photoactivity. Amorphous TiO₂ has poor photocatalytic performance in contrast to TiO₂ with high crystallinity mainly because of the high density of surface defects. This indicates that a balance between surface area and crystallinity is necessary to produce an effective photocatalyst¹⁰⁹. Similarly particle size is also an important parameter that affects photocatalytic activity as it decides the type of recombination (surface or volume recombination) and spectral shift (UV and visible light absorption)¹¹⁰. The same way, the choice of crystal structure (anatase, rutile and brookite) and phase composition of TiO₂, also play a crucial role in predicting its photocatalytic activity. In addition, surface adsorption-desorption characteristics is also essential in defining the activity as photocatalysis is a surface phenomenon. In conclusion, an optimized combination of the physicochemical properties of TiO₂ is necessary to produce an efficient photocatalyst for enhanced photocatalytic water splitting.

1.3.4 Drawbacks of TiO₂ for photocatalytic water splitting

Having strong catalytic activity and high chemical inertness, TiO₂ with optimized physicochemical properties alone doesn't make it an ideal candidate for enhanced water splitting. The major limiting factors are,

(i) Fast backward reaction: Decomposition of water into hydrogen and oxygen by TiO₂ photocatalyst is an energy intensive process. This easily enables the backward reaction of hydrogen and oxygen recombination to produce water.

(ii) Inactive to Visible light: Large band gap (anatase: 3.23 eV, rutile: 3.02 eV and brookite: 3.14 eV) of TiO₂ makes it only UV light active (corresponds to shorter wavelength < ca. 390 nm) which accounts only for about 5% of solar spectrum. The rest of the solar spectrum is mainly composed of visible (about 50%) and IR radiation. Thus inability to utilize visible light limits the efficiency of TiO₂ photocatalyst.

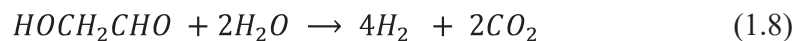
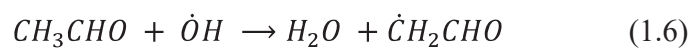
(iii) Recombination of excited charge (electron-hole) pairs: After photoexcitation, CB electrons can easily recombine with VB holes in very less time and the energy is released in the form of unproductive heat or photons;

In order to overcome the above problems and to improve the photocatalytic efficiency of water splitting, numerous modifications were carried out. The commonly applied techniques are cation/anion doping, cocatalyst loading, dye sensitization, coupling with other semiconductors, addition of electron donors (hole scavengers) etc. which are discussed briefly in the following sections.

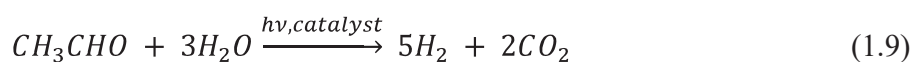
1.4 Photocatalyst Modification Techniques to Enhance H₂ Production

1.4.1 Suppressing backward reaction

The various intermediate reactions such as the photoexcited charge carriers interacting with the lattice and surface defects as well as with an impurity substituting the lattice sites of a semiconductor photocatalyst might occur during water decomposition. These unavoidable pathways make the water splitting a complex reaction, which in turn decreases the efficiency of hydrogen generation. The use of sacrificial agents to act as electron donors or hole acceptors increases the efficiency of hydrogen generation either by suppressing the recombination of electrons and holes through various reactions irreversibly and by minimizing the reverse reaction between oxygen and hydrogen^{111,112}. Some of the prevalently used electron donors are alcohols (methanol, ethanol, isopropanol, etc.), acids (formic acid, acetic acid, etc.), aldehydes (acetaldehyde, formaldehyde, etc.). Among them methanol and ethanol are widely used. It is reported that the amount of hydrogen produced by decomposition of ethanol is less compared to that generated by methanol, formaldehyde, formic acid etc^{113,114}. Hence in our work, we have utilized ethanol as sacrificial agent. The reaction mechanism of ethanol is as follows¹¹⁵:



The overall reaction is



Thus the presence of ethanol scavenges the holes and in turn produces hydrogen and carbon-di-oxide.

1.4.2 Tuning the band gap for visible light absorption

Although there has been extensive research on photocatalytic activity of titania, an efficient visible light active photocatalyst with high quantum efficiency is still a distant goal. The wide band gap of titania (≈ 3.2 eV) is capable of absorbing only UV light, hence various modifications are adapted to narrow the band gap. Some of them are metal doping, non metal doping, metal/non metal co-doping, and coupling with other semiconductors. There are several successful synthesis methods for modifying TiO_2 , including impregnation, deposition-precipitation, sol-gel process, hydrothermal reduction and photo-deposition.

Metal doping is an efficient strategy to activate TiO_2 in visible-light region mainly because the FL of these metals (especially noble metals) is lower than that of TiO_2 which results in better transfer of electrons from TiO_2 to the metal particles. Extensive research has also been focused on the doping of transition and rare earth metal ions ($\text{Fe}^{116,117}$, $\text{Cr}^{118,119}$, Co^{120} , Mn^{121} , V^{122} , Ce^{123} , La^{124} , Ni^{125} etc) for improving the photocatalytic activity of TiO_2 in the visible light range.

Similarly, another approach of non-metal doping in TiO_2 , is also of high interest due to the fact that anion dopants show a lower formation of recombination centers when compared to metal dopants. A wide variety of non metal ions (N^{16} , S^{126} , F^{79} , C^{127} , B^{128} etc) doped TiO_2 nanostructures have been explored till date to narrow the band gap that allow the absorption into visible region due to the introduction of dopant impurity level into the band gap of titania.

In titania, the $3d$ orbitals of Ti govern the CB and O $2p$ orbital occupy the VB. Cation doping generates impurity levels in the forbidden gap or resonates with the bottom of the CB while anion doping mostly modifies the VB due to the generation of

different p orbitals in relation to the O 2p states¹²⁹. The two effects of doping are (i) reducing the band gap either by increasing the top of VB edge or lowering the bottom of CB edge or (ii) introducing intra band states (Figure 1.3). Thus the visible light photoactive transitions in doped titania are obtained due to the excitation of an electron from mid band gap energy level to CB^{16,130} or the excitation of electron from the VB to the mid band gap energy level as shown in Figure 1.3. The photocatalytic activities of doped TiO₂ are dependent on the method of synthesis and dopant content. Dopant ions often act as charge trapping sites that reduces the recombination rate; however, conflicting reports are also found in literature stating that mono dopant ions (transition metals ions) may also acts as recombination centers for photogenerated carriers¹³¹.

Recently, it has been reported that the optical drawback in mono-doped (cations or anions) TiO₂ can be compensated by codoping. Some of the attractive combinations of doping, includes nonmetal and metal co-doping, e.g. N-W¹³² and N-Ta¹³³, N-Pt¹⁶, S-Bi¹³⁴, C-Mo¹³⁵, B-V¹³⁶ or two nonmetal ions co-doping, e.g. C-H¹³⁷, N-H¹³⁷, C-N¹³⁸, N-S¹³⁹. In such case of codoping, both band gap narrowing and a decrease in recombination centers can be achieved resulting in enhanced photocatalytic activity¹²⁹. The photo-reactivity of doped photocatalyst in general depends on the energy level of dopant within the TiO₂ band gap, light intensity, method of doping and dopant concentration. Also it is difficult to derive unifying conclusions from the reported results regarding the factors which influence the doping phenomena, because of the difference in the experimental conditions, sample preparation, photoreactivity and characterization methods. However, it is common opinion among researchers that there is an optimum limit for dopant ion addition. The limit lies usually at low dopant concentration and if the amount exceeds the limit then dopants

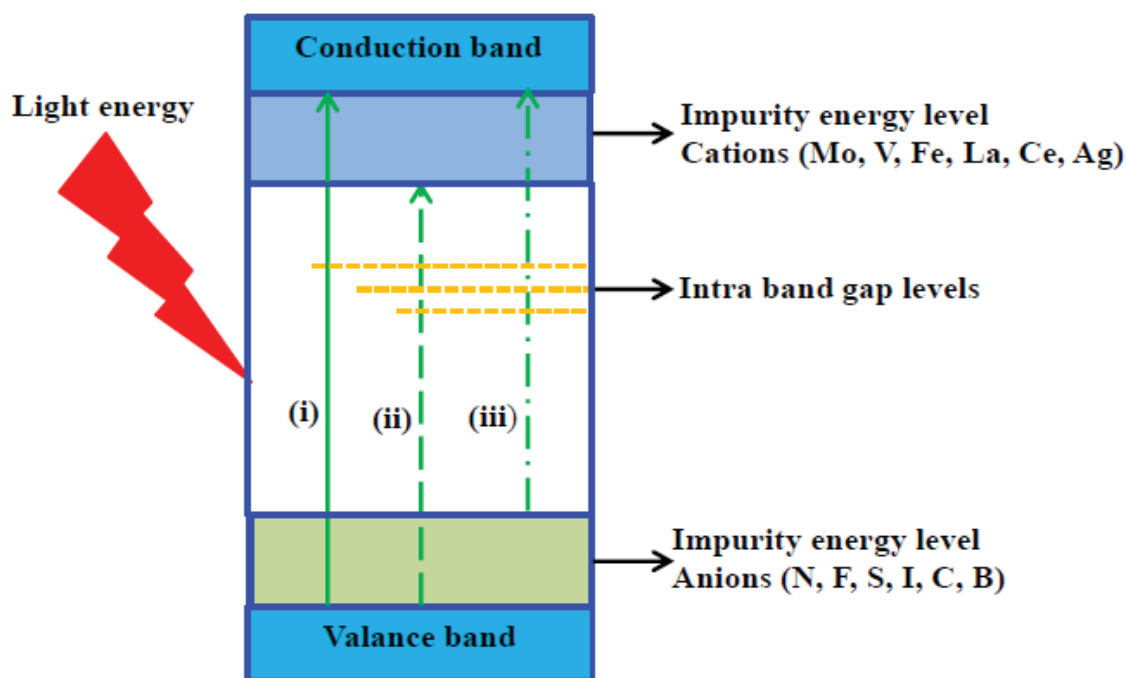


Figure 1.3 Schematic of (i) undoped (ii) cationic and (iii) anionic doped TiO₂

become the recombination sites and as a consequence the photocatalytic phenomenon is adversely influenced¹³¹. In conclusion the photophysical properties of doped and codoped photocatalysts still require investigation because bulk and surface properties and photocatalytic activity strongly depend on the doping method used and also on the nature and concentration of the dopant precursor¹¹⁰.

In view of this, the approach of nitrogen doping in TiO₂ which has the competitive virtues of efficient visible light activity and less deep level trap, has gained wide attention for the past decade. After Asahi et al, many authors have observed that nitrogen doped TiO₂ (N-TiO₂) shows significant catalytic activity in various photocatalytic reactions due to the modification of its electronic structure. This along with the tuning of surface oxidation state can have a great impact on its photocatalytic activity.

The mechanism of the enhancement of light absorption by N-doping is still controversial. Asahi et al¹⁴⁰ claimed that the doped N atoms narrow the band gap of TiO₂ by mixing N 2p and O 2p states, thus explaining the activity for the decomposition of acetone and methylene blue. Irie et al¹⁴¹ argued that the isolated narrow band located above the VB is responsible for the visible light response. Ihara et al¹⁴² suggested that the visible light activity is attributed to the oxygen vacancies caused by N doping.

Although the doping of metal and non metal ions extends the absorption of TiO₂ into the visible-light region and improves photocatalytic activity, the introduction of foreign atoms into the lattice is not always desired. Therefore the generation of native defect states into the band gap of TiO₂ for visible light absorption is highly appreciable. Thermodynamically, the water splitting potential is only 1.23 V. This band gap energy corresponds to a wavelength of 1000 nm. So, ideally, the color of TiO₂ should be tuned to black, with an energy gap of 1.23 eV corresponding to an absorption in near infrared region.

In 2011, hydrogenation has been reported as an effective approach to obtain black TiO₂ with the band gap around 1.5 eV with an optical onset around 1.0 eV¹⁴³. This discovery has triggered world-wide research in black TiO₂ nanomaterials¹⁴⁴⁻¹⁴⁷. Indeed, it is well known that heating TiO₂ under vacuum or in a reducing atmosphere leads to color changes¹⁴⁸. Generation of Ti³⁺ or/and oxygen vacancies turn white TiO₂ into yellow, blue or black¹⁴⁸.

1.4.3 Suppressing charge carrier recombination

Charge carrier recombination is undesirable, leading to loss of photo excited electrons and holes thus limiting the photocatalytic performance of TiO₂. Due to the high

recombination rate, only a small fraction of these charge carriers (5%) can be used to undergo redox reactions at the interface. Modification of TiO₂ by organic dye photosensitization^{149,150}, noble metal deposition^{17,56} or doping¹⁵¹⁻¹⁵³ and semiconductor compounding¹⁵⁴⁻¹⁵⁶ can effectively utilize the incident photons and enhance the charge separation, thereby improving its photocatalytic efficiency. Under illumination, the dyes absorb photons of longer wavelengths beyond the absorption range of TiO₂, where the electrons are excited from the highest occupied molecular orbital (HOMO) level to lowest unoccupied molecular orbital (LUMO) level. The photoexcited electrons will then be transferred to CB of TiO₂ increasing the number of free electrons available for photocatalytic reactions¹⁵⁷. The deposition of metal nanoparticles on TiO₂ nanostructures enhance the quantum yield of photoinduced charge transfer process by (i) improving charge separation within the oxide semiconductor, (ii) discharging photogenerated electrons across the interface and (iii) providing redox pathway with low overpotential¹⁵⁸. Besides acting as photosensitizers for charge injection or as electron traps for facilitating charge separation, noble metal nanoparticles can also act as the light trapping or scattering agent in TiO₂-metal structures. Heterojunction formed by coupling with different semiconductors of appropriate band structures has been considered to be an effective approach to overcome the charge pair recombination by means of inter-particle charge transfer¹⁵⁹. The difference in chemical potential between two semiconductors causes band bending at the junction interface, which induces a built-in field, driving the photogenerated electrons and holes to move in opposite directions, leading to a spatial separation of the charge carriers on the different sides of the heterojunction.

However, the above methods face drawbacks such as poor reaction stability and controllability, high cost, photocorrosion etc. In these respects, mixed-phase TiO₂ with relatively simple preparation process, low cost, resistance to photocorrosion and adjustable crystal type has attracted much attention. Recent studies have demonstrated that, the mixed phase in TiO₂ have higher photocatalytic activity compared to single phase TiO₂¹⁶⁰.

1.5 Mixed Phase TiO₂

Many research reports state that the mixtures of rutile and anatase TiO₂ forming heterojunctions can significantly improve the photocatalytic activity^{16,115,161}. These results invoked extensive research on other phase combinations of TiO₂ such as anatase-brookite^{162,163}, rutile-brookite¹⁶⁴, anatase/TiO₂(B)¹⁶⁵ and anatase-rutile-brookite^{160,166}. The results of these studies also state that the mixed phase TiO₂ performs better in photocatalytic activity compared to single phase TiO₂. The enhanced photocatalytic activity of mixed phase TiO₂ is due to the difference in band edge positioning of the phases. Their combination can effectively promote the separation of photo-generated electron-hole pairs. In addition, interface of different phase junctions can acts as “catalytic hot spots”, therefore increasing the photocatalytic efficiency in many folds¹⁶⁷⁻¹⁶⁹. Owing to the better performance of mixed phase TiO₂ heterostructures compared to single phase, great efforts have been devoted to synthesize TiO₂ with different phase heterojunctions and apply them in photocatalysis.

1.5.1 Synthesis and application of mixed phase TiO₂

The mixed phase TiO₂ nanomaterials having different phase compositions are obtained through several synthesis techniques. The hydrothermal method is used most commonly for the preparation of TiO₂ mixed phases in laboratory scale¹⁷⁰⁻¹⁷². The phase

compositions of mixed phase TiO₂ are controlled by varying the process parameters¹⁷³. Solvothermal method is similar to hydrothermal method wherein organic solvents are used instead of an aqueous environment for the synthesis of mixed phase TiO₂. Similar to hydrothermal method, the crystal phases and morphology of the TiO₂ nanomaterials synthesized by solvothermal method are controlled by regulating parameters such as the autoclave pressure, the reaction temperature, the reaction time and the titanium source^{174,175}. The mixed phase TiO₂ nanomaterials, prepared by the above two methods are usually well crystallized and doesn't require calcinations under high temperature. Besides these advantages, these methods face drawbacks including the requirement of special equipments to withstand high temperature and high pressure. In addition, the reaction is sometimes incomplete due to the absence of stirring process and hence difficult to reproduce the uniform product.

Recently, microemulsion method combined with solvothermal method termed as “microemulsion mediated solvothermal method” has been used to prepare the mixed phase TiO₂ crystals. The advantage of this method lies in the synthesis of small grain size of the product and good control over the phases^{176,177}. Another commonly used method for preparation of mixed phase TiO₂ is sol-gel method. This method has the ability to synthesize various shapes of high pure small size mixed phase TiO₂ at low temperature. However, this method requires long time aging and the particles agglomerate after high temperature calcinations, which may have a significant impact on the photocatalytic activity¹⁶⁸. Another method, solvent mixing and calcinations method (SMC method) which refers to mixing of different phases of TiO₂ in a suitable solvent and then evaporating it followed by calcinations at high temperature to make a close contact among different crystal phases. The

phase composition of the product can be regulated easily using this SMC method however the resultant TiO_2 is prone to easy agglomeration under final high temperature calcinations process. In addition, it is difficult to achieve perfect mixing of different phases, thus limiting its photocatalytic performance^{178,179}.

The mixed phase TiO_2 product obtained by above methods is of mainly anatase-rutile (AR), anatase-brookite (AB) and some gives rise to rutile-brookite (RB) compositions. These different phase mixtures are widely studied for photocatalytic water splitting and are found to be highly active than its component phases in charge separation. There are very few reports on the synthesis of anatase-rutile-brookite (ARB) triphase TiO_2 . Although ARB is a rare polymorph and its synthesis involves multiple steps of rigorous reactions and/ thermal treatment, their importance in photocatalysis is recently realized^{160,180}. The phase selection in these synthesis techniques depends on the reactant concentration, temperature and reaction time¹⁸¹⁻¹⁸³. Unlike the widely studied single or biphasic systems, the reports on water splitting efficiency of ARB triphase TiO_2 nanostructures are unavailable. To understand the actual reactivity of triphase TiO_2 nanostructures in the photocatalytic water splitting, a facile synthesis of TiO_2 nanoparticles having three phases in single entity whose phase compositions are not separated by dispersion is highly appreciable.

1.5.2 Challenges in using mixed phase TiO_2 as a photocatalyst for water splitting

Research on synthesis methods and applications of mixed-phase TiO_2 in photocatalysis have made great progress since years. The superior photocatalytic performance of mixed-phase TiO_2 to single-phase TiO_2 has been well received among the researchers and the mechanism of the enhanced photocatalytic activities has also been

widely studied. However, there are still many problems remaining to be resolved. Some of the important issues are:

(1) Particulate mixed-phase TiO_2 nanomaterials are prone to agglomeration, which will greatly decrease the photocatalytic activity;

(2) Although the relatively narrow band gap of rutile extends the absorption of the mixed-phase TiO_2 slightly to visible light range, it is still insufficient to utilize all visible light radiation from sun light, limiting its application in sun light assisted photocatalysis;

(3) Although researchers all agree that the mixed-phase crystal structure enables the effective separation of photogenerated electrons and holes, thereby enhancing the photocatalytic activity, there is much controversy about the mobility direction of photo-generated electrons and holes¹⁸⁴. Further research is essential to confirm the mechanism of the enhanced photocatalytic activity of mixed-phase TiO_2 .

Therefore, developing mixed-phase TiO_2 nanomaterials in advantageous nanostructures, enhancing the visible light utilization, and exploring the mechanism by newly developed characterization techniques will continue to be the challenges and hot research topics in this area.

1.6 Motivation and Research objectives

Although mixed-phase crystal TiO_2 has been studied for decades, it is still a popular topic due to its excellent photocatalytic activity and there exists a large gap to be covered. In recent days, with increasingly serious energy and environmental problems, the application of mixed-phase TiO_2 in water splitting application is anticipated to attract considerable attention. It is seen that the efficiency of triphase TiO_2 in photocatalysis is recently realized

as it is found to perform better than its biphasic and single phase forms. Also it is demonstrated that the physicochemical properties and application of triphasic TiO₂ in photocatalytic water splitting is not yet ventured due to the difficulties in synthesis of triphasic TiO₂ in single entity. Considering the above issues, a stepwise systematic approach to explore triphasic TiO₂, for hydrogen generation by photocatalytic water splitting is the main objective of this thesis, which is represented in following points:

- Oxides in nanotubular forms are of high importance in photocatalysis due to the availability of high active surface area and enhanced electron transport properties. Therefore having three phases of TiO₂ in single nanotube is advantageous as it forms a single entity which gives rise to bulk heterojunctions and hence high photo-excited charge transfer properties. Therefore, the first objective of this thesis is to synthesize triphasic TiO₂ using electrochemical anodization technique as it is a facile, cost effective technique which gives rise to nanotubular TiO₂ powders and using it in water splitting.
- The co-existence of three phases is highly sensitive to experimental conditions. Hence it is necessary to study the growth mechanism of triphasic TiO₂ with respect to change in applied potential and electrolyte concentration in electrochemical anodization technique. Also, the ability of triphasic TiO₂ in water splitting is understood only when it is compared with its biphasic and single phase forms. Hence it is necessary to be able to tune the conditions so as to obtain TiO₂ nanotubes with varied phase compositions, such as single phase, biphasic and triphasic, single experimental set up.

- Unlike, biphasic TiO₂, the photo-excited charge transfer properties of triphasic TiO₂ has not been explored yet. Therefore it is necessary to study the band alignment and charge transfer properties of the synthesized triphasic TiO₂ nanotubes.
- Among various modifications adopted to decrease the band gap of TiO₂, nitrogen doping is found to be promising. Hence in order to extend solar light harvesting, nitrogen doping is to be carried out without altering the triphasic composition in nanotubes. Also it is necessary to delineate the effect of N doping into triphasic TiO₂ with change in nitrogen concentration. The solar water splitting ability of N-doped triphasic TiO₂ should be compared with its pristine form. In addition, the charge transfer pathway of N-doped triphasic TiO₂ should be delineated in order to understand the photocatalytic mechanism.
- In order to obtain enhanced light absorption in triphasic TiO₂ without the need of external doping, the intraband states should be created by generating native defects. This can be achieved by means of hydrogen annealing the triphasic TiO₂. This as the advantage of having negligible recombination centers as external dopant sites act as recombination centers. The water splitting ability of hydrogenated triphasic TiO₂ should be compared with its pristine form. In addition, the charge transfer pathway of photoexcited charge carriers in hydrogenated triphasic TiO₂ should be delineated in order to understand its water splitting efficiency.
- Finally the photocatalytic efficiencies of pristine and band engineered triphasic TiO₂ are to be compared.

Thus, the objectives will justify the chosen thesis title “Band gap engineering of TiO₂ for efficient water splitting to generate hydrogen”.

Experimental Techniques

To arrive at a comprehensive understanding of the material properties, it is important to choose the right characterization tools. Proper choice of operating conditions, understanding sources of errors, accurate interpretation of results are all equally important in the process of material characterization. In line with this, the current chapter gives details of the experimental techniques adopted for the study of band engineered triphase TiO₂ nanotubes.

2.1 Introduction

The Chapter deals with the brief description of the experimental techniques and procedures employed for the synthesis, characterization and application of the band engineered titania nanotube powders in photocatalytic hydrogen generation. The synthesis of pristine and modified triphase TiO₂ nanotubes were carried out using electrochemical anodization facility whose details are explained. Following this, the major characterization techniques for structural (XRD, Raman spectroscopy, TEM), morphological (FESEM), elemental (XPS), energy band gap (UV-Visible absorption spectroscopy), band edge (UPS, Synchrotron VB spectra), band bending (MS plots) and PL analysis are briefly discussed. In addition, the basic features of the hydrogen generation reactor are presented.

2.2 Rapid Breakdown Anodization (RBA)

TiO₂ nanotube powders are synthesized by potentiostatic RBA technique using titanium and platinum foils as the working and counter electrodes (two electrode configuration), respectively, in 0.1 M perchloric acid electrolyte as represented in Figure 2.1. Before performing the experiment, the titanium foil (0.5 mm thickness, 99% pure, cut to the size of area 2.5 x 0.5 cm²) is polished smoothly to remove the oxide layer on the surface. The polished foils are ultrasonicated in alcohol, acetone followed by distilled water and dried in N₂ gas stream. A programmable DC power supply (Agilent N6700 series) and a multimeter (Agilent 34401A) interfaced to computer were used for DC voltage supply and measurement of current transients respectively. All anodization reactions were performed under potentiostatic conditions in perchloric acid medium. The TiO₂ nanotube powders obtained in the present work is synthesized at voltages equal to or above 9.5 V as it is the threshold voltage, below which no TiO₂ nanopowders are seen to fall into the solution. The

TiO₂ powders obtained were washed several times in distilled water, followed by overnight drying at 70 °C and labeled accordingly.

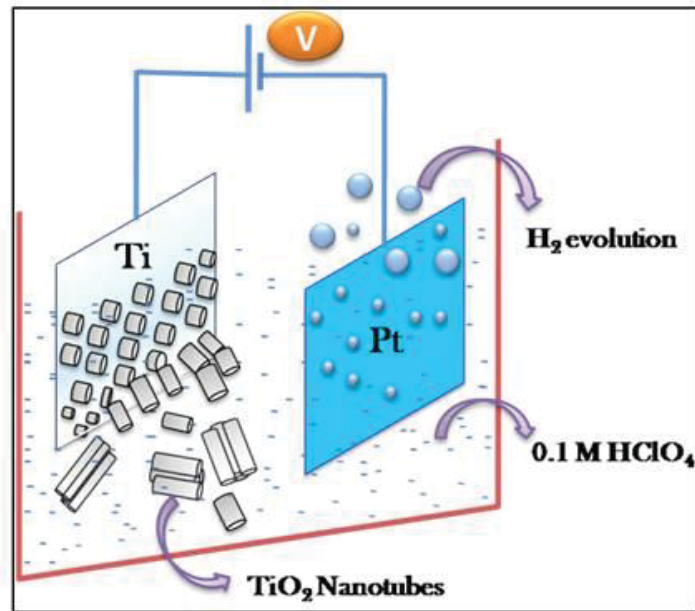


Figure 2.1 Schematic of potentiostatic RBA technique

2.3 X-Ray Diffraction (XRD)

When electromagnetic rays are incident on a solid material (grating), they are either coherently/in-coherently scattered or absorbed. The coherent scattering of rays can interfere with each other giving bright (constructive interference) and dark (destructive interference) fringes. Since X-rays have wavelength comparable to inter-atomic spacing in a crystal, it can interact with the solid and scatter to produce a diffraction pattern. However, the scattered rays will become constructive only at a particular angle when the path difference between the two rays differs by an integral number of wavelengths. This condition for constructive interference of X-rays is termed as Bragg's law which is represented as¹⁸⁵:

$$2d \sin \theta = n\lambda \quad (2.1)$$

where d is the inter-planar spacing (i.e. spacing between adjacent planes in a set of planes, as given in Figure 2.2), θ represents the angle of incidence, n the integer representing the order of diffraction, and λ represents the wavelength of the X-ray (normally Cu $K\alpha = 1.54056 \text{ \AA}$). Generally, the diffraction pattern is plotted as intensity versus diffraction angle 2θ . The X-ray diffractometer typically uses Bragg-Brentano geometry for recording the diffraction pattern. Each peak in the diffraction pattern can be correlated to a set of planes in a crystal lattice. A schematic representation of the X-ray Diffraction (XRD) in crystal planes is shown in Figure 2.2. In powder XRD, the X-rays can penetrate the material from 0.1 to 10 mm depth depending on the material type and the incident X-ray energy. In the present study, observed diffraction patterns of titania nanopowders were compared with JCPDS (Joint Committee on Powder Diffraction Standards, 1974) files corresponding to anatase: 21-1272; rutile: 21-1276 and brookite: 29-1360.

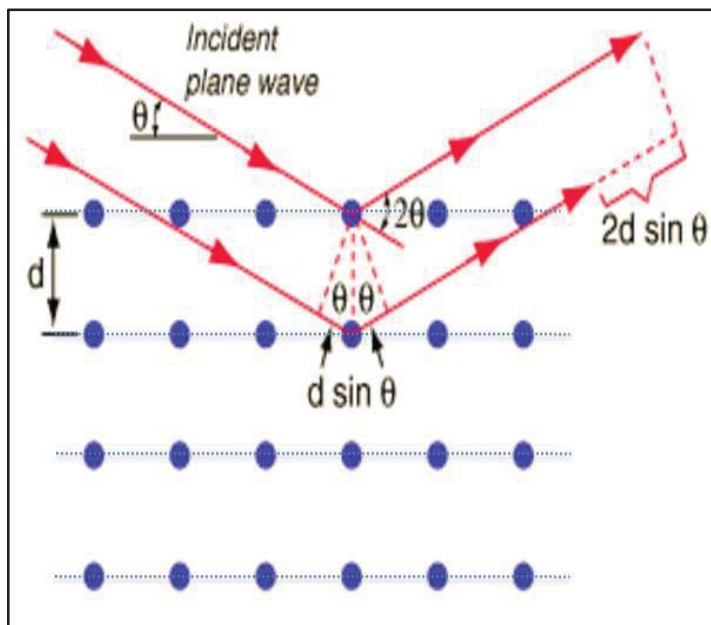


Figure 2.2 Schematic representation of XRD

Width of the diffraction peaks signifies the dimension of the reflecting planes. It is known that the width of a diffraction peak increases when the crystallite size is reduced below a certain limit (<100 nm). Therefore, XRD patterns can be used to estimate the average crystallite size by using Scherrer formula which is given as¹⁸⁶

$$t = \frac{0.9 \lambda}{\beta \cos \theta_B} \quad (2.2)$$

where t is the thickness of the crystal (in Å), λ the X-ray wavelength, and θ_B the Bragg angle in radians. Broadening β is calculated by taking the full width half maximum (FWHM) of the diffraction peak corresponding to each plane in the diffraction pattern. The phase identifications of all the samples in this thesis work are carried out using X-Ray Diffractometer (D8, Bruker) with a scanning range from $2\theta = 20^\circ$ to 80° .

Further Synchrotron XRD measurements were carried out for TiO₂ nanotube powders synthesized at different voltages in RBA technique for the phase composition analysis. The high brilliance of synchrotron source compared to conventional source and superior signal to noise ratio is been exploited for identification of phases whose signal is weak due to its high orientation when laboratory XRD is used. The measurements were recorded in transmission geometry using Image Plate area detector at ambient temperature and pressure using ADXRD beamline on Indus-2 synchrotron source at RRCAT, Indore, India. For this purpose, the angle dispersive mode with a wavelength, $\lambda = 0.82 \text{ \AA}$ is used. The beamline consists of adaptive focusing optics and Si(111) based double crystal monochromator. A MAR345 imaging plate system was used and this image plate data was further processed with automated software FIT2D by integrating over full circle, to obtain the 2 dimensional XRD data. The center of the pattern has been fixed carefully to minimize

the possible error. The calibration of the X - Ray photon energy and the distance between the sample and the image plate was carried out by using standard LaB₆ and CeO₂ samples.

In the present study, TiO₂ nanotubes having anatase-rutile-brookite phases are synthesized. From XRD pattern, the individual phase composition of the triphase samples can be determined using the equations¹⁸⁷:

$$Wa = KaAa/(KaAa + Ar + KbAb) \quad (2.3)$$

$$Wr = Ar/(KaAa + Ar + KbAb) \quad (2.4)$$

$$Wb = KbAb/(KaAa + Ar + KbAb) \quad (2.5)$$

where Wa , Wr and Wb represent mass fractions of anatase, rutile and brookite, respectively; Aa , Ar and Ab represent the integrated intensities of anatase (101), rutile (110) and brookite (121) respectively. Ka and Kb stands for correction coefficients whose values are 0.886 and 2.721 respectively¹⁸⁷. After deconvoluting the overlapping anatase (101) and brookite (120) peaks, calculations are performed using the above formula to calculate the individual phase composition.

The theoretical band gap of nanocomposite materials could be accurately determined using the XRD data (ie mass fraction of each polymorph) and band gap energies of individual polymorphs (anatase, rutile, brookite) using equation:

$$Eg(ARB) = Eg(A)Wa + Eg(R)Wr + Eg(B)Wb \quad (2.6)$$

where Eg represents band gap energy for each material (A-Anatase, R- rutile, B- brookite, ARB – anatase/rutile/brookite nanocomposite)¹⁶⁰.

2.4 Raman Spectroscopy

Vibrational spectra obtained using Raman spectroscopy is the fingerprint of the sample through which its physical and chemical information can be delineated. In 1928, an Indian physicist Chandrashekhara Venkata Raman discovered the phenomena of inelastic scattering of light, known as the Raman effect. This explains the change of wavelength exhibited by some of the radiation scattered by a medium. The degree of shift is specific to chemical structure of the molecules responsible for scattering¹⁸⁸.

Raman spectroscopy utilizes scattered light to gain knowledge about molecular vibrations which can provide information regarding the structure, symmetry, electronic environment and bonding of the molecule, thus permitting quantitative and qualitative analysis of the individual compounds. The irradiation of a molecule with a monochromatic light always results in two types of light scattering, elastic and inelastic. In elastic scattering, there occurs no change in photon frequency. Conversely, in inelastic scattering which is accompanied by the shift in photon frequency due to excitation or deactivation of molecular vibrations where the photon may lose some amount of energy or gains energy.

Thus, three types of phenomena can occur when light is scattered by a medium. First, when light is incident on a molecule, it can interact with the molecule but the net exchange of energy is zero, so the frequency of the scattered light is same as that of the incident light. This process is known as Rayleigh scattering. Second, the light can interact with the molecule and the net exchange of energy is the energy of one molecular vibration. If the interaction causes the light photon to gain vibrational energy from the molecule, then the frequency of the scattered light will be higher than that of the incident light, which is termed

as anti-Stokes Raman scattering. Third, if the interaction causes the molecule to gain energy from the photon, then the

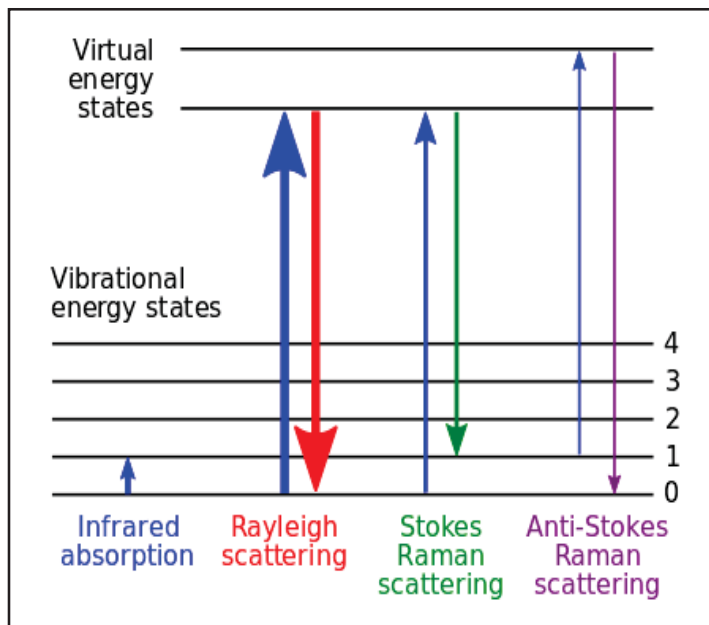


Figure 2.3 Schematic of Raman scattering process

frequency of the scattered light will be lower than that of the incident light, this process is known as Stokes Raman scattering.

The two spectra (Stokes and anti-Stokes) are mirror images on opposite sides of the Rayleigh line. However, because anti-Stokes scattering depends on the existence of thermally activated vibrations, their intensities are strongly temperature dependent; whereas the Stokes intensities are only weakly temperature dependent. For this reason, anti-Stokes scattering is rarely measured, except for the specialized technique known as coherent anti-Stokes Raman spectroscopy. The schematic of the Raman scattering process is given in Figure 2.3. Raman spectra bring direct results from the sample without the need for specific sample preparation and also it is a non destructive technique. Hence it is a time saving and cost effective technique for structural analysis.

All the Raman spectra presented in the thesis were recorded on a micro-Raman spectrometer (inVia, Renishaw, UK), in the back scattering configuration, with Ar⁺ laser (514.5 nm) being used as excitation source, diffraction gratings of 1800 gr·mm⁻¹ for monochromatization and a thermoelectric cooled charged coupled device (CCD) as detector to study the vibrational modes.

2.5 Field Emission Scanning Electron Microscopy (FESEM)

Electron microscopy is based on the interaction between the electrons (matter wave) and the sample. This utilizes the advantage of significantly short wavelength of the electrons which can be focused with the help of electromagnetic lenses to generate highly magnified images. Scanning electron microscopy (SEM), which can produce high resolution images of the surface of a sample, is widely used to analyze the surface morphology of synthesized materials. It is a type of electron microscopy that images a sample by scanning its surface with a focused beam of high energy electrons (e^-).

An accelerated beam of e^- s with a high potential difference impinges on the target material under consideration resulting in consequent elastic and inelastic interactions (Figure 2.4).¹⁸⁵ The elastically backscattered electrons (BSEs), which are emitted through an angle more than 90° possess energy comparable to the primary e^- beam. By convention, if the energy of the emitted e^- is greater than ~50 eV, then it is considered as BSE. Whereas, in the case of the inelastic scattering, a little amount of energy of primary e^- beam is transferred to the target atom. If the energy transferred to the target atom exceeds the work function of the material, then it can knock out additional e^- s, which can escape from the solid surface, those are termed as secondary electrons (SE). The energy of these SEs is less than ~50 eV. Most of

the emitted SEs is produced within the first few nm scale of the surface. By detecting and scanning the BSE and SE, the

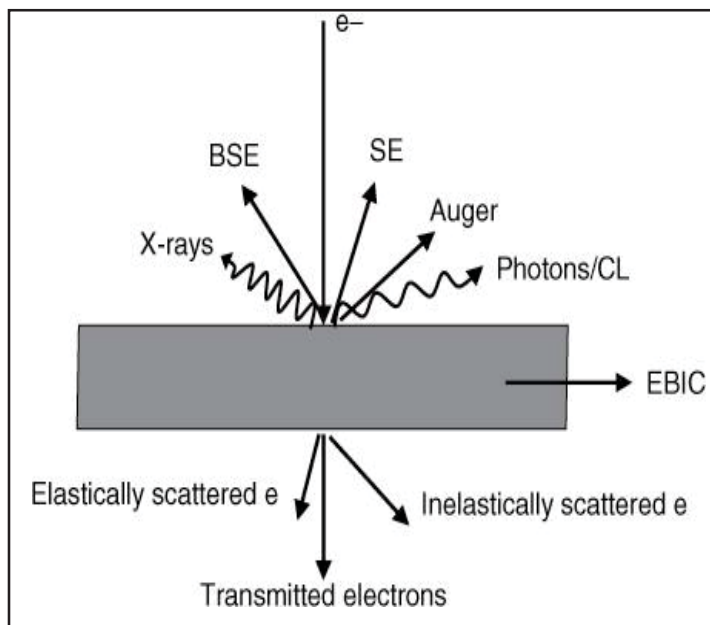


Figure 2.4 Schematic of the effect of high energy e^- beam interaction with the material

image formation can be carried out for the topography and Z-contrast variations in the sample. Thus, in SEM, the primary incident electrons coming from electron gun strike the surface of the sample and interact with the surface atoms of the tested sample, giving rise to electron emission that reveal information about surface morphology and electrical conductivity. The morphological studies of the all the TiO_2 nanotubes samples reported in the thesis were carried out using FESEM (SUPRA 55 Zeiss and JEOL 6360) with 30 kV source from a tungsten field emission (FE) tip.

2.6 Transmission Electron Microscopy (TEM)

As discussed in the previous section, when high energy electrons interact with the specimen, various phenomena occurs as shown in Figure 2.4. SEM involves the investigation of elastically backscattered electrons (BSEs) and secondary electrons (SE). On the other hand, TEM involves investigation of the transmitted electron from a thin sample and reveals information about its morphology and particle size distribution at a spatial resolution of 1.4 nm.

A TEM setup basically consists of an electron gun, voltage generator, vacuum system, electromagnetic lenses and recording devices whose schematic is given in Figure 2.5a. Usually thermionic gun (tungsten filament, LaB6 crystal) or field emission gun is used as an electron source to illuminate the sample specimen. The acceleration voltage of the electrons determines the wavelength of the electron beam, which in turn governs the resolution of the electron microscope. The electron beam after passing through the condenser lens system is directed towards a thin sample. Typically TEM specimen thickness is in the range of 50 to 100 nm for it to be electron transparent. The microscope column is maintained at high vacuum levels to prevent scattering of electrons by the atmosphere inside the microscope. The diffraction pattern and image are formed at the back focus plane and image plane of the objective lens. Information is obtained from both transmitted electrons (i.e. image mode) and diffracted electrons (i.e. diffraction mode) whose schematic is given in Figure 2.5b. A transmitted beam combined with one or more diffracted beam gives a bright field image, whereas a dark field image is obtained from a transmitted beam alone or one of the diffracted beams. Some of the diffraction patterns are from a selected area of the specimen which is termed as selected area electron diffraction (SAED) patterns.

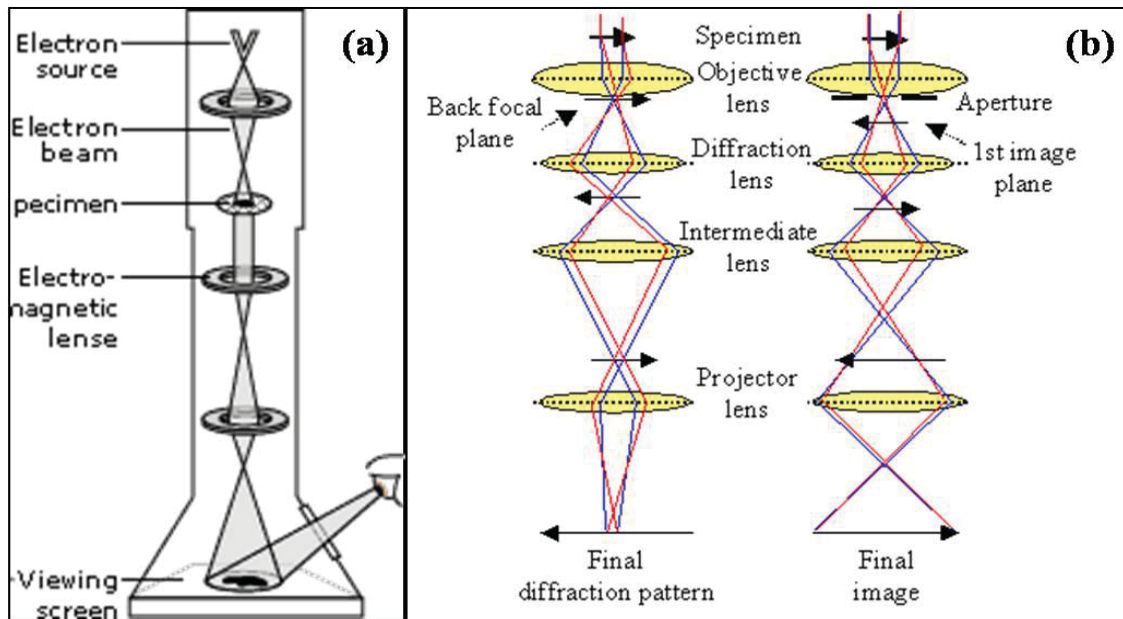


Figure 2.5 (a) Basic set up of TEM; (b) Different modes of TEM

High resolution TEM (HRTEM) on the other hand, requires both high instrumental resolving power and high image contrast. In case of HRTEM, transmitted beams along with at least one diffracted beam is admitted by using a large-diameter objective diaphragm. All of the beams passing through the objective aperture are then made to recombine in the image-forming process, in such a way that their amplitudes and phases are preserved. When viewed at high-magnification, it is possible to observe contrast in the image in the form of periodic fringes. These fringes represent direct resolution of the Bragg diffracting planes. Thus this mode of contrast is referred to as phase contrast. The fringes that are visible in the high-resolution image originate from those planes that are oriented as Bragg reflecting planes and possess interplanar spacing greater than the lateral spatial resolution limits of the instrument.

TEM (JEOL, 2010) was employed for the morphological and structural characterization of all the samples investigated for the present work.

2.7 Ultraviolet-Visible absorption spectroscopy

The band gap (E_g) is an important feature of semiconductors which determines their application in photocatalysis. The UV-Visible spectrum can be used to measure the band gap of any material. In samples, where light penetrates and initiates different processes such as reflection, refraction and diffraction, and eventually emerges out diffusively (scatters in all directions), UV –Visible spectroscopy in transmission mode becomes difficult to execute. In such cases, diffuse reflectance spectroscopy (DRS) is adopted. The difference in these techniques is that in UV-Visible spectroscopy in transmission mode, one measure the relative change of transmittance of light as it passes through a solution, whereas in diffuse reflectance, one measures the relative change in the amount of reflected light off a surface.

There are different methods for determining the band gap using DRS^{189,190}. Among the various methods, Tauc plot^{190,191} is widely used to determine the band gap of the materials in which $(\alpha hv)^n$ is plotted as a function of hv where α represents the absorption coefficient of radiation, h is the Planck's constant and ν is the frequency of the radiation. The value of n is either 2 or $\frac{1}{2}$ depending on the direct and indirect transition behavior respectively¹⁹².

In the case of thick samples, Kubelka Munk function (KM) is used to convert the diffuse reflectance measurements to equivalent absorption coefficient¹⁹³ using the equation:

$$KM = \frac{(1-R)^2}{2R} = \frac{\alpha}{S} \quad (2.7)$$

where R is the ratio of the intensities of radiation reflected in diffuse manner from the sample and from the reference sample, and S is the scattering factor. When the thickness of the sample is much bigger than the individual particle of the sample, S is approximately

unity or it assumes a constant value. Therefore, the KM function will be almost equal to the absorption coefficient α .

For different transition mechanisms, it has been proved that along the sharp absorption edge, the energy of incident photons ($h\nu$) and E_g of a semiconductor will have the relation

$$(\alpha h\nu)^n = A(h\nu - E_g) \quad (2.8)$$

Since the re-emission function (scattering factor S) is equal to the absorption coefficient according to the equation 2.7, the Tauc plot, $(\sqrt{\alpha h\nu})$ versus $h\nu$ can be replaced by $(\sqrt{KB * h\nu})$ versus $h\nu$. Therefore, using reflectance values of UV-Visible radiation, we can calculate the band gap of semiconductors using the above relation.

In the present thesis work, an UV Vis spectrometer (PerkinElmer, Lambda 750S) equipped with a 60 mm diameter integrated sphere in reflectance mode is used for band gap measurements, with barium sulphate as the reference. The powder samples and barium sulphate are loaded into their respective sample lid and tightly packed which then are exposed to UV-Vis light for reflectance measurements.

2.8 Photoluminescence (PL) Spectroscopy

Many materials are capable of emitting visible luminescence when subject to electromagnetic radiation. This process is termed as photoluminescence (PL). PL spectroscopy is a powerful technique for investigating the electronic structure, both intrinsic and extrinsic, of semiconducting and semi-insulating materials. There are two pre-requisites for luminescence: (a) the luminescent material must have a nonzero E_g and (b) energy must be imparted to this material before luminescence can take place. The PL mechanism in

semiconductors is schematically illustrated in Figure 2.6 which plots the E - k diagrams for direct and indirect band gap semiconductors, where E and k are the kinetic energy and wave vector (or momentum vector) of the electron or hole. The direct and indirect band gap semiconductors are distinguished by their relative positions of CBM and VBM in the Brillouin zone. In a direct band gap material, both CBM and VBM occur at the zone center where $k = 0$. In an indirect band gap material, however CBM doesn't occur at $k = 0$, but rather at some other values of k which is usually at the zone edge or close to it¹⁹⁴.

Upon absorption of a UV or visible light photon with an energy exceeding the band gap E_g of the material, an electron-hole pair is created where the electron is excited to states high up in the CB. During a photon absorption process in semiconductors, both energy and momentum should be conserved. In a direct band gap material, CBM and VBM have the same k values; conservation of momentum is guaranteed for the photoexcitation of the electron which only involves a UV or visible photon:

$$\hbar k_i + \hbar k_{\text{photon}} \approx \hbar k_i = \hbar k_f \quad (2.9)$$

where k_i and k_f are the wave vectors of the initial and final electron states. Since $\hbar k_{\text{photon}}$, the wave vector of the absorbed photon (which is in the order of $2\pi/\lambda \approx 10^5$) is negligible compared to the electron wave vector (which is related to the size of the Brillouin zone $\pi/a \approx 10^8$, where the unit cell dimension ' a ' is in the order of few angstroms). This implies that in a direct band gap material, the electron wave vector doesn't change significantly during a photon absorption process. Therefore the photon absorption process is represented by vertical arrows in the E- k diagrams.

In contrast, for an indirect band gap material of which the CBM and the VBM have different k values, conservation of momentum implies that the photon absorption process

must be assisted by either absorbing or emitting a phonon, because the electron wave vector must change significantly in jumping from VB to CB and the absorption of a photon alone cannot provide the required momentum change since $|k_{photon}| \ll |k_i - k_f|$. The excited electron and hole cannot remain in their initial excited states for very long, instead, they will relax very rapidly to the lowest energy states within their respective bands by emitting phonons. When the electron finally arrives at the bottom of the CB, the electron-hole pair can recombine radiatively with the emission of a photon giving rise to luminescence, or nonradiatively by transferring the electron's energy to impurities or defects in the material or dangling bonds at the surface.

Therefore, the photon absorption process in an indirect gap material for which conservation of momentum can be fulfilled by either absorption or emission of a phonon, in the electron-hole recombination process, phonon absorption becomes negligible, whereas phonon emission becomes the dominant mediator for momentum conservation because (1) the number of phonon available for absorption is low and it rapidly decreases at low temperatures, whereas the emission of phonons by electrons which are already at a high-energy state is very probable; and (2) an optical transition assisted by phonon emission occurs at a lower photon energy $E_g - h\nu_{phonon}$ than the energy gap, whereas phonon absorption results in a higher photon energy of at least $E_g + h\nu_{phonon}$, which can be more readily re-adsorbed by the semiconductor. But we note that the energy of a phonon ($h\nu_{phonon}$) is just in the order of ≈ 0.01 eV, much smaller than the energy of the electron-hole recombination luminescence photon. Also because prior to the recombination, the electron and holes respectively accumulate at the bottom of the CB and the top of the VB, the energy separation between the electrons and the holes approximately equals to the

energy of band gap. Therefore, the luminescence emitted by both types of semiconductors occurs at energy close to the band gap E_g .

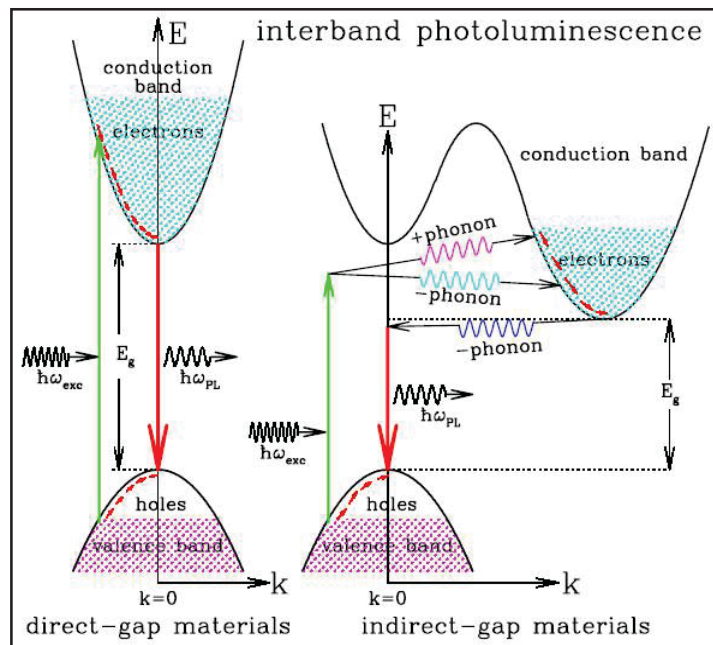


Figure 2.6 Photoluminescence in direct and indirect band gap semiconductors

The PL efficiency is determined by the competition between radiative and nonradiative recombination. For an indirect gap material, the PL process, which requires a change in both energy and momentum for the excited electron and hence involves both a photon and a phonon, is a second-order process with a long radiative lifetime ($\approx 10^{-5} - 10^{-3}$ s), therefore a relative small efficiency because of the competition with nonradiative recombination, In contrast, in a direct gap material, the emission of a PL photon doesn't need the assistance of a phonon to conserve momentum, hence it's a first order process having a much shorter radiative lifetime ($\approx 10^{-9} - 10^{-8}$ s) and a higher PL efficiency than an indirect band gap material.

The PL studies on TiO_2 nanotubes, reported in this thesis, are carried out using the same setup used for the micro-Raman measurements (inVia, Renishaw), by choosing the

He–Cd laser source (325 nm) operating at a power level of 200 mW, a long pass filter, 2400 gr.mm⁻¹ grating and a CCD detector.

2.9 X-ray Photoelectron Spectroscopy (XPS)

The physical and chemical composition of the catalyst surfaces determines the nature of surface - adsorbent interactions. Their surface chemistry will influence factors such as corrosion rates, catalytic activity, adsorption properties, contact potential and reaction mechanisms. XPS is a semi-quantitative technique to determine chemical composition of the materials surface based on photoelectric effect. Each atom in the surface has core electron with the characteristic binding energy that is conceptually, not strictly, equal to the ionization energy of that electron. When an X-ray beam radiated on the sample surface, the energy of the X-ray photon is adsorbed by the core electron. If the photon energy, $h\nu$, is large enough, the core electron will then escape from the atom and emit out of the surface. The emitted electron with the kinetic energy (E_k) is referred to as the photoelectron. The binding energy (E_b) of the core electron is given by the Einstein relationship:

$$h\nu = E_b + E_k + \phi \quad (2.10)$$

$$E_b = h\nu - E_k - \phi \quad (2.11)$$

where $h\nu$ is the X-ray photon energy (for Al K α , $h\nu = 1486.6\text{eV}$); E_k is the kinetic energy of photoelectron, which can be measured by the energy analyzer; and ϕ is the work function induced by the analyzer, about 4~5eV. Since the work function ϕ , can be compensated artificially, it is eliminated, giving the binding energy as follows:

$$E_b = h\nu - E_k \quad (2.12)$$

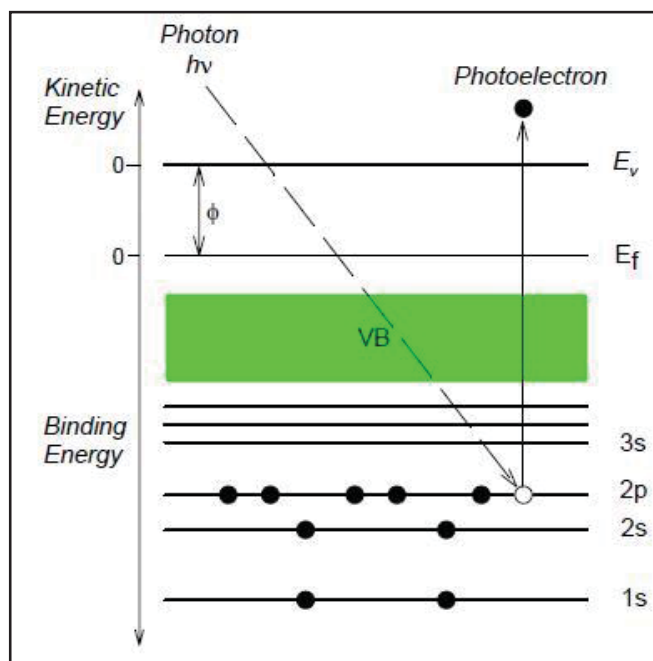


Figure 2.7 Schematic of photoelectron emission

XPS is a widely used technique for obtaining chemical information of various material surfaces. The low kinetic energy ($0 \leq 1500$ eV) of emitted photoelectrons limit the depth from which it can emerge, so that XPS is a very surface-sensitive technique and the sample depth from which electron is emitted is in the range of few nanometers (<10 nm). Photoelectrons are collected and analyzed by the instrument to produce a spectrum of emission intensity versus electron binding (or kinetic) energy. In general, the binding energies of the photoelectrons are characteristic of the element from which they are emanated, so that the spectra can be used for surface elemental analysis. Small shifts in the elemental binding energies provide information about the chemical state of the elements on the surface. The peak area can be used (with appropriate sensitivity factors) to determine the surface compositions of the material. Therefore, the high resolution XPS studies can provide the chemical state information of the surface. Once a photoelectron has been emitted, the

ionized atom must relax in some way. This can be achieved by the emission of an X-ray photon, known as X-ray fluorescence. The other possibility is the ejection of an Auger electron through a secondary process.

All XPS data present in the thesis were collected using hemispherical analyzer EA 15 (PREVAC) equipped with dual anode X-ray source RS 40B1 (PREVAC). The measurements were performed using Al $K\alpha$ (1486.6 eV) radiation and analyzer pass energy of 100 eV. The electron binding energy (BE) scale was calibrated at the maximum of C 1s core excitation at 285 eV. The ultra-high vacuum (UHV) conditions of $1 \cdot 10^{-9}$ mbar were maintained during the measurements.

X-ray photoelectron spectrometer (XPS) (SPECS, Germany) with Al $K\alpha$ X-ray source (1486.74 eV) is also used for some other set of samples (TiO_2 synthesized with different voltages). In this XPS set up, the photoelectron energy spectra were collected using the PHOIBOS 150 MCD-9 analyzer with a resolution of 0.67 eV for 656 keps at a pass energy of 12 eV.

2.10 Ultra-violet Photoelectron Spectroscopy (UPS)

UPS is analogous to XPS except that it uses Helium discharge source for excitation. Depending on the operating conditions of the source, the photon energy can be optimized for He I = 21.22eV or He II = 44.8eV which is significantly lower energy than Al or Mg $K\alpha$ used in XPS. As lower energy photons are used, most core level photoemissions are not accessible using UPS, so spectral acquisition is limited to VB region of the material. There are two types of experiment performed using UPS: (1) VB acquisition and (2) electronic work function measurement.

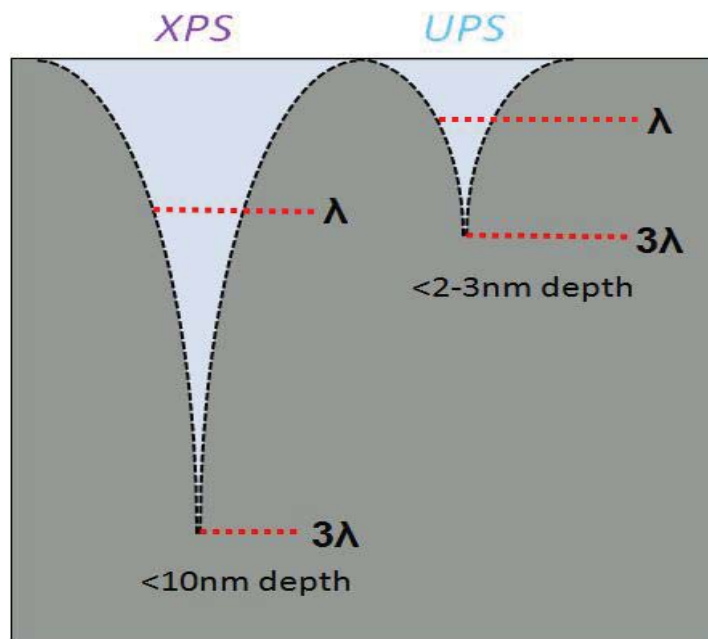


Figure 2.8 Difference in information depth for XPS and UPS

UPS also exhibits greater surface sensitivity than XPS. The inherent surface sensitivity of XPS is due to the shorter inelastic mean free path (IMFP, or λ) of free electrons within a solid, with the so-called 'information depth' from which $> 99\%$ of photoemission signal originates. For UPS, the conventional mean free path is being defined as 3 nm from the surface, whereas for XPS, it is often quoted as 10 nm. The values are an approximation as the IMFP of an electron is determined by the material properties of the solid media through which it is travelling and its kinetic energy. The lower incident photon energies used in UPS emit photoelectrons of much lower kinetic energies than those measured in XPS, therefore UPS spectra provides an approximate information depth of 2-3nm. Figure 2.8 shows the difference between XPS and UPS with respect to surface sensitivity.

The difference between the FL and Vacuum level is referred to as the electronic work function, a material property applied in the development of electronics devices, for example where matching of VB and CB in multilayered devices is required. As a surface property, the work function is strongly influenced by variation in composition or structure at the surface, such as atmospheric contamination.

The UPS study in the present work is carried out for VB edge analysis. The UPS set up used for the present work consists of discharge UV source UVS 40A2 (PREVAC), which produces the characteristic excitation line He I α (21.2 eV). The analyzer pass energy of 10 eV, at a chamber pressure better than 10^{-8} mbar is used.

In order to distinguish the VB edges of three phases present in triphase TiO₂ nanotubes, high resolution VB edge spectra using synchrotron radiation source is sought. The VB spectra were measured with angle resolved photoelectron spectroscopy (ARPES) beam line (BL-3) at Indus-1 synchrotron radiation source, RRCAT, Indore, India. Vacuum in the analysis chamber was better than 3×10^{-9} mbar during the measurements. The analysis chamber is equipped with SPECS PHOIBOS 150 electron analyzer. UPS spectrum from Au foil was used as a reference to characterize the monochromatic synchrotron light from the beamline.

2.11 Electron Paramagnetic Resonance Spectroscopy (EPR)

EPR spectroscopy, also called electron spin resonance (ESR) spectroscopy, is a technique used to study chemical species with unpaired electrons. EPR spectroscopy plays an important role in understanding both organic and inorganic radicals, transition metal

complexes and even some biomolecules. In photocatalysis, EPR studies are carried out to study the defects present in the sample.

When a molecule with an unpaired electron placed in a magnetic field, aligns its spin in two different ways giving rise to two spin states, $m_s = \pm 1/2$. The alignment can either be parallel to the magnetic field which corresponds to the lower energy state $m_s = -1/2$ or antiparallel to the

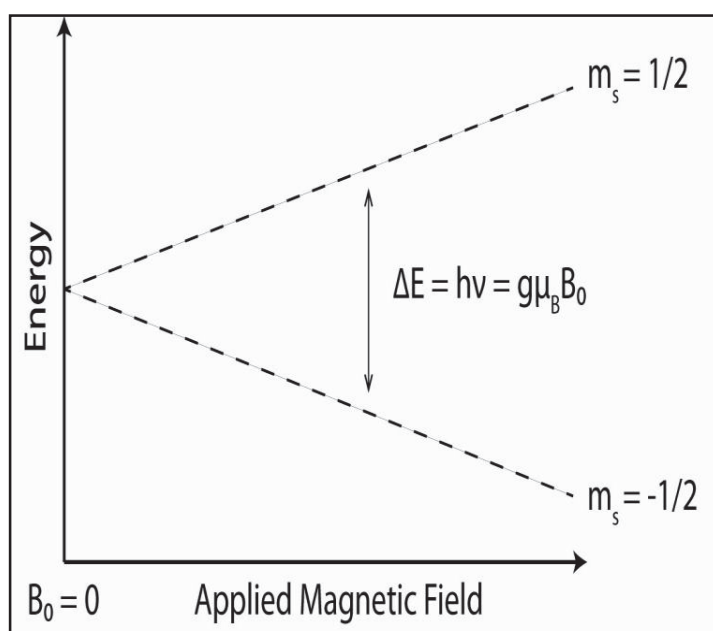


Figure 2.9 Energy levels for an electron spin ($m_s = \pm 1/2$) under magnetic field direction of applied magnetic field $m_s = +1/2$ (Figure 2.9). The two alignments have different energies and this difference in energy lifts the degeneracy of the electron spin states. The energy difference is given by:

$$\Delta E = E^+ - E^- = h\nu = g\mu_B B_0 \quad (2.13)$$

where h is the Planck's constant, ν is the radiation frequency, μ_B is the Bohr magneton ($9.274 * 10^{-24} \text{ JT}^{-1}$), B_0 is the magnetic field strength (in Tesla) and g is called the g factor. The g -factor is a unit less parameter of the intrinsic magnetic moment of the electron and its

value for a free electron is 2.0023. During the experiment, the values of h , ν and μ_B doesn't change whereas g value changes with change in magnetic field strength B_0 . The EPR spectrum is the absorption of microwave frequency radiation plotted against the magnetic field intensity.

In an EPR experiment, the magnetic field of the magnet is varied linearly to excite some of the electrons in the lower energy level to the upper energy level while the sample is exposed to fixed microwave radiation. The free or the unpaired electrons having magnetic moment align parallel to the larger field produced by the spectrometer's magnet. At a particular magnetic field strength, the microwave irradiation will cause some of the free electrons to flip and orient against the applied magnetic field. This separation between the lower and the higher energy level is exactly matched by our microwave frequency. The condition where the applied magnetic field and the microwave frequency are just coinciding to produce EPR resonance (or absorption) is known as the resonance condition and is detected by the spectrometer. EPR spectroscopic measurements can be carried out either by varying the magnetic field keeping the frequency constant or vice versa. Typically, in commercial EPR spectrometer, microwave frequency is held constant and the applied magnetic field is varied to record the spectrum.

EPR experiments in the thesis work were performed using a Jeol JES X310 ESR spectrometer, Japan at an operating frequency of 9.4GHz. The EPR measurements were taken at room temperature with the powder sample kept in 4mm OD quartz EPR tubes. The g -value was calibrated with standard DPPH (a, a0 -diphenyl-b-picryl hydrazyl) and is used as a field marker.

2.12 Mott-Schottky Analysis

Fundamental studies on photoelectrochemical properties of semiconductor are required in order to understand its behavior in photocatalysis. When a semiconductor is immersed in a redox electrolyte, the electrochemical potential is disparate across the interface. In order for the two phases to be in equilibrium, their electrochemical potential should match each other. The electrochemical potential of the solution is determined by the redox potential of the electrolyte species, whereas that of semiconductor is determined by its FL. In order to equilibrate the redox potentials of two phases, the charges migrate between the semiconductor and the solution.

The excess charge that is now located on the semiconductor does not lie at the surface rather it extends into the electrode for a significant distance (100- 10,000 Å). This region is referred to as the “space charge region”, which gives rise to inbuilt electrical field. Hence, two double layers develop when the semiconductor is immersed in electrolyte solution: the interfacial (electrode/electrolyte) double layer, and the space charge double layer.

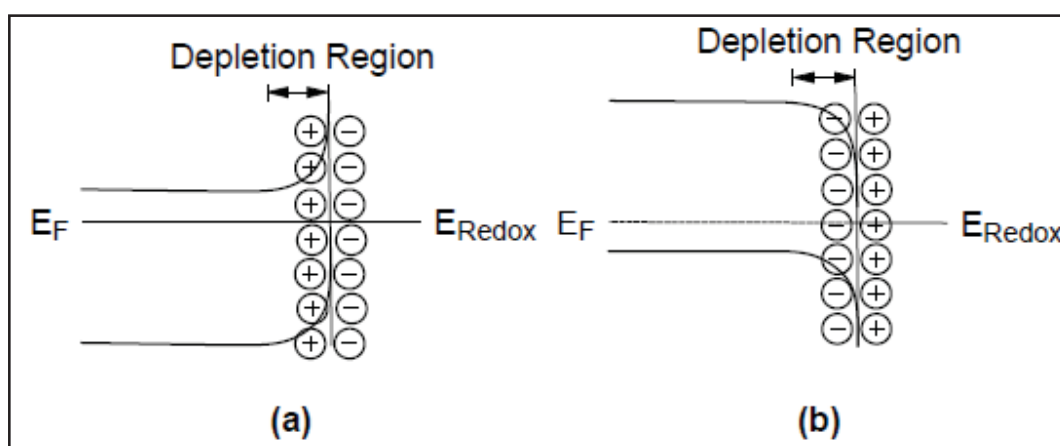


Figure 2.10 Band bending of (a) n-type and (b) p-type semiconductor in equilibrium with redox potential of electrolyte.

The FL of n-type semiconductor is in general higher than the redox potential of the electrolyte under open circuit condition and hence electrons will be migrated from the electrode into the solution. This develops a positive charge in the space charge region which leads to the upward bending of the band edges as shown in Figure 2.10a. Since the region is devoid of majority charge carriers, it is also referred to as “depletion layer”. For a p-type semiconductor, the FL is lower than the redox potential hence reverse reactions takes place leading to the downward bending in the band edges as represented in Figure 2.10b.

The FL of metallic electrodes can be altered by changing the potential applied to the electrode. Similar way, the band edges in the semiconductor interior (i.e., away from the depletion region) also vary with the applied potential whereas the one at the interface doesn't undergo any change. Therefore, the magnitude and direction of band bending, varies with the applied potential. There are three different situations to be considered in the semiconductor/electrolyte under applied potential:

- a) At a certain potential, the FL of semiconductor lies at the same energy as the redox potential of the electrolyte (Figure 2.11 b). There is no net transfer of charge, and hence there is no band bending. This potential is therefore referred to as the flatband potential, E_{fb} .
- b) Depletion regions arise at potentials positive of the flatband potential for an *n*-type semiconductor (Figure 2.11 a) and vice versa for a *p*-type semiconductor.
- c) At potentials negative of the flatband potential for an *n*-type semiconductor, excess of majority charge carriers (electrons) generated in this space charge region, which is referred to as an accumulation region (Figure 2.11c). An accumulation region arises in a *p*-type semiconductor at potentials more positive than the flatband potential.

The charge transfer abilities of a semiconductor electrode depend on whether there is an accumulation layer or a depletion layer. If there is an accumulation layer, the behavior of a semiconductor electrode is similar to that of a metallic electrode, since there is an excess of majority charge carrier available for charge transfer. In contrast, if there is a depletion layer, then there are few charge carriers available for charge transfer, and electron transfer reactions occur

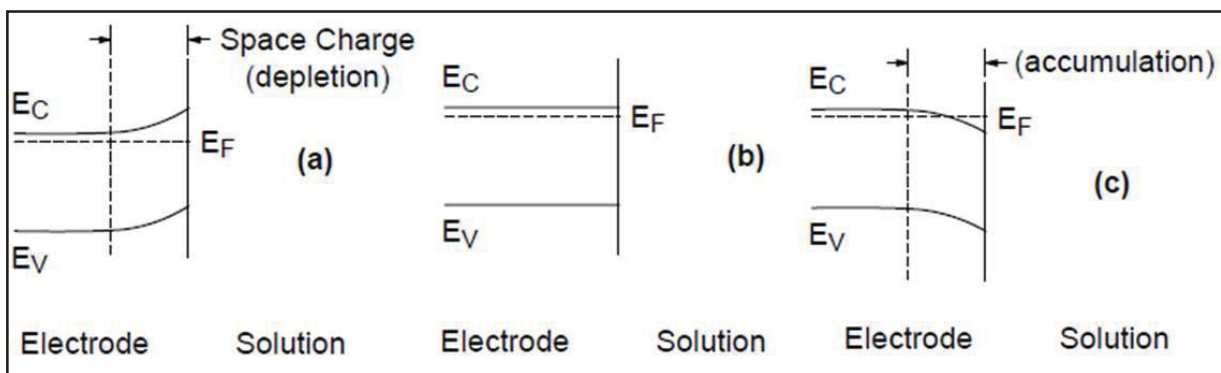


Figure 2.11 Effect of varying the applied potential on band edges in the interior of a n-type semiconductor (a) $E > E_{fb}$ (b) $E = E_{fb}$ and (c) $E < E_{fb}$

slowly, if at all. However, if the electrode is exposed to radiation of sufficient energy, electrons can now be promoted to the CB. If this process occurs in the interior of the semiconductor, recombination of the promoted electron and the resulting hole typically occurs, together with the production of heat. However, if it occurs in the space charge region, the electric field in this region will cause the separation of the charge. Therefore estimating the E_{fb} gives information about the band edge and charge transfer properties of the semiconductor at the electrolyte interface.

There are many methods to determine E_{fb} . Among them, determining the apparent capacitance of the semiconductor/electrolyte interface as a function of applied potential

under depletion condition called MS analysis is widely used. The MS relationship¹⁶ is defined as;

$$(C_{sc})^{-2} = \frac{2(E - E_{fb} - \frac{kT}{e})}{N_D \epsilon \epsilon_0 e A^2} \quad (2.14)$$

where C_{sc} is space charge capacitance, N_D represents the charge carrier density of the sample, ϵ is the dielectric constant of the sample (100 for TiO₂ nanotubes), ϵ_0 is the permittivity in vacuum and A represents the active surface area of the exposed electrode. The value of E_{fb} is calculated from the intercept extrapolating a straight line from $1/C^2$ versus potential plot.

2.13 Photocatalytic Hydrogen Generations

Solar water splitting reactions were carried out in order to prove the photocatalytic activity of the materials. The hydrogen generation experiments are carried out by dispersing 10 mg of the photocatalyst in ethanol-aqueous solution (1:4 ratio) in a quartz photocatalytic cell of 50 mL capacity sealed with a rubber septum. The suspension is carefully purged with argon for 30 minutes. The quartz cell with dispersed sample is kept at 20 cm away from the solar simulator (equipped with 300 W Xenon arc lamp and AM 1.5 cut-off filter from Newport) to ensure one sun irradiation conditions¹⁹⁵ with an area of illumination to be 12 cm² (Figure 2.12). The generated hydrogen is measured every hour by periodically withdrawing gas samples through the rubber septum followed by quantification using a gas chromatograph (GC, Agilent 7890A) for the total reaction time of 4 hours.



Figure 2.12 Photocatalytic hydrogen generation test done under AM 1.5 illuminations (100 mW/cm²) for 10 mg of photocatalyst in 40 ml aqueous ethanol solution.

The spectral output of the solar simulator with and without AM 1.5G type filter is calibrated to be 1 Sun (100 mW/cm²) and 1.6 Sun (160 mW/cm²).

The solar to hydrogen conversion efficiency (STH) of powder photocatalyst for particulate water splitting at AM 1.5G illumination is measured using the formula¹⁹⁶:

$$STH = \frac{\left(\frac{mmol\ H_2}{s}\right) * \left(\frac{237\ kJ}{mol}\right)}{P_{total} \left(\frac{mW}{cm^2}\right) * Area\ (cm^2)} \quad (2.15)$$

where the denominator is the total power of incident simulative sunlight (AM 1.5G) multiplied by the area irradiated by the incident light, and the numerator is the product of the H₂ evolution rate and the Gibbs free energy for generating one mole of H₂ from water.

2.14 Summary

This chapter provides brief overview of synthesis and characterization techniques adopted to understand the physiochemical properties of TiO₂ nanotube powders and its variants. The microscopic imaging, spectroscopic and electrochemical characterization tools employed are described with their basic functionalities. The experimental set up needed for testing the photocatalytic hydrogen generation ability of TiO₂ nanotubes and their variants are also demonstrated.

Synthesis and Characterization of Band Engineered TiO₂ Heterojunctions

TiO₂, being a wide band gap semiconductor, is universally opted for photocatalytic hydrogen generation application. High electron hole pair recombination and absence of visible light activity are the two major intrinsic issues of this material. The thesis is dedicated to address and attenuate the above issues of titania. Recently, it has been found that the heterostructures formed by various phases of titania exhibit better photoexcited charge pair separation leading to efficient photocatalytic activity compared to single phase titania. In this regard, biphasic titania with different phase compositions are widely studied till date. However, the study on the potential of triphase TiO₂ in water splitting is scarce as it's a rare polymorph.

The present chapter introduces a new route for the simple synthesis of triphase (ARB) TiO₂ nanotubes for efficient photocatalytic hydrogen generation. The effects of experimental conditions over the triphase TiO₂ synthesis are demonstrated. In addition, the chapter also discusses the synthesis of doped and defect induced triphase TiO₂ nanotubes for extending the absorption spectrum to obtain visible light active high quantum efficient photocatalyst.

3.1 Introduction

Even though the water splitting efficiency of TiO₂ is attributed to its energy band characteristics, the physical and chemical properties of TiO₂ are sensitive to the phase composition. TiO₂ has three different crystalline forms viz anatase, rutile and brookite, whose photocatalytic activity is strongly limited by its low quantum efficiency due to fast recombination of excited electron-hole pairs⁷⁴. It has been demonstrated that the effective strategy to inhibit the recombination is to introduce phase junctions in TiO₂ catalyst¹⁶¹. Recent studies have reported that biphasic interfaces such as anatase/rutile,^{16,74,161} anatase/brookite^{162,163} and brookite/rutile¹⁶⁴ perform better in photocatalytic application compared to individual phases. Although triphase (ARB) composition of titania is a rare polymorph and its synthesis involves multiple steps of rigorous reactions / thermal treatment, their importance in photocatalysis is recently realized^{181,197,198}. The phase selection in these synthesis techniques depends on the reactant concentration, temperature and reaction time¹⁸¹⁻¹⁸³. Moreover the triphase TiO₂ obtained by most of these synthesis methods can be easily separated by peptization to individual phase nanoparticles where the efficiency of triphase interface is doubted due to the dispersive nature of the colloids^{160,183,199}.

Unlike the widely studied single or biphasic systems, the reports on water splitting efficiency of triphase (ARB) TiO₂ nanostructures are unavailable. To understand the actual reactivity of triphase TiO₂ nanostructures in the photocatalytic water splitting, a facile synthesis of TiO₂ nanoparticles having three phases in single entity whose phases are not separated by dispersion is highly appreciable. Among the various nanoarchitectures of TiO₂, one dimensional nanostructure is preferred for various photocatalytic applications due to their

high aspect ratio and enhanced electron transport properties^{200,201}. In addition to that, the titania in powder form are favorable as these can be suspended homogeneously in the media facilitating better light harvesting capability and superior reaction kinetics. Therefore having three phases in a single TiO₂ nanotube is advantageous as all phases exist in single entity, providing high aspect ratio with enhanced charge transport properties in water splitting. Of the various techniques available for the synthesis, an electrochemical technique called Rapid Breakdown Anodization (RBA) is adopted in the present work to synthesize triphase TiO₂ nanotube powders, whose phase composition can be varied by varying electrochemical parameters such as synthesis voltage and electrolyte concentration in a very simple experimental set up.

After the remarkable discovery of Asahi et al¹⁴⁰ on band gap engineering of TiO₂ by nitrogen doping to absorb visible light, the effects of nitrogen^{56,101,202-204} and other non metals²⁰⁵⁻²⁰⁷ doping in various TiO₂ nanomaterials are reported. It is found that compared to other non metals, nitrogen doping is more appropriate for extending the photocatalytic activity of TiO₂ into visible region because of its comparable atomic size to that of oxygen, small ionization energy and stability^{208,209}.

Despite the fact that the heterostructures formed by two polymorphs of titania can endure photocorrosion, the composites are active only under UV light. Hence the strategy of coupling binary structure with nitrogen doping has been designed for high quantum efficient visible light photocatalysis, which was well received^{16,210}. Although, there are many reports on visible light active nitrogen doped single and biphasic TiO₂, still there exists lot of space to be covered to obtain a practicable photocatalyst. One such step towards this is to carry out nitrogen doping in triphase TiO₂, to obtain efficient visible light photocatalytic activity.

There are no reports on nitrogen doping in triphase TiO₂ for water splitting applications till date.

Our efforts to synthesize N-doped triphase TiO₂ by annealing the triphase TiO₂ nanotube powders obtained from RBA technique (discussed above), in NH₃ atmosphere resulted in N-doped biphasic TiO₂¹⁶. Efforts to synthesize N-doped triphase TiO₂ at low temperatures through soft chemistry and electrochemical routes using various amines as nitrogen precursor resulted in destruction of tubular structure and carbon contamination. After several trials, use of carbon less precursor in combination with an electrochemical technique is identified to be a potential method for synthesizing visible light active N-doped triphase TiO₂ nanotube powders.

Although it was successful in tailoring the optical properties to visible region, the nitrogen dopant sites often act as recombination centers affecting the photocatalytic efficiency^{16,211}. Recently, dopant free defective TiO₂ has triggered extensive research interest due to the efficient engineering of band gap, towards visible light to infrared absorption²¹²⁻²¹⁵. Hydrogenation of TiO₂ is one such attempt which produced black titania, whose band offsets shifted to match equivalently with the water redox potential^{143,216,217}.

Thus obtaining high photoexcited charge separation by constructing multiple phase junctions in TiO₂ and visible light absorption through hydrogen annealing is a great deal towards the synthesis of high efficient photocatalyst. Many reports are found on the hydrogenation of single phase titania nanoparticles and its photocatalytic properties^{147,216,218}. Similarly there are few reports on the study of hydrogenated biphasic titania²¹². However there are no reports which emphasize the study of hydrogenated triphase titania. The

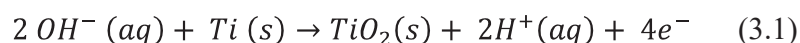
difficulties encountered in synthesis of tailored ARB nanoparticle limit the information on their photocatalytic efficiencies.

Therefore in the present chapter, the synthesis of triphase TiO₂ nanotube powders under varying experimental conditions such as synthesis potential and electrolyte concentration in RBA technique, are discussed. In addition, the chapter focuses on extending visible light absorption in these triphase TiO₂ nanotubes by nitrogen doping using suitable precursor in RBA technique and also by creating native defects through hydrogen annealing at various temperatures. The resultant pristine and modified TiO₂ powders are characterized for its phase composition, structure and optical properties. The work is carried out with an aim to build an ideal photocatalyst by exploiting the multiphase junctions towards charge separation and visible light absorption.

3.2. Synthesis of Triphase TiO₂ Nanotubes

3.2.1 Effect of synthesis voltage

The schematic of TiO₂ nanotube synthesis using RBA technique is shown in Figure 3.1a. As soon as we apply a potential difference between the Ti foil and Pt electrode in HClO₄ solution, an oxide layer grows on the surface of titanium. Below the threshold voltage V_t, the oxidation of titanium proceeds much more rapidly than that of chlorination by the overall anodic reaction



The applied bias voltage causes an inward migration of oxide ions which increases the oxide layer thickness. At low anodization voltage, the oxidation of titanium dominates

that of chlorination even after the formation of a steady state barrier thickness and hence etching of TiO_2 is not observed. The reaction pathway is schematically depicted in Figure 3.1b. At threshold voltage (V_t), the chlorine chemistry begins to compete with the oxygen chemistry causing etching of TiO_2 layer. This in turn, reduces the oxide thickness and the chlorination interferes with the oxide growth mechanism. At this point, we start to observe the TiO_2 powders falling out of the Ti foil into the solution. At higher voltages ($V > V_t$), both chlorine chemistry and oxygen chemistry speed up, leading to rapid increase in reaction rates producing more TiO_2 powders into the solution.

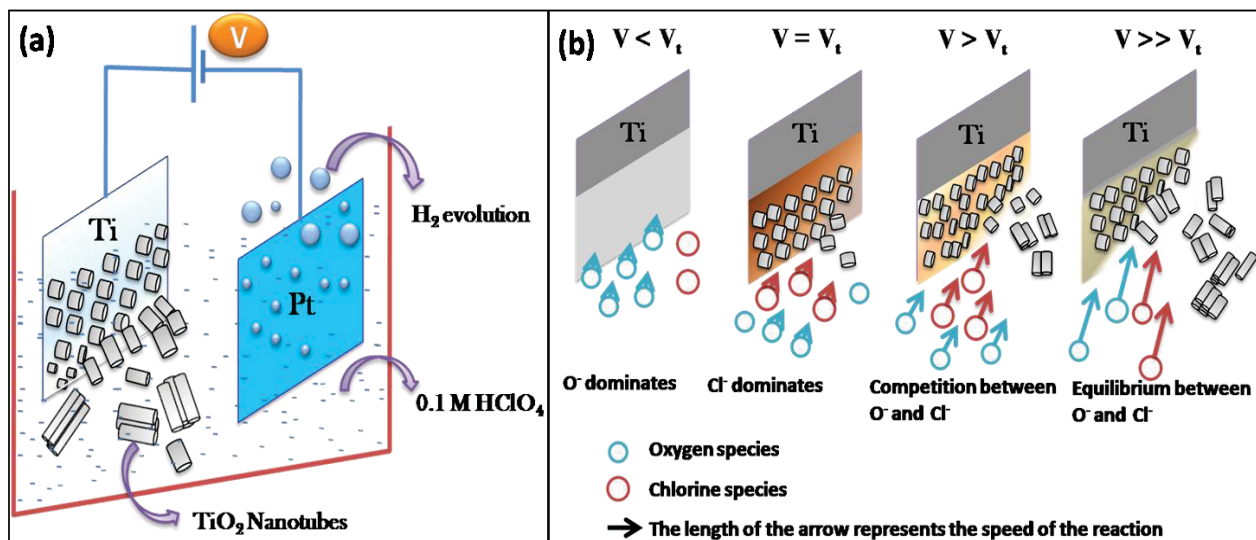


Figure 3.1 (a) Schematic representation of synthesis of TiO_2 nanotubes; (b) A tentative reaction route of the synthesis with respect to voltage

Hence at different voltages there is a rapid change in reaction rates of chlorine species and oxygen species. The earlier reports on RBA technique for the synthesis of nanotubes have concentrated either on the threshold voltage V_t or the much higher voltages ($V \gg V_t$)^{101,219,220}. However, there are no reports which concentrate on the reactions that occur in between these two extremes where the specific phase growth phenomena take place.

Previous studies confirmed the optimum concentration of HClO_4 as 0.1 M for obtaining TiO_2 powders with good tubular morphology¹⁰¹. Hence in order to study the phase formation with respect to voltage, the anodizations were performed at different voltages from 9.5 to 15 V (at 9.5, 10.2, 11, 12 and 15 V) in 0.1 M HClO_4 and the obtained TiO_2 nanotubes are characterized. The synthesis is repeated multiple times and the voltages are constantly monitored to ensure minimum error (± 0.03 V) in the set voltage.

3.2.1.1 Phase evolution

3.2.1.1.1 XRD analysis

The XRD pattern of the TiO_2 powders obtained at different anodization voltages are shown in Figure 3.2. From the XRD patterns, it is evident that the nanotubes obtained at 9.5 V are of anatase phase, with a weak residual rutile phase peak around 54.3° and 69° . The

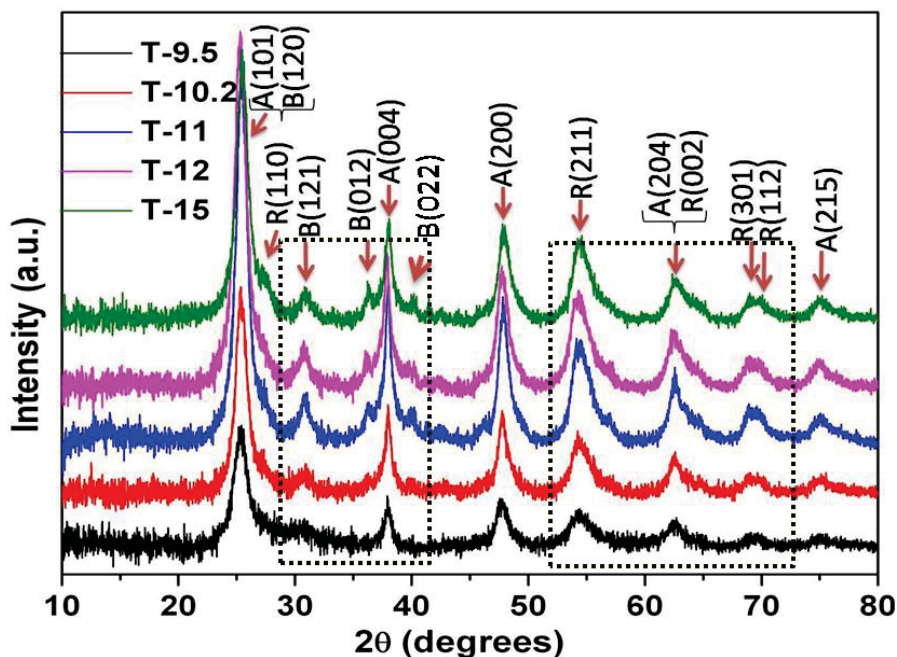


Figure 3.2 XRD of TiO_2 nanotubes synthesized at different voltages.

XRD pattern of samples synthesized at 10.2 V shows diffraction peaks corresponding to strong anatase and rutile peaks. The two phase formation can be attributed to the competition between chlorination and oxidation at moderate speed. As we increase the synthesis potential to 11 V, the peaks corresponding to brookite are evolved along with anatase and rutile peaks. The phase evolution of rutile and brookite with respect to voltage is

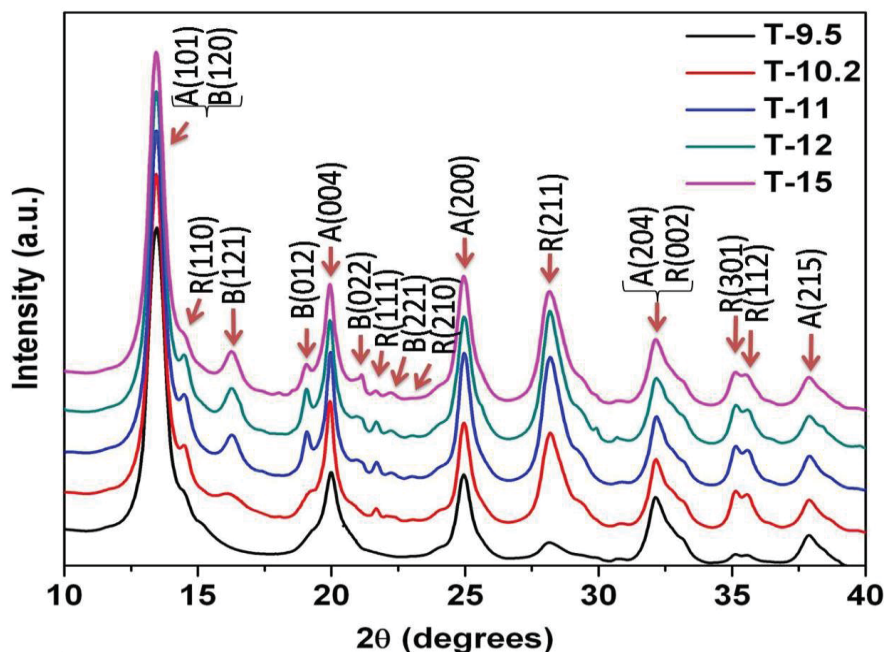


Figure 3.3 Synchrotron XRD of TiO₂ nanotubes synthesized at different voltages.

shown in the window depicted in Figure 3.2. The TiO₂ powders synthesized at 11 and 12 V have sharp peaks compared to powders synthesized at other voltages. This can be attributed to the good crystallinity of the tri-phase nanotubes resulted from stabilized synthesis voltage at which the equilibrium is reached between oxidation and chlorination. At higher voltages, the oxidation and chlorination rates are high, which constantly disturbs the phase growth mechanism resulting in non tubular morphology as reflected in T-15 (Figure 3.2). The low

intensity of the major peak of rutile R(110) in all the samples can be attributed to the preferred orientation of TiO₂ nanotubes.

Thus it can be concluded that the phase composition can be changed by simply tuning the DC voltage in RBA technique. The quantification of phases is difficult from the XRD pattern obtained from the laboratory X-ray diffractometer (Figure 3.1a) due to the poor resolution of rutile (110) peak. Therefore, high resolution synchrotron XRD analysis is carried out for the samples and compared in Figure 3.3.

The reflections from the corresponding planes of anatase, rutile and brookite phases are labeled in Figure 3.3 after matching the calculated interplanar spacing with that from the JCPDS files listed in Chapter 2. A clear resolution of the XRD peaks corresponding to reflections from R(110), R(111), B(221), R(210), R(301) and R(112) planes is observed,

Table 3.1 Quantification and crystallite size of individual phases in TiO₂ nanotubes synthesized at different voltages (The calculated error values are $\leq 2\%$)

Samples	Anatase		Rutile		Brookite	
	Phase %	Size (nm)	Phase %	Size (nm)	Phase %	Size (nm)
T-9.5	94	7.1	6	3.2	-	-
T-10.2	67	6.83	31	6.77	2	3.69
T-11	45	6.74	26	6.17	29	5.19
T-12	46	6.98	28	6.33	26	6.19
T-15	44	6.99	32	6.57	24	6.25

which is poor in case of laboratory XRD (Figure 3.2). The phase evolution with respect to synthesis potential can also be discerned from Figure 3.3. The individual phase composition

and grain size of the samples can be determined using the equations 2.2-2.5 and the results are listed in Table 3.1. It is clear that T-9.5 is majorly anatase with residual rutile (6%) and T-10.2 is majorly anatase-rutile with residual brookite (2%). The grain size of each phase, in an average, increases slightly with increase in synthesis voltage. The relatively smaller grain size of each phase in T-11 leads to the availability of large number of heterojunctions, hence effective charge transfer can be expected.

3.2.1.1.2 Raman spectra analysis

The phase structure of TiO₂ nanotubes synthesized at different voltages is further examined by Raman spectra analysis (Figure 3.4). The characteristic Raman modes of anatase

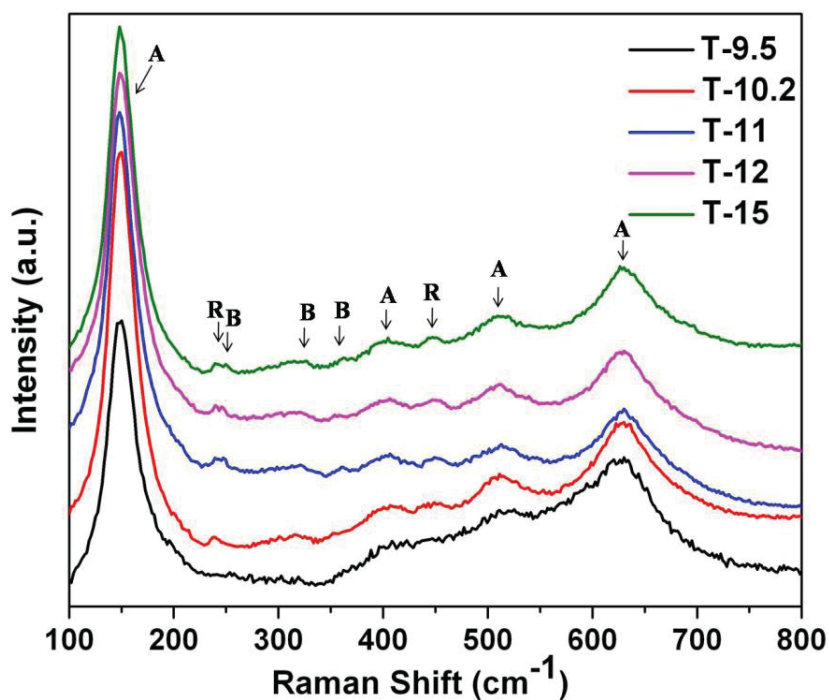


Figure 3.4 Raman spectra of TiO₂ photocatalysts synthesized at different voltages.

phase around 148, 402, 515, 630 cm⁻¹ are present in all the samples. These peaks are assigned to E_g , B_{1g} , A_{1g}/B_{1g} and E_g modes of anatase phase respectively¹⁰¹. The peak

corresponding to E_g mode of rutile appears around 448 cm^{-1} and is found in all the samples except T-9.5²²¹. A small peak around 240 cm^{-1} , as a result of second order scattering effect in rutile phase²²¹, also appears in all the samples except T-9.5. Similarly, the Raman shift corresponding to brookite phase which appears around $245, 322$ and 360 cm^{-1} representing its A_{1g}, B_{1g} and B_{2g} modes respectively⁵⁸ are clearly visible in T-11, T-12 and T-15. Thus Raman studies confirm the phase evolution from anatase to anatase-rutile to anatase-rutile-brookite with increase in synthesis potential.

3.2.1.2 Structural analysis

It is essential to know the morphology of the synthesized TiO_2 nanopowders as it plays a major role in determining the photocatalytic activity. Also it is necessary to obtain the information of the co-existence of different phases in the nanotube powders. Hence in order to understand the morphological and structural information, FESEM and TEM analysis are performed on these nanotubes and are presented in the following sections. The tubular morphology of the samples is confirmed from scanning electron micrographs given in Figure 3.5. The granular arrangement of particles in tubular orientation is observed in T-9.5 and an improved tubular morphology is observed in T-10.2 sample. This is due to the slow chlorination rate and the large oxide thickness. Where as in T-11 and T-12 samples, the nanotube bundles are clearly seen (Figure 3.5c and d). The diameters of the nanotubes in T-11 and T-12 samples are in the range of 30-120 nm. It is evident from Figure 3.5e that the tubular morphology of triphase TiO_2 is lost at higher synthesis potential.

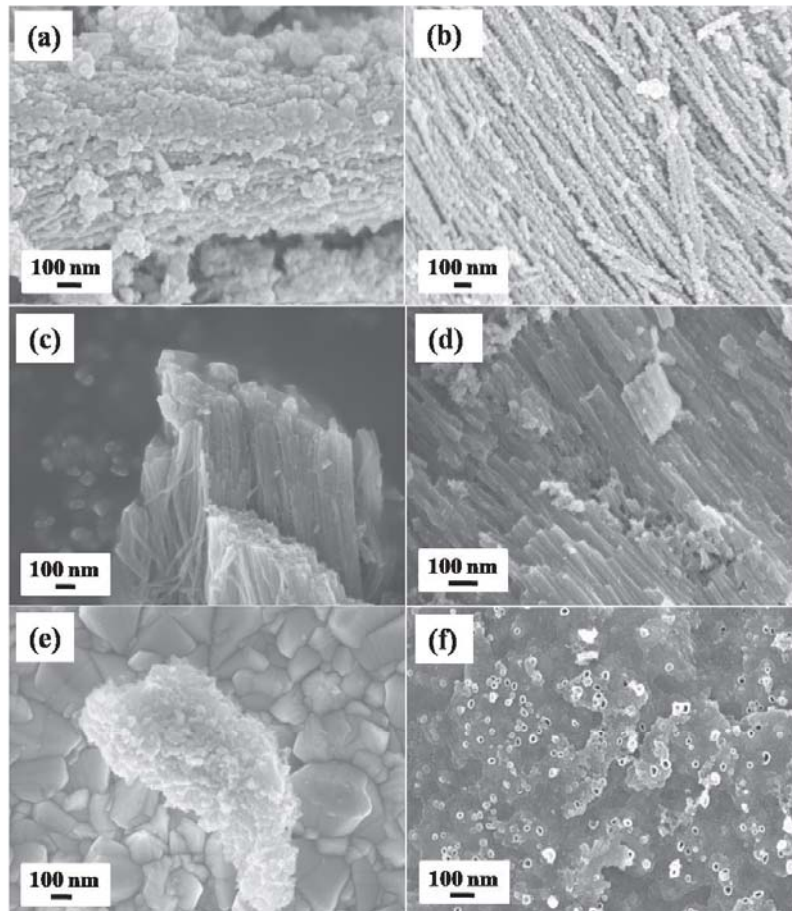


Figure 3.5 FESEM images of (a) T-9.5, (b) T-10.2, (c) T-11, (d) T-12, (e) T-15 and (f) the perpendicular view of T-11 nanotubes in which the tubular openings are visible.

TEM images of T-11 are presented in Figure 3.6. The bright field images of the nanotubes are shown in Figure 3.6a and b. The diameter of the nanotubes is in the range of 40-120 nm from SEM (Figure 3.5). High resolution TEM images of the nanotubes are presented in Figure 3.6c and d, with the Fast Fourier Transform (FFT) and Inverse Fast Fourier Transform

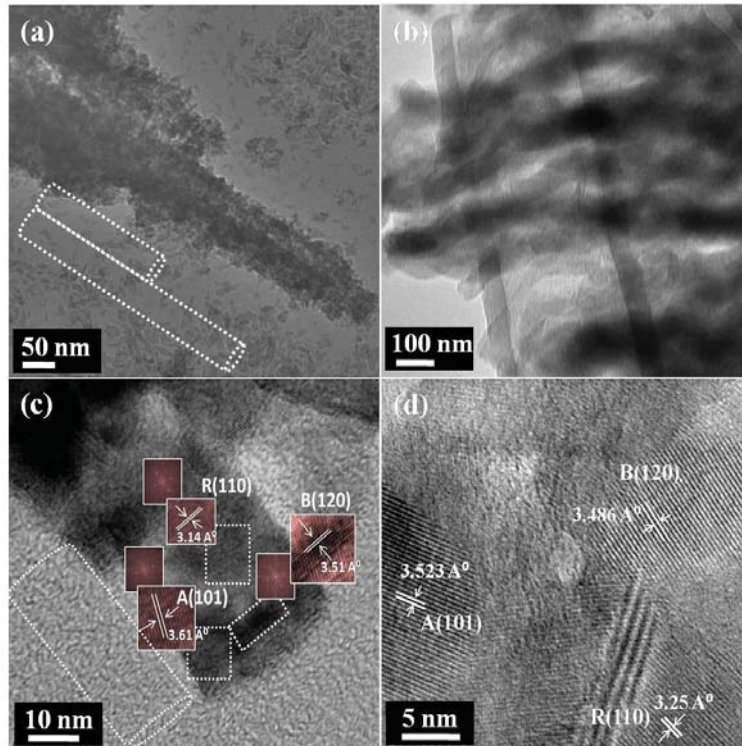


Figure 3.6 (a), (b) Bright field images of TiO₂ nanotubes; (c), (d) HRTEM images of T-11 (IFFT) images of the selected spots on the TiO₂ nanotube. The images clearly show the tubular structure of TiO₂ with the fringes corresponding to anatase (101), brookite (120) and rutile (110). Figure 3.6c confirms that all the three phases are present in a single nanotube. The junction observed between different phases of TiO₂ is an important feature which is expected to allow facile transfer of charge carriers. This would increase the dispersion of charge carriers and enhance the utilization of charge carriers for redox reactions. The results depict that TiO₂ nano-powders with best tubular morphology and optimum phase composition is obtained at 11 V.

3.2.1.3 Band gap analysis

The optical properties of the TiO₂ nanotubes synthesized at different voltages were analyzed using UV-visible DRS (Figure 3.7). The band gap values estimated from KM

function (Equation 2.7) corresponding to the DRS spectra of each sample is listed in Figure 3.7. Band gap energies for TiO₂ nanotubes synthesized at different voltages were found to be around 3.06 ± 0.04 eV. The obtained values are close to the reported values for anatase-rutile-brookite mixtures^{182,183}. Only a small difference is observed in band gap of samples as they are practically independent of different phases²²².

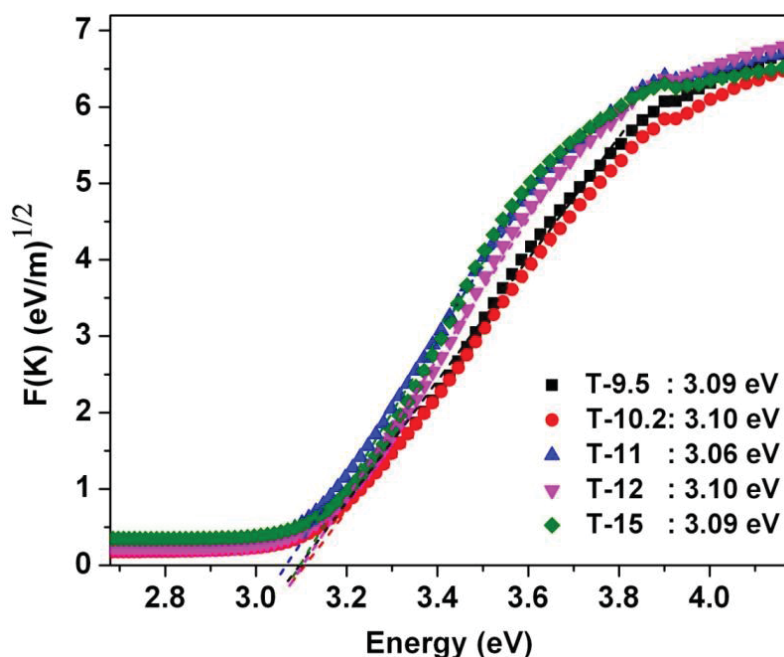


Figure 3.7 KM plot of TiO₂ nanotubes synthesized at different voltages

3.2.2 Effect of electrolyte concentration

It is discussed in previous section that variation in synthesis potential leads to changes in phase composition and TiO₂ nanopowders with best tubular morphology as well as optimum phase composition are obtained at 11 V. In order to study the effect of electrolyte concentration, the TiO₂ nanotubes are synthesized at different perchloric acid (electrolyte) concentration (0.07, 0.1, 0.12 and 0.15M of HClO₄), keeping the voltage constant at 11 V (± 0.03 V). The titania powders fallen into the electrolyte are collected,

centrifuged, washed in double distilled water and dried in air atmosphere at 70 °C overnight. The synthesized samples are labeled as T-0.07, T-0.1, T-0.12 and T-0.15 where the numbers represent the respective electrolyte concentration. More the chloride ions more will be the etching, and hence faster the reaction. It is noticed that the time to complete transformation of foil to powder is inversely proportional to the concentration of electrolyte.

3.2.2.1 Phase evolution

3.2.2.1.1 XRD analysis

The XRD patterns of TiO₂ nanotubes synthesized at different electrolyte concentrations are shown in Figure 3.8. It is observed that all the three phases are present in T-0.07 and T-0.1. As the perchloric acid concentration is increased from 0.07 to 0.15M, the intensity of rutile peaks gradually decreases and almost disappears in T-0.15. On the other hand, the brookite peaks grows in intensity with increase in electrolyte concentration. The rutile to brookite phase transformation (R(211) to B(113))with increase in electrolyte concentration, resulting ARB to AB phase composition is evident from Figure 3.8 (the windows depicted).

Phase quantification using Equations 2.2 - 2.5 and grain sizes of each phase obtained using Equation 2.6, are tabulated in Table 3.2. The phase compositions of different samples also indicate rutile to brookite phase transformation with increase in electrolyte concentration. Grain size of anatase is unaltered whereas that of rutile decreases and brookite increases. The energetics of phase polymorphs is sufficiently close that they could be reversed by small differences in surface energy.

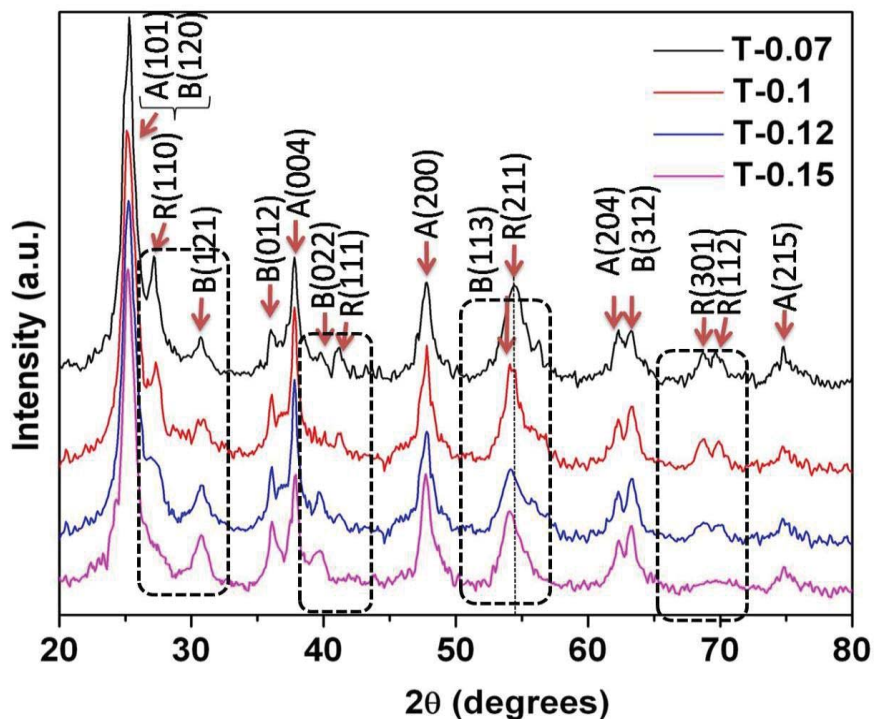


Figure 3.8 XRD of TiO₂ nanotubes synthesized at different electrolyte concentration

Table 3.2 Quantification and crystallite size of individual phases in TiO₂ nanotubes synthesized at different electrolyte concentration (The calculated error values are $\leq 2\%$)

Samples	Anatase		Rutile		Brookite	
	Phase %	Size (nm)	Phase %	Size (nm)	Phase %	Size (nm)
T-0.07	46	6.8	29	6.22	25	5.3
T-0.1	45	6.7	26	6.23	29	5.4
T-0.12	49	6.7	13	5.9	38	5.6
T-0.15	50	6.8	1	-	49	5.9

3.2.2.1.2 Raman analysis

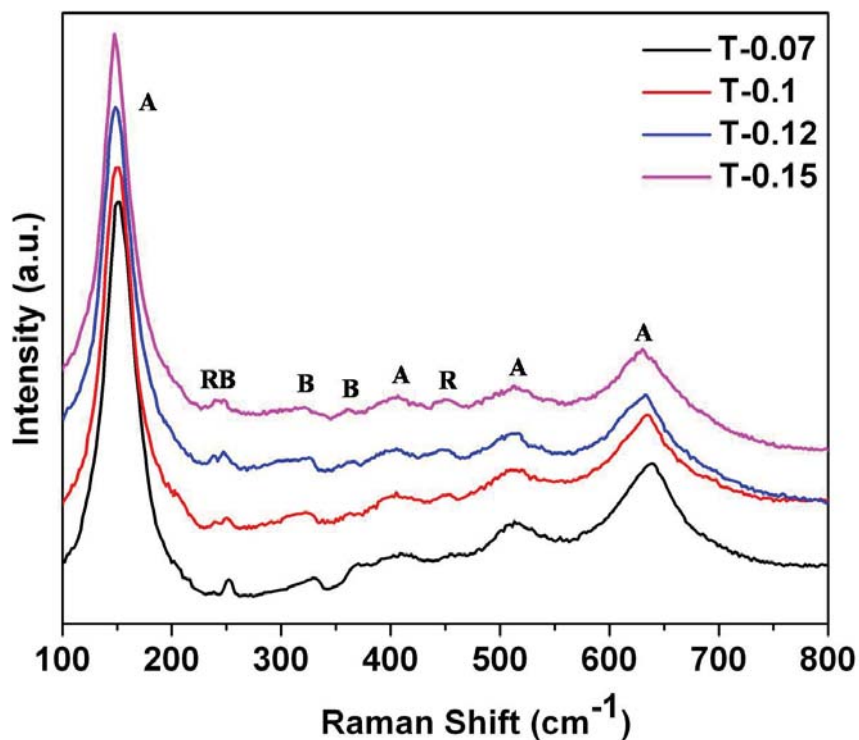


Figure 3.9 Raman spectra of TiO₂ photocatalysts synthesized at different electrolyte concentration

The phase structure of TiO₂ nanotubes synthesized at different electrolyte concentrations is further examined by Raman spectra analysis (Figure 3.9). The characteristic Raman modes around 148, 402, 515, 630 cm⁻¹ corresponding to E_g , B_{1g} , A_{1g}/B_{1g} and E_g modes respectively of anatase phase are present in all the samples¹⁰¹. Similarly the Raman shift corresponding to brookite phase which appears around 245, 322 and 360 cm⁻¹ representing its A_{1g} , B_{1g} and B_{2g} modes respectively⁵⁸ are clearly visible in all the spectra. The peak around 448 cm⁻¹ corresponding to E_g mode of rutile and that around 240 cm⁻¹, as a result of second order scattering effect in rutile phase²²¹, are present in T-0.07 and T-0.1. Whereas its intensity decreases in T-0.12 and it totally disappears in T-0.15. Thus it is clear that T-0.07 and T-0.1 possess all three phases whereas the rutile is diminishing in

T-0.12 and is absent in T-0.15. The Raman analysis again depicts that the increase in electrolyte concentration induces rutile to brookite phase transformation.

3.2.2.2 Structural analysis

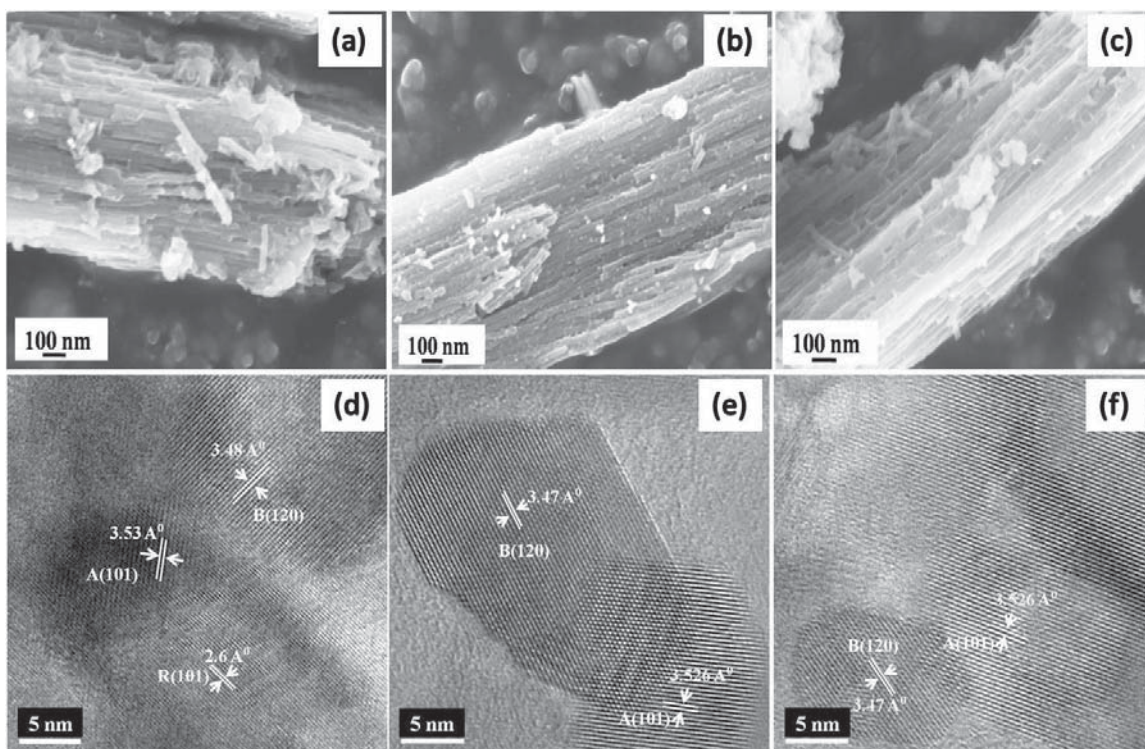


Figure 3.10 FESEM images of (a) T-0.07, (b) T-0.12 and (c) T-0.15; HRTEM images of (d) T-0.07, (e) T-0.12 and (f) T-0.15

FESEM analysis of selected TiO_2 samples is given in Figure 3.10 a-c. The tubular morphology is clearly evident in the FESEM images (Figure 3.10a - c) which represent the surface of T-0.7, T-1.2 and T-1.5. The tubular diameters are observed to be in the range of 30 to 120 nm for all the samples. It is very clear that change in electrolyte concentration doesn't affect the tubular morphology.

From HRTEM analysis of T-0.07 (Figure 3.10d), it is evident that the well resolved lattice features of three phases viz anatase, rutile and brookite exist in close proximity

making heterojunctions. Similar features are observed in the case of T-11 as seen already in Figure 3.6c and d. The interfaces among different phases lead to the efficient transfer of excited charge carriers from one phase to another thus enhancing its lifetime and thereby its photocatalytic efficiency. The interplanar spacing corresponding to rutile phase is not frequently observed in close proximity in HRTEM images of T-0.12 as shown in Figure 3.10e, whereas it is completely absent in the case of T-0.15 (Figure 3.10f). This further confirms that the TiO₂ nanotubes undergo phase transformation with increase in electrolyte concentration leading to ARB to AB composition, corroborating with results obtained from XRD and Raman spectra analysis.

3.2.2.3 Band gap analysis

The optical properties of the TiO₂ nanotubes synthesized at different electrolyte concentration were analyzed using UV-visible DRS (Figure 3.11). The band gap values estimated from KM function (Equation 2.7) corresponding to the DRS spectra of each sample is listed in Figure 3.11. It is noticed that the band gap values are independent of phase composition. All samples possess band gap which are in same range around 3.1 eV. Therefore it is clear that the change in electrolyte concentration doesn't affect the band gap instead only changes the phase composition.

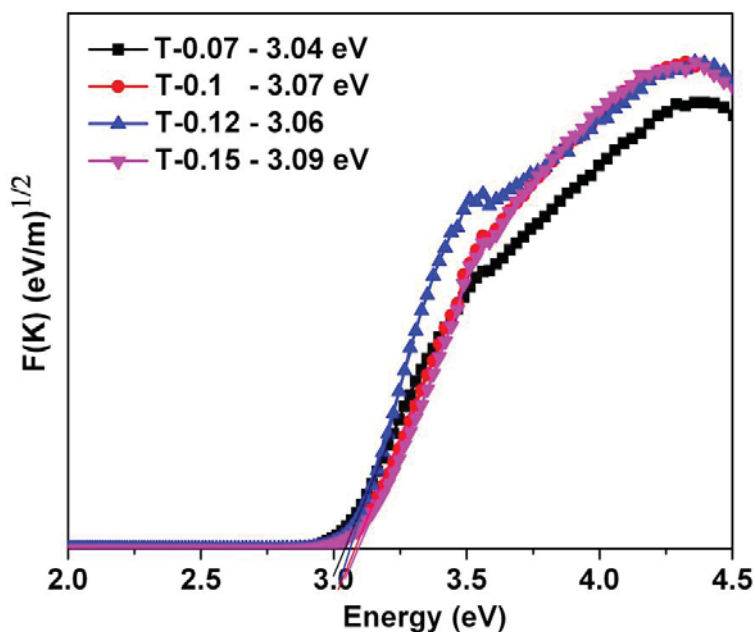


Figure 3.11 KM plots of TiO₂ nanotubes synthesized at different electrolyte concentration

3.3 Synthesis of Nitrogen Doped Triphase TiO₂ for Visible Light Activity

The synthesis of pristine triphase TiO₂ nanotubes are carried out by following RBA technique where the synthesis voltage is kept constant at 11 V (± 0.03 V), as it is seen earlier that it is the optimum voltage set up for obtaining triphase TiO₂ nanotubes. Nitrogen doped triphasic TiO₂ nanotubes, corresponding to different nitrogen concentrations are synthesized by having 0.5, 1.5, 3 and 4.5 wt% hydrazine hydrate as nitrogen source in 0.1 M HClO₄ electrolyte solutions with 11 V (± 0.03 V) as synthesis voltage. The pristine and doped TiO₂ powders fallen into the electrolyte are collected, centrifuged, washed in double distilled water and dried in air atmosphere at 70 °C overnight. The dried samples are labeled as, T-ARB for anatase-rutile-brookite TiO₂ nanotubes, whereas labels NT-0.5, NT-1.5, NT-3 and NT-4.5 represent nitrogen doped TiO₂ nanotubes synthesized with 0.5, 1.5, 3 and 4.5 wt% of nitrogen source respectively. The nitrogen concentration present in NT-0.5, NT-1.5, NT-3

and NT-4.5 are estimated to be 0.19, 0.29, 0.37 and 0.48 at % respectively from N 1s spectra of XPS which is demonstrated in later chapters.

3.3.1 Effect of N doping in triphase composition

3.3.1.1 XRD analysis

The XRD patterns of the pristine and N-doped catalysts are shown in Figure 3.12. It is observed that all the three phases are present in pristine T-ARB. The peak intensities corresponding to different phases obtained for samples synthesized at different concentrations of nitrogen precursor are found to be different. It is noticed that, as we increase the nitrogen source concentration from 0.5 wt to 4.5 wt %, the intensity of brookite peaks remain unaltered in NT-0.5 and NT-1.5 whereas it gradually decreases in NT-3 and finally disappears in NT-4.5. On the other hand, the anatase peaks grows in intensity with increase in nitrogen concentration. The brookite to anatase phase transformation with increase in nitrogen doping, resulting in ARB to AR transformation in N-TiO₂ nanotubes is evident from Figure 3.12 (depicted window).

Phase quantification and grain size, using Equations 2.2-2.5 are tabulated in Table 3.3. It is found that T-ARB is composed of 45% anatase, 26% rutile and 29% brookite phases. Marginal increase in grain size is noticed in case of rutile phase (almost in the same range), whereas reasonable increase of grain size in anatase phase with decrease in brookite grain size is noticed with increase in nitrogen concentration. The cause of brookite to anatase phase transformation can be attributed to the relation between phase stability and crystallite size viz. anatase is more stable at crystallite sizes below 11 nm, brookite at crystal sizes between 11 and 35 nm, and rutile with the crystal sizes ≥ 35 nm¹⁸⁷. The initial particle sizes of brookite and anatase in the pristine triphase TiO₂ nanotubes

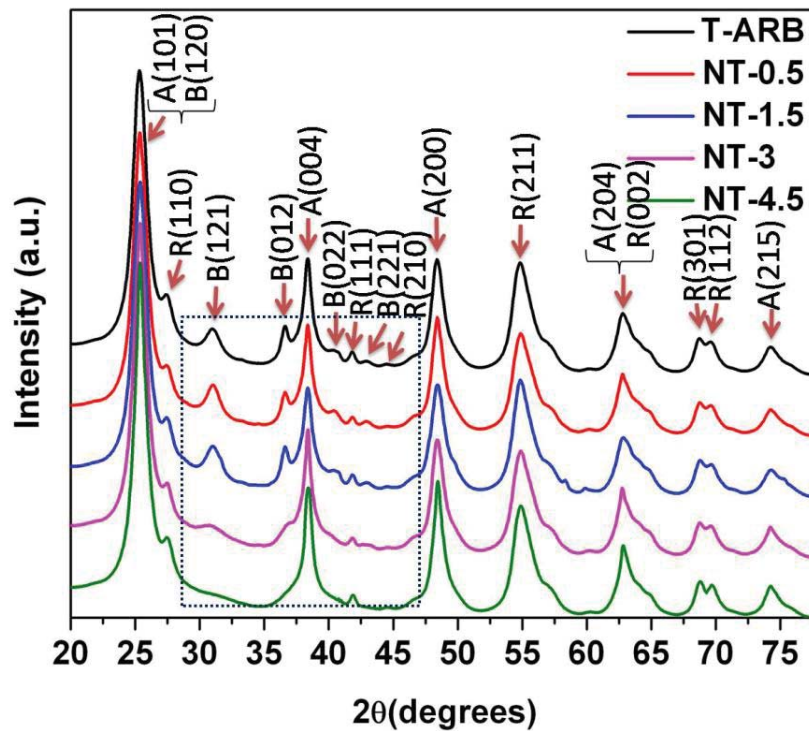


Figure 3.12 XRD of pristine and N-TiO₂ nanotubes

Table 3.3 Quantification and crystallite size of individual phases in TiO₂ and N-TiO₂ polymorphs (The calculated error values are $\leq 2\%$)

Samples	Concentration of Nitrogen (at %)	Anatase		Rutile		Brookite	
		Phase %	Size nm	Phase %	Size nm	Phase %	Size nm
T-ARB	-	45	6.7	26	6.23	29	5.19
NT-0.5	0.19	46	6.9	25	6.22	29	5.26
NT-1.5	0.29	54	7.2	26	6.191	20	5.03
NT-3	0.37	65	7.6	27	6.465	8	4.42
NT-4.5	0.48	72	8.06	28	6.68	-	-

are 6.7 and 5.1 nm, respectively. Upon nitrogen doping, particles of all the three phases coarsen. Due to this coarsening effect, the particle size of every phase increases initially.

However, as the nitrogen doping concentration increases, the smaller crystallite size of brookite (5.3 nm) than its stable crystallite size (11 – 35 nm) makes it unstable and is converted to anatase which is more stable phase at crystallite sizes between below 11 nm. Most nanocrystalline materials have metastable structure which gets converted to stable structure with change in temperature, pressure, grain growth, defects etc²²³⁻²²⁶. In case of TiO₂, anatase is stable at low temperature whereas rutile is stable at high temperatures²²³. Brookite, on the other hand is metastable when compared to rutile and anatase²²⁷. Therefore it is expected that brookite should transform either to anatase or rutile. Since the surface Gibbs free energy of anatase is lower than that of rutile phase^{228,229} when the particle size is small, brookite prefers to stabilize by transforming into anatase phase rather than into rutile phase. Pen and Banfield et al²³⁰ showed that the brookite phases can be considered as a polytype (reversible solid state transformation) of anatase, constructed out of essentially identical octahedral layers stacked in different ways. Therefore the inter conversion of anatase to brookite or brookite to anatase can be invoked by the displacement of Ti atoms into adjacent sites in the lattice. When the concentration of nitrogen doping into the lattice increases, the induced strain in the lattice causes displacement of lattice atoms. In addition, the oxygen vacancies generated by N-doping also leads to Ti displacement. These in turn invoke the unstable brookite to transform to stable anatase phase as it is the more stable phase in the size range of < 11 nm.

3.3.1.2 Raman spectra analysis

The phase compositions of pristine and N-TiO₂ nanotubes are further examined by Raman spectra analysis (Figure 3.13). The characteristic Raman modes of anatase phase appear at 148, 402, 515 and 630 cm⁻¹ for T-ARB and with slight shift in N-TiO₂

polymorphs. These peaks are assigned to E_g , B_{1g} , A_{1g}/B_{1g} and E_g modes of anatase phase respectively¹⁰¹. The peak corresponding to E_g mode of rutile appears around 448 cm^{-1} ²²¹ and a small peak around 240 cm^{-1} , as a result of second order scattering effect in rutile phase²²¹, also appears in all the samples with shift due to N-doping. Similarly, the Raman features corresponding to brookite phase around 245 , 322 and 360 cm^{-1} representing A_{1g} , B_{1g} and B_{2g} modes respectively⁵⁸ are visible in T-

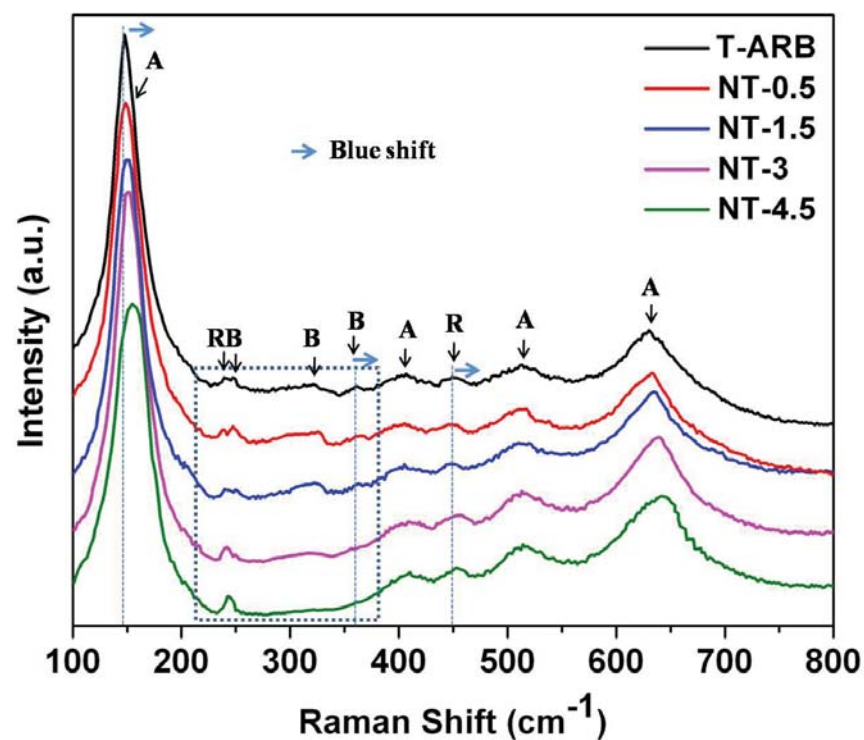


Figure 3.13 Raman Spectra of pristine and N-TiO₂ nanotubes

ARB and with slight shift in NT-0.5 and NT-1.5; whereas their intensities decreases in NT-3 and are absent in NT-4.5. Thus Raman studies further confirm the ARB to AR phase transformation with increase in nitrogen doping which is clearly depicted in the window of Figure 3.13. It is observed that the peaks corresponding to anatase, rutile and brookite modes are blue shifted (the shift is depicted in Figure 3.13) as a result of nitrogen doping. The shift

of the peaks can be attributed to change in size^{231,232}, lattice disorder or defects such as oxygen vacancies^{233,234}. The blue shift is also indicative of better electronic interaction between titania and nitrogen doping¹⁷.

3.3.2 Structural analysis

The surface morphology of pristine and nitrogen doped TiO₂ is analyzed using FESEM and TEM on selected samples. The tubular morphology is clearly visible in FESEM images (Figure 3.14a - c) which represent the surface of T-ARB, NT-1.5 and NT-4.5. The tube diameters are observed to be in the range of 30 to 120 nm for all the samples. Figure 3.14d shows the perpendicular view of the nanotubes present in NT-1.5 samples.

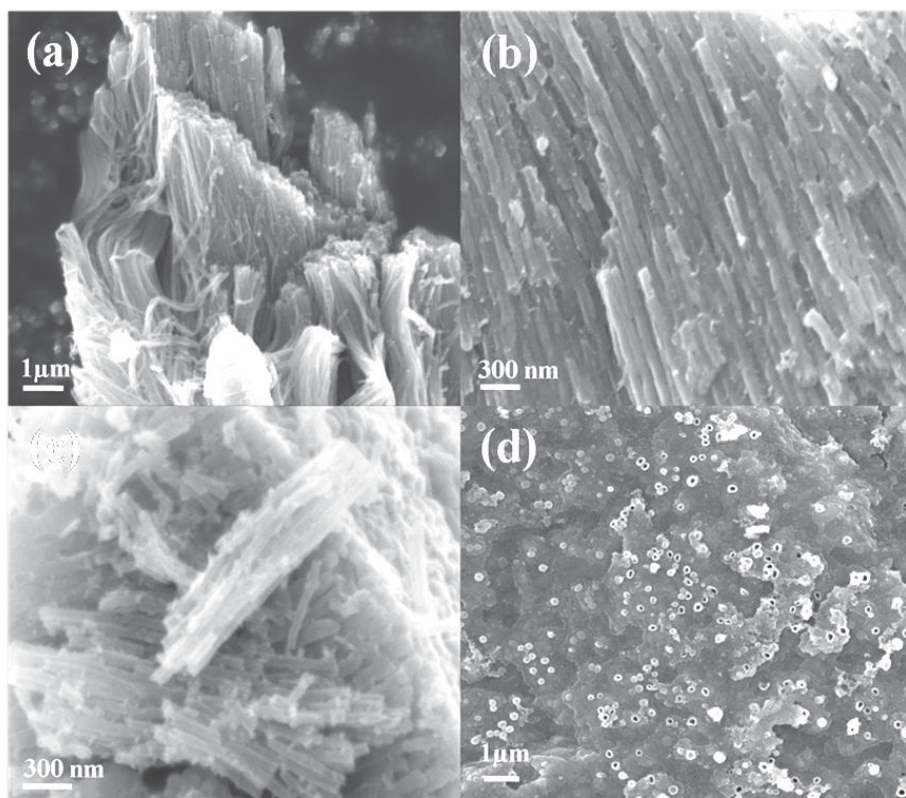


Figure 3.14 FESEM images of T-ARB and selected N-TiO₂ nanotubes.

The bright field image given in Figure 3.15a and b also confirms the tubular morphology of T-ARB and NT-1.5. From HRTEM analysis of single nanotube of T-ARB (Figure 3.15c), it is evident that the three phases viz anatase, rutile and brookite are present in a single nanotube. The triphase nature with well resolved lattice features is retained in NT-0.5, NT-1.5, and NT-3 as evident from the HRTEM analysis represented in Figure 3.15c and d.

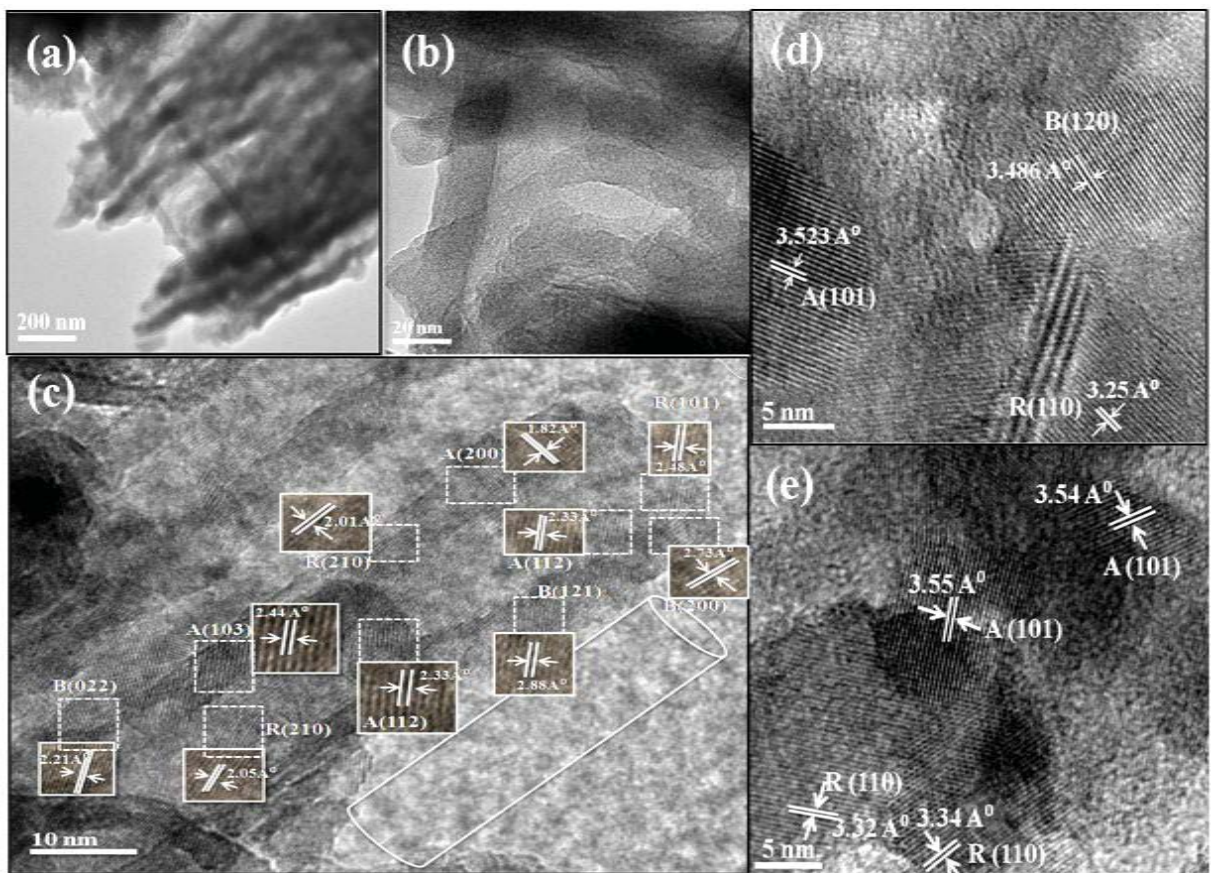


Figure 3.15 TEM bright field image: (a) T-ARB and (b) NT-1.5; HRTEM images: (c) T-ARB (d) NT-1.5 and (e) NT-4.5

The interplanar spacing corresponding to brookite phases is not frequently observed in close proximity in HRTEM images of NT-3, whereas it is completely absent in the case of NT-4.5

(Figure 3.15e). This further confirms that the TiO₂ nanotubes undergoes phase transformation from ARB to AR composition with increase in nitrogen doping, which corroborate with results obtained from XRD and Raman spectra analysis. An important observation is the hetero-junctions formed between various phases of titania in the nanotubes. This demonstrates the physical connectivity between three phases at nanoscopic levels, and the junctions are expected to act as charge separation centers.

3.3.3 Band gap analysis

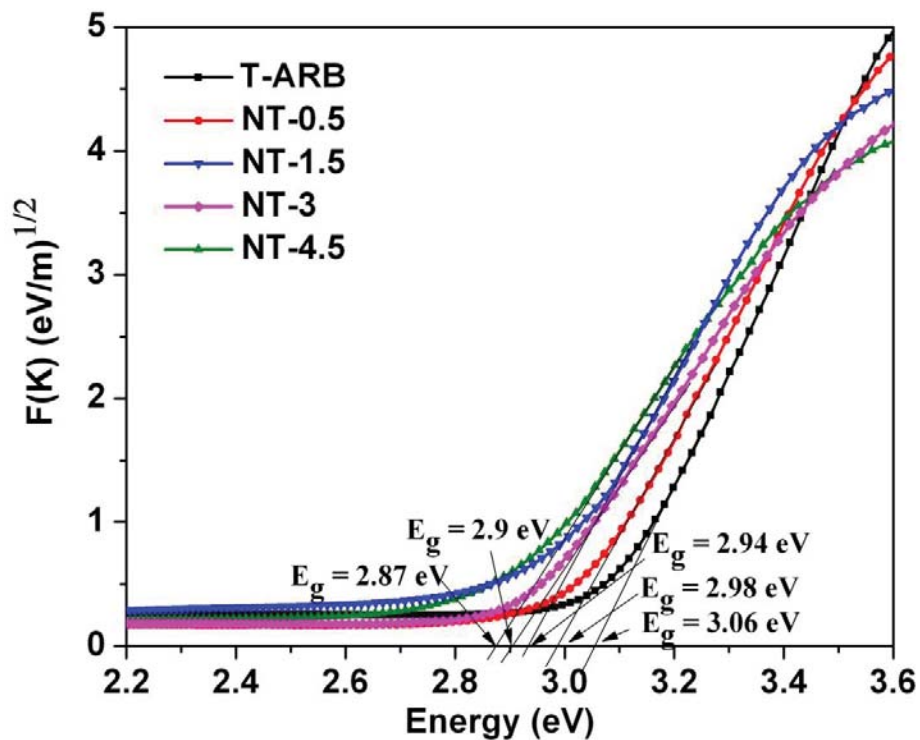


Figure 3.16 KM plots of T-ARB and N-TiO₂ nanotubes

The optical properties of the pristine and N-doped TiO₂ nanotubes were analyzed using UV-visible DRS (Figure 3.16). The band gap values estimated from KM function (Equation 2.7) corresponding to the DRS spectra of each sample is mentioned in Figure 3.16. Band gap of

pristine TiO₂ nanotubes (T-ARB) is found to be around 3.06 eV. The degree of nitrogen doping strongly affects the visible light absorption of TiO₂ leading to monotonic decrease in band gap with increasing nitrogen doping. The lowest band gap of 2.87 eV is achieved in NT-4.5 which has highest nitrogen doping.

3.4 Synthesis of Hydrogenated TiO₂ for Visible Light Activity

3.4.1 Effect of hydrogenation in phase composition

3.4.1.1 XRD analysis

The phase composition of the pristine TiO₂ nanotubes (T-ARB) and TiO₂ nanotubes annealed in hydrogen atmosphere at 250 and 450 °C (H-250 and H-450) is analyzed by XRD (Figure 3.17). From Figure 3.17 it is clearly seen that all three phases such as anatase, rutile and brookite are present in all the samples. The crystallinity of the TiO₂ powder is improved after hydrogen annealing which is evident from the sharp increase in the peak intensities of H-250 and H-450. The crystallite size of the individual phase in all the samples are determined using Scherrer equation (Equation 2.2) from characteristic XRD peaks of anatase A(101), rutile R(110) and brookite B(121). The calculated values are represented in Table 3.4. It is found that the crystallite size of all phases increases with hydrogen annealing temperature. Similar changes in XRD pattern are observed in T-ARB annealed in air atmosphere for 2 hours at 250 and 450 °C. The individual grain size and phase composition of pristine and hydrogenated triphase sample determined using Equations 2.3-2.5 is also tabulated in Table 3.4. It is found that the T-ARB is composed of 49% anatase, 27% rutile and 24% brookite phases. The phase percentage of rutile is increased at the expense of

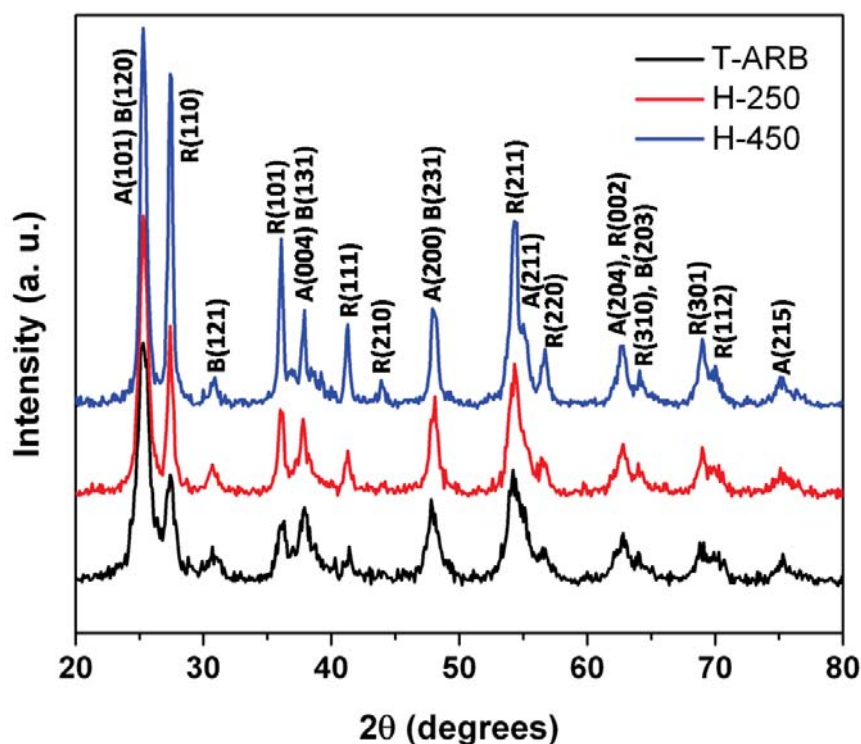


Figure 3.17 XRD of pristine and hydrogenated TiO₂ nanotubes

Table 3.4 Quantification and crystallite size of individual phases in pristine and hydrogenated TiO₂ nanotubes (The calculated error values are $\leq 2\%$)

Samples	Anatase		Rutile		Brookite	
	Phase %	Size nm	Phase %	Size nm	Phase %	Size nm
T-ARB	49	7.021	27	10.0637	24	6.5246
H-250	42	12.106	33	16.838	25	9.8637
H-450	24	18.806	48	22.1218	28	10.454

anatase in the hydrogen annealed samples as well as at higher annealing temperatures; whereas brookite shows a marginal increase in content after H₂ reduction at 450 °C. The presence of brookite phase enhances the anatase-rutile transformation as the interface

between brookite and anatase with high interfacial energy would provide potential nucleation sites for anatase-rutile transition as suggested by Gribb and Banfield^{235,236}. The brookite phase forms as the byproduct in anatase-rutile phase transition and hence it increases marginally with respect to hydrogen annealing temperatures²³⁷.

3.4.1.2 Raman analysis

The phase composition of the samples and the effect of hydrogen annealing are further explored by Raman spectroscopy. The Raman spectra of the samples are illustrated in Figure 3.18 with corresponding labels. The well resolved distinct Raman peaks corresponding to anatase, rutile and brookite phases are present in all the polymorphs. In T-ARB polymorph, the peaks at 148, 401 and 509 cm^{-1} corresponds to E_g , B_{1g} and A_{1g} (or B_{1g}) modes of anatase phase,^{238,239} the peaks at 440 and 610 cm^{-1} corresponds to E_g and A_{1g} modes of rutile phase²³⁹ whereas the peaks at 240, 318 and 626 cm^{-1} corresponds to A_{1g} , B_{1g} and A_{1g} modes of brookite²⁴⁰ respectively. The spectra of H-250 and H-450 retain the peaks as that of T-ARB as the Raman modes are preserved during hydrogenation. It is observed that the peaks corresponding to different vibration modes of rutile and brookite are blue shifted whereas that of anatase phase is red shifted (the shift is depicted in Figure 3.18) as a result of hydrogen annealing of ARB polymorph. The shift of the peaks may be due to some of the following reasons such as change in grain size^{231,232}, lattice disorder due to hydrogenation or defects such as oxygen vacancies^{233,234}. In our case the size of crystallites obtained from XRD data (>10 nm) exclude the occurrence of finite size effects. Consequently the presence of defects is rather responsible for the blue shift of rutile and brookite peaks. The red shift in anatase E_g mode at 148 cm^{-1} in hydrogen annealed TiO_2 samples hints that the anatase is being transformed to rutile as the rutile B_{1g} appears around

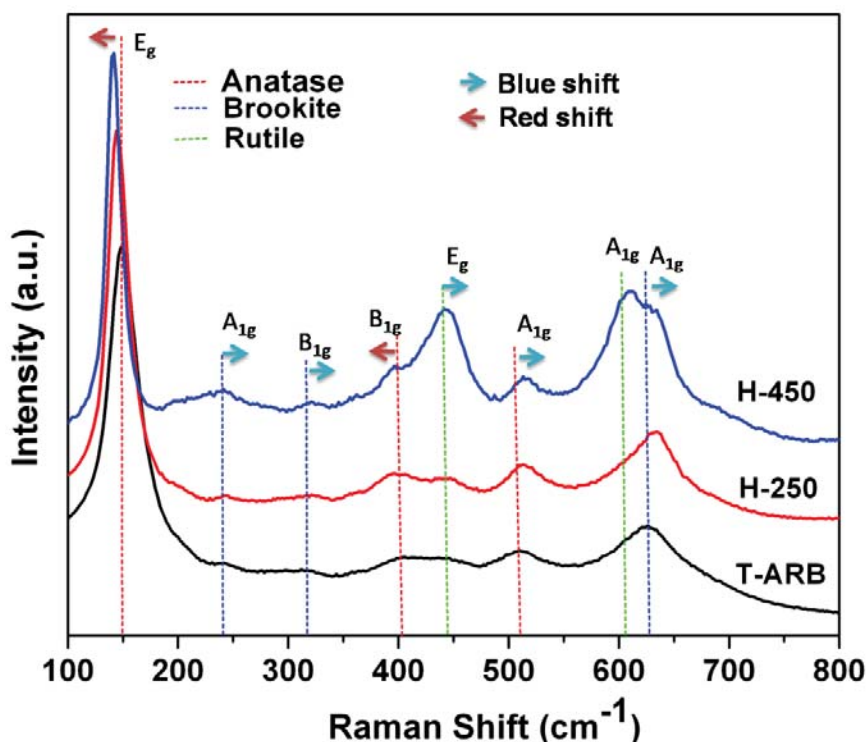


Figure 3.18 Raman Spectra of TiO₂ and hydrogenated TiO₂ nanotubes

143 cm⁻¹ and it is difficult to distinguish²⁴¹. The red shift in anatase B_{1g} peak around 401 cm⁻¹ may be due to the stress induced in the nanotubes with growing size of other phases²⁴². Thus the Raman spectrum of hydrogen annealed samples clearly confirms the presence of three phases in reduced TiO₂ samples.

3.4.2 Structural analysis

The surface morphology of pristine and hydrogenated TiO₂ is analyzed using SEM and TEM images on selected samples. The tubular morphology is clearly visible in SEM images (Figure 3.19a and b) which represent the surface of T-ARB and H-450 samples. The tube diameters are in the range of 30 to 120 nm in both the samples. The bright field image of T-ARB given in Figure 3.19c also confirms the sample's tubular morphology. From HRTEM analysis of single nanotube of T-ARB (Figure 3.19d), it is evident that the three

phases viz anatase, rutile and brookite are present in single nanotube. The triphase nature with well resolved lattice features is retained in H-250 and H-450 as evident from the HRTEM analysis represented in Figure 3.19e and f. The disorder layer at the lattice surface resulting out of hydrogenation^{213,238} is not observed in this case as the samples are marginally hydrogenated. The SAED pattern in Figure 3.19 g and h further proves that the H-450 is highly crystalline compared to T-ARB thus leading to the conclusion that the hydrogenation doesn't induce disorder on the surface of TiO₂ nanotubes.

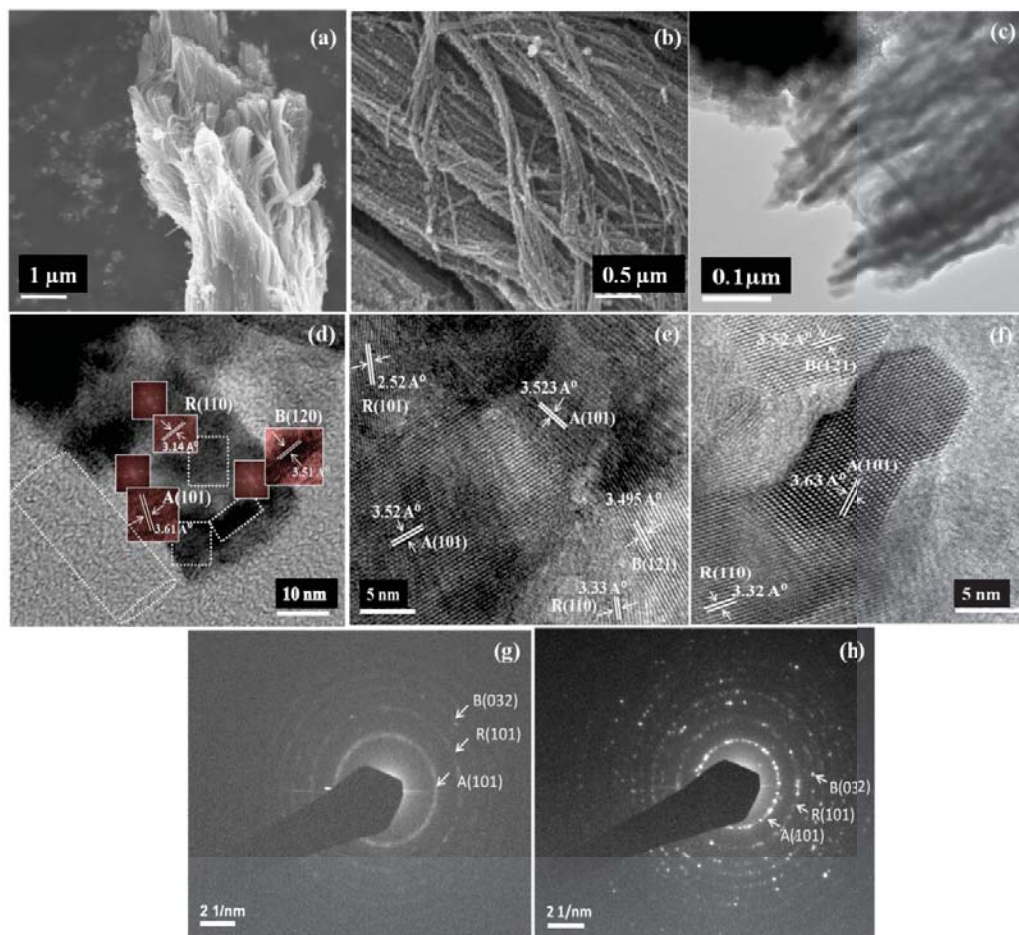


Figure 3.19 FESEM images of (a) T-ARB and (b) H-450; (c) TEM bright field image of T-ARB, (d) HRTEM of single nanotube of T-ARB; HRTEM images of (e) H-250 and (f) H-450; SAED patterns of (g) T-ARB and (h) H-450

3.4.3 Band gap analysis

Optical properties of the prepared samples were characterized using UV-Vis absorbance and DRS (Figure 3.20). In our case, there is no enhancement after 520 nm in the absorbance spectra of hydrogenated polymorphs, the region where the spectral improvement leads to the typical color change of hydrogenated samples as reported in many literatures.^{146,217} In fact the TiO₂ powder maintained the original colorless nature even after hydrogenating at 250 °C and 450 °C for 2 hours. However there is a minor shift in the spectra towards visible region and the spectral intensity is enhanced in the region from 412 to 518 nm¹⁴⁶ with respect to hydrogen annealing temperature. Therefore H-250 and H-450 samples may be considered as marginally hydrogenated.

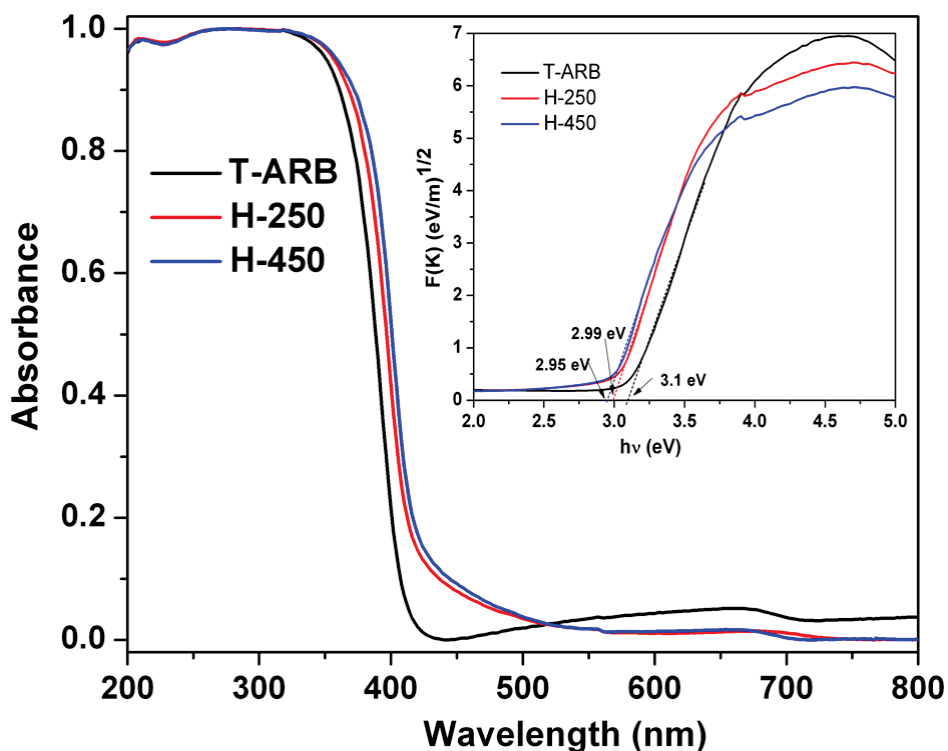


Figure 3.20 UV-Vis absorbance spectra of TiO₂ and hydrogenated TiO₂ nanotubes (Inset: Band gap values calculated from the KM plots)

The synthesis of black color titania requires either high pressure hydrogenation or high temperature hydrogenation²⁴³⁻²⁴⁵ as reported in literatures. In the present case of triphase TiO₂ nanotube powders, the black titania is not obtained with the present hydrogenation conditions and even with prolonged annealing time (7 hours at temperatures 250 and 450 °C). In order to maintain three phase crystalline structure and nanotubular morphology, the high pressure or high temperature hydrogenation treatments are not carried out. Also, it is reported that the slight hydrogenation exhibit enhanced photocatalytic activity compared to the black titania produced after heavy hydrogenation¹⁴⁶. Thus the TiO₂ hydrogenated at 250 and 450 °C for 2 hours are used for photocatalytic treatments. However it is noticed later (vide infra, Figure 6.1) that these slightly hydrogenated samples are much better in performance in hydrogen generation compared to pristine TiO₂.

KM analysis of the corresponding diffuse reflectance spectra is represented as the inset of Figure 3.20. Band gap energies (calculated using Equation 2.7) of T-ARB, H-250 and H-450 are found to be 3.1, 2.99 and 2.95 eV respectively. The theoretical band gap of nanocomposite materials could be accurately determined using the XRD data (ie mass fraction of each polymorph) and band gap energies of individual polymorphs (anatase, rutile, brookite) using Equation 2.6. Theoretically determined band gap energies of T-ARB, H-250 and H-450 are equal to 3.11, 3.09 and 3.08 eV. Among the values, only the theoretical band gap of T-ARB matches with the experimental value. This confirms that the band gap of H-250 and H-450 samples have been modified only due to the hydrogen annealing rather than the change in crystallinity due to heating effect as observed from XRD. The decrease in the band gap values of hydrogenated samples may be due to the formation of inter band gap states.¹⁴⁶

3.5 Summary

Triphasic TiO₂ nanotubes are successfully synthesized using RBA technique. The increase in synthesis potential induces the phase evolution from anatase to anatase-rutile to anatase-rutile-brookite in TiO₂ nanotubes. Similarly, the increase in electrolyte concentration induces anatase-rutile-brookite to anatase-brookite phase composition in synthesized nanotubes due to rutile to brookite phase transformation. All the synthesized TiO₂ samples have tubular morphology with the tube diameters from 30-120 nm. Also, it is found in triphase TiO₂ that all the three phases exist in single nanotube leading to more heterojunctions. This demonstrates the physical connectivity between three phases at nanoscopic levels, and the junctions are expected to act as charge separation centers. Similarly, the same is found for the case of biphasic TiO₂ nanotubes (anatase-brookite) obtained with increase in electrolyte concentration. In addition, the band gap analysis of all the TiO₂ nanotubes reveals that their band gap is independent of phase composition in TiO₂ nanotubes.

Nitrogen doping in triphase TiO₂ is successfully obtained using RBA technique using suitable nitrogen precursor. It is found that the nitrogen doped into the TiO₂ lattice induces brookite to rutile phase transition at higher nitrogen concentrations. All the phases exist in single nanotube again indicating the potential of enhanced photoexcited charge transfer among the different phases in N-TiO₂. The band gap is decreased with increase in nitrogen doping, thereby extending the visible light absorption. This indicates the formation of defects states (N 2p) into the band gap of doped TiO₂. Hence it is expected that these N-TiO₂ polymorphs are expected to possess better photocatalytic efficiency due to the absorption of increased quanta of light.

On the other hand, hydrogen annealed TiO₂ doesn't alter the number of phases present in the sample as obtained in our previous modifications of triphase TiO₂, rather it changes only the crystallinity and triphase composition. The hydrogenation of triphase TiO₂ nanotubes doesn't induce disorder on the surface of TiO₂ nanotubes. All the three phases are present in single nanotubes similar to the results of above cases. Like N-doped triphase TiO₂, hydrogenation also decreases the band gap thus allowing absorption of more light quanta. This may be due to the generation of defect states into the band gap of triphase TiO₂. Hence it is expected that hydrogenated TiO₂ can act as an efficient visible light photocatalyst for hydrogen generation due to the presence of high crystalline triphase TiO₂ nanotubes with extended visible light absorption.

Photocatalytic Hydrogen Generation Efficiency of Triphase Heterojunctions and Their Band Alignment

In the previous chapter, the synthesis of triphase TiO₂ nanotubes using RBA technique is discussed. In addition, the sensitivity of the synthesis of triphase TiO₂ nanotubes with respect to variation in experimental conditions is also demonstrated. The present chapter illustrates the photocatalytic hydrogen generation efficiency of the synthesized triphase TiO₂ nanotubes in comparison with biphasic and single phase TiO₂ nanotubes obtained in RBA technique under different experimental conditions. In addition, the band alignment and charge transfer pathway in triphase TiO₂ nanotubes is derived from the deconvolution of PL and UPS spectra.

4.1 Introduction

Unlike the widely studied anatase or anatase/rutile systems, the reports on water splitting efficiency of ARB triphase TiO_2 nanostructures is unavailable to the best of author's knowledge. To understand the actual reactivity of triphase TiO_2 nanostructures in photocatalytic water splitting, a facile synthesis of TiO_2 nanoparticles having three phases in single entity whose phase compositions are not separated by dispersion as well as a clear cut picture of the charge transfer mechanism in the triphase system is highly appreciable. In order to study the efficiency of triphase TiO_2 in comparison to its biphasic and single phase form, the single, two and three phase compositions should be obtained from the same system. It is already demonstrated in the previous chapter that the triphase TiO_2 nanotubes are synthesized successfully by simple cost effective RBA technique. It is also found that using the same technique, the biphasic and single phase TiO_2 nanotubes are obtained by varying experimental conditions.

Therefore, the hydrogen generation efficiencies of all the synthesized TiO_2 nanotubes with varying phase composition can be compared easily to understand the reactivity of triphase TiO_2 nanotubes. In addition, unlike anatase-rutile biphasic system, studies on photoexcited electron transfer pathway in ARB triphase system has not yet come to the spotlight to determine the underlying physics behind the high efficiency of such systems. Therefore the present chapter deals with the hydrogen generation efficiency of the synthesized TiO_2 nanotubes corresponding to various phase compositions under one sun condition to compare the efficiency of single, biphasic and triphase TiO_2 nanotubes. For the first time, a band diagram is proposed for ARB system with the possible electron transfer pathway.

4.2 Photocatalytic Hydrogen Generation

4.2.1 TiO₂ nanotubes synthesized at different voltages

The photocatalytic hydrogen generation experiments using all the samples are carried out in water, containing ethanol as a sacrificing agent. The H₂ evolution rate of TiO₂ nanotubes at different time intervals are depicted in Figure 4.1. The highest hydrogen evolution of 645 $\mu\text{mol/g}$ is observed for T-11, after 4 hours of light irradiation. The hydrogen generation efficiency of the samples follow the order T-9.5(A: 94%, R: 6%) < T-10.2 (A:67%, R:31%, B: 2%) < T-15(A: 44%, R: 32%, B: 24%) < T-12 (A:46%, R :28%, B: 26%) < T-11(A: 45%, R: 26%, B: 29%).

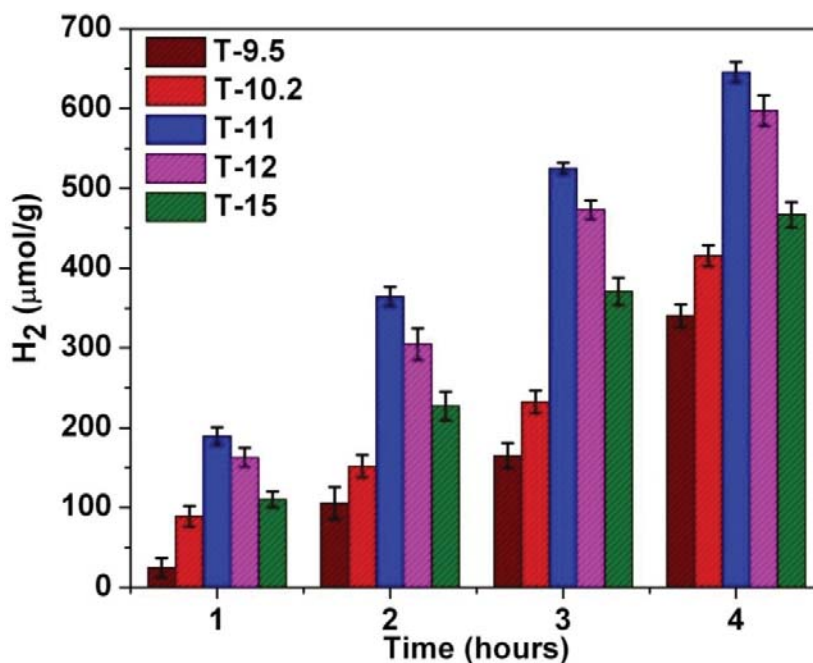


Figure 4.1 Cumulative hydrogen generation of triphasic TiO₂ synthesized at different voltages under one sun conditions with ethanol as sacrificial agent (The error bars in the figure are standard error values of three tests). The area of illumination is 12 cm².

The low hydrogen evolution of T-9.5 compared to that of T-10.2 can be attributed to the presence of single phase in T-9.5 and two phases in T-10.2 which lead to the efficient electron transport along anatase-rutile (AR) interface. Compared to T-10.2, the hydrogen generation is more in T-11, T-12 and T-15 samples. This is due to the presence of anatase, rutile and brookite phases in the nanotubes of T-11, T-12 and T-15, which enhances the charge separation by the facile movement of charge carriers across the heterojunction interfaces. Among the triphase samples, T-11 has the highest hydrogen generation efficiency. This can be attributed to the better crystallinity of the phases in the nanotubes which enhances charge transport thereby facilitating charge separation leading to effective hydrogen generation¹⁶⁰. Despite the fact that T-12 possesses similar characteristics as T-11, the noticeable difference in hydrogen generation efficiency is due to the presence of defects which is discussed later with respect to Figure 4.4a and b. The low reactivity of T-15 can be attributed to the destruction of tubular morphology (Figure 3.5e) leading to reduction in active surface area. H₂ generated by T-11 (ARB) is twice that of T-9.5 (anatase) TiO₂ nanotubes and 1.6 times that of T-10.2 (AR) TiO₂ nanotubes.

The solar to hydrogen conversion efficiency (Equation 2.15) of 10 mg photocatalyst of all the TiO₂ samples synthesized with change in synthesis potential is calculated to be around 0.01 %.

4.2.2 TiO₂ nanotubes synthesized at different electrolyte concentrations

The hydrogen generated by TiO₂ nanotubes synthesized under different electrolyte concentrations is represented in Figure 4.2. The sample T-0.07 (A:46%, R:29%, B: 25%) produces more hydrogen (655 μmol/g for four hours of solar irradiation) compared to other

sets at each hour of light irradiation. Similarly, the hydrogen generated by T-0.1 (A:45%, R:26%, B: 29%) is almost equal to that of T-0.07. As the electrolyte concentration is increased as in the case of T-0.12 (A:49%, R:13%, B: 38%) and T-0.15 (A:50%, R:1%, B: 49%), the hydrogen generation values drops to 582 and 538 $\mu\text{mol/g}$. The surface morphology and band gap analysis given in Chapter 3 clearly indicates that there is no phenomenal difference in the samples synthesized using different electrolyte concentration. Only difference among these samples is its

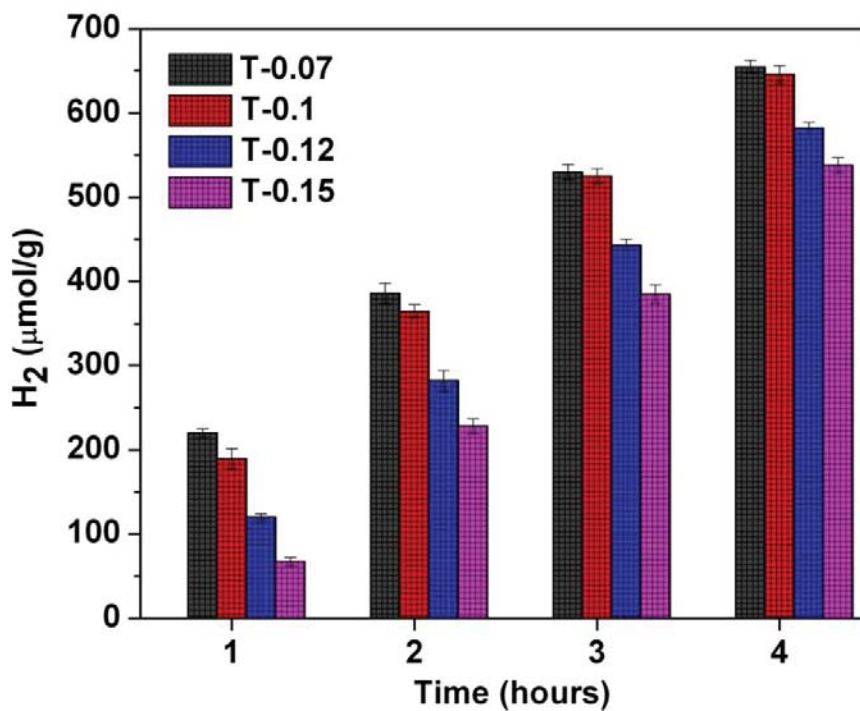


Figure 4.2 Cumulative hydrogen generation of triphasic TiO_2 synthesized at different electrolyte concentration under one sun conditions with ethanol as sacrificial agent (The error bars in the figure are standard error values of three tests). The area of illumination is 12 cm^2 .

phase composition which is clear from XRD and Raman spectra (Figures 3.8 and 3.9). Hence, the hydrogen generation results indicate that the high hydrogen generation efficiencies of T-0.07 and T-0.1 are due to their triphase composition. The decrement in hydrogen generation ability of T-0.12 can be ascribed to the low content of rutile phase. The relatively low water splitting ability of T-0.15 can be attributed to its biphasic nature. The hydrogen generated by high efficient sample T-0.07 (ARB) is 1.25 times that of T-0.15 (AB).

The solar to hydrogen conversion efficiency (Equation 2.15) of 10 mg photocatalyst of all the TiO_2 samples synthesized with change in electrolyte concentration is also calculated to be around 0.01 %.

4.3 Charge Separation Efficiency

4.3.1 TiO_2 nanotubes synthesized at different voltages

4.3.1.1 Mott-Schottky analysis

To ascertain the improvement in charge separation due to band alignment in triphase system compared to biphasic and single phase systems, MS analysis is performed under UV light for T-9.5, T-10.2, T-11 and T-12 samples in 0.5 M Na_2SO_4 electrolyte. Figure 4.3 represents the MS plots, from which the E_{fb} is calculated using the MS relation as expressed in Equation 2.14¹⁶ and the calculated E_{fb} values are given in Figure 4.3. All samples exhibit a positive slope in MS plots, as expected for n-type semiconductors. The observed cathodic shift in E_{fb} is in the order T-11 > T-12 > T-10.2 > T-9.5. When TiO_2 is irradiated, the upward shift of the Fermi level (FL) enhances the charge separation at the semiconductor/electrolyte interface. The electrons in CB and holes in VB take part in the

redox reaction^{218,246}. In a multi-phase system, under UV illumination, the excited charge carriers transfer from one phase to another leading to a higher shift in the FL towards the CB edge (as in the case of triphase (T-11 and T-12) and biphas (T-10.2)). This causes higher degree of band bending and hence higher E_{fb} . The degree of FL shift depends on the number of phase junctions present. The difference in E_{fb} among the different samples (T-11 > T-12 > T-10.2 > T-9.5) supports that more the phase junction more the flat band potential (E_{fb}) and hence better charge separation.

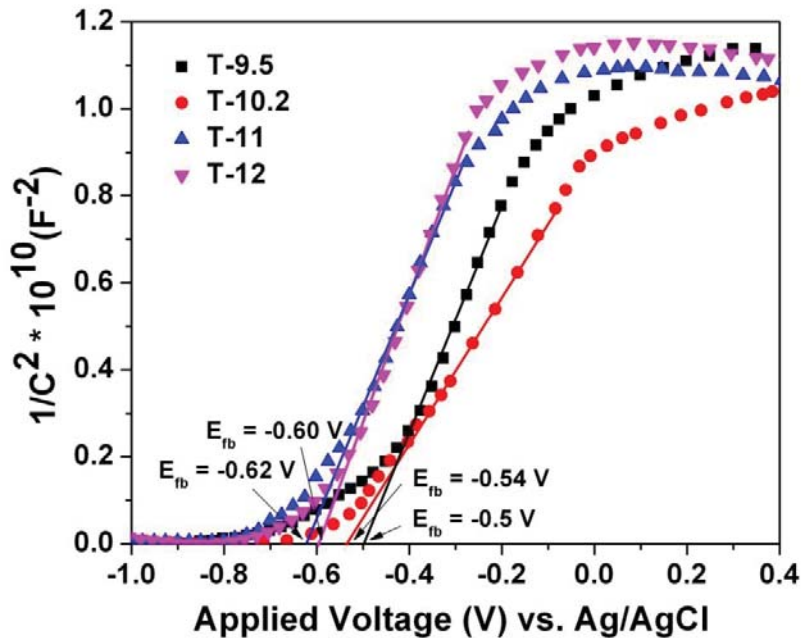


Figure 4.3 MS plots of TiO₂ nanotubes synthesized at different voltages in 0.5M Na₂SO₄ at a frequency of 1 KHz, under UV illumination.

From Table 3.1, it is clear that T-11 and T-12 shows comparable phase percentages. However, crystallite size analysis (Table 3.1) indicates a marginally smaller crystallite size of anatase and rutile, and significantly smaller size of brookite in T-11 compared to T-12. This difference in crystallite size would lead to more number of heterojunctions and is

expected to assist in effective charge separation. This reflects in the MS plots presented above (E_{fb} of T-11 > T-12). Further, the presence of all three phases in close proximity in T-11, as observed in the HRTEM analysis (Figure 3.6c and d), directly supports the presence of bulk heterojunctions.

4.3.1.2 Photoluminescence

The PL spectra (Figure 4.4 a) is analyzed to study the photophysics of the photogenerated charge carriers in the samples. In Figure 4.4a, the high PL intensity is observed for T-9.5, T-10.2 and T-15 whereas the intensity is comparatively low for T-11 and T-12 samples. In general the PL intensity in the region from 1.75 eV to 2.65 eV is due to the defects present in the sample, which act as electron traps. The peak around 2.11 eV is due to the oxygen vacancy related defects in addition to the under-coordinated Ti acting as electron

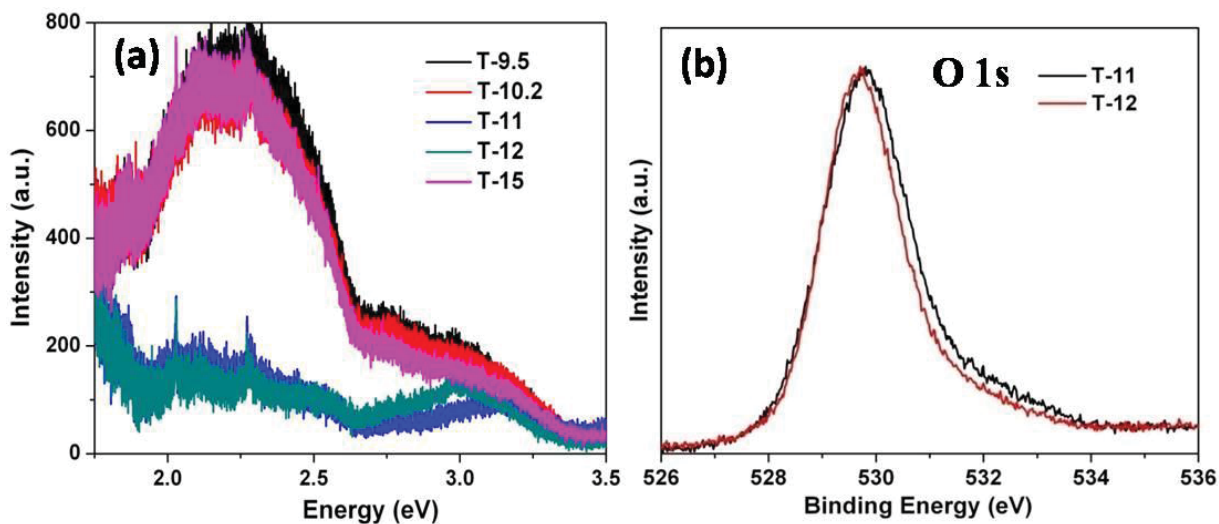


Figure 4.4 (a) PL spectra TiO₂ nanotubes synthesized at different voltages (b) O 1s XPS spectra comparison of T-11 and T-12.

traps^{247,248}. The broad green emission peaked at 2.3 eV is usually assigned to the surface defects caused by oxygen deficiency and the associated Ti^{3+} ions²⁴⁸⁻²⁵¹. It is noted that the emission intensity in 1.75 eV to 2.65 eV is quenched for T-11 and T-12. This may be due to the passivation of oxygen vacancies residing along the nanotube walls²⁵². This passivation suggests the efficient transport of charge carriers along the axis of the nanotubes²⁵². This is in accord with the observation of high crystallinity and good tubular morphology in T-11 and T-12 (Figure 3.5 c and d) in which the three phases favor efficient transport of excitons for hydrogen generation¹⁶⁰. Compared to T-12, T-11 has slight increase in intensity. This may be due to the presence of excess defects in T-11. The O 1s spectra of T-11 and T-12 are compared in Figure 4.4b. It is clear that there is a slight broadening in T-11 which can be attributed to the presence of excess oxygen vacancies¹⁶. It is well known that the presence of oxygen vacancies in TiO_2 decrease the band gap. This is further confirmed by a slight decrease in band gap of T-11 compared to that of T-12 (Figure 3.7).

The high energy emission in the region from 2.65 eV to 3.4 eV (Figure 4.4) can be either due to the self trapped excitons located at TiO_6 octahedra or due to the near band edge emission. As our samples are composed of different phases, the deconvolution is necessary for the further insight. This is done in the succeeding sections of this chapter for the evaluation of average band gaps of anatase, rutile and brookite phases present in the sample.

4.3.2 TiO_2 nanotubes synthesized at different electrolyte concentrations

4.3.2.1 Mott-Schottky analysis

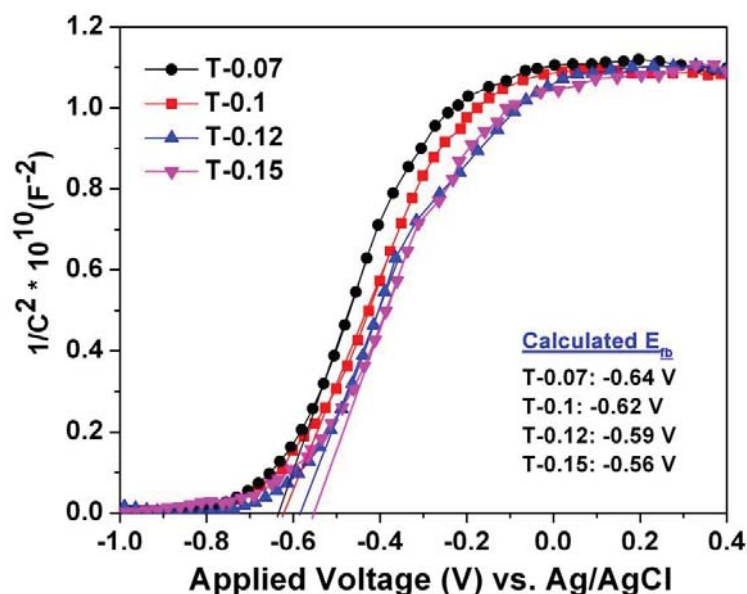


Figure 4.5 MS plots of TiO₂ nanotubes synthesized at different electrolyte concentration in 0.5M Na₂SO₄ at a frequency of 1 KHz, under UV illumination.

Similar to the MS plots of TiO₂ prepared under different voltages (Section 4.3.1.1), the TiO₂ samples synthesized under different electrolyte concentrations also exhibit a positive slope in MS plots (Figure 4.5) indicating n-type semiconducting behavior. The observed cathodic shift in E_{fb} is in the order of T-0.07 > T-0.1 > T-0.12 > T-0.15. These results corroborate with the results of hydrogen generation. In section 4.3.1.1, it is discussed that the degree of FL shift depends on the number of phase junctions. Therefore, the nearly equal E_{fb} of T-0.07 and T-0.1 indicating high charge pair separation can be attributed to the presence of triphase heterojunctions. Whereas decrease in E_{fb} values in samples synthesized with increase in electrolyte concentration as in case of T-0.12 (less triphasic) and T-0.15 (biphase) can be attributed to the transformation of triphase to biphase.

4.3.2.2 Photoluminescence

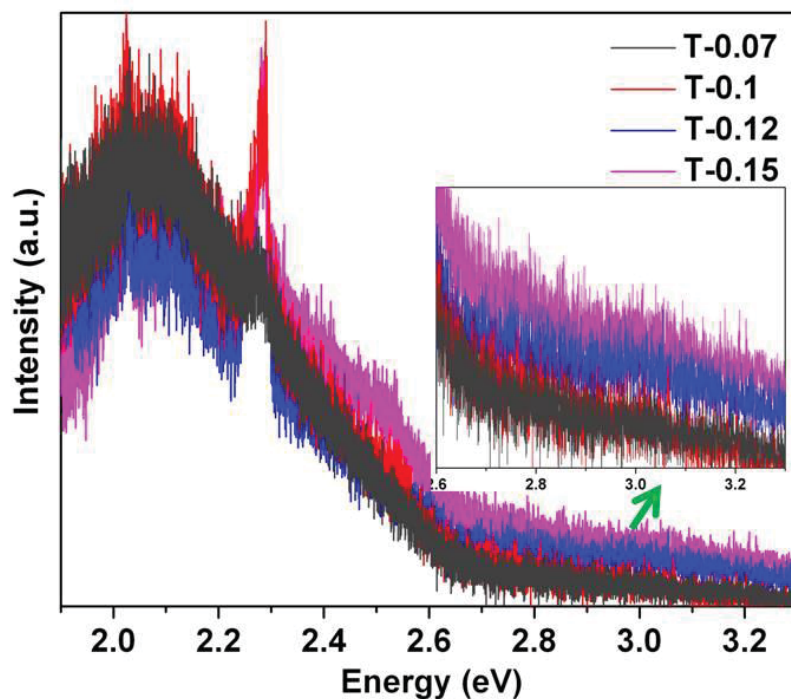


Figure 4.6 PL spectra of TiO₂ nanotubes synthesized at different electrolyte concentration

The PL spectra of TiO₂ nanotubes synthesized under different electrolyte concentrations are given in Figure 4.6. Unlike the PL spectra of TiO₂ nanotubes synthesized at different voltages (Figure 4.4a), the PL intensity of all the samples is nearly same in the energy region from 1.75 eV to 2.4 eV. This indicates that the change in electrolyte concentration doesn't alter the presence of defects. In the near band edge emission region (2.65 eV to 3.4 eV) there is a slight difference in PL intensity among the samples. A close look at this region (Inset of Figure 4.6) reveals that T-0.07 and T-0.1 have same intensity whereas it increased in T-0.12 and more for T-0.15. The variation of intensity can be attributed to the phase composition of different TiO₂ nanotubes as T-0.07 and T-0.1 have triphase composition, whereas T-0.12 is less triphasic and T-0.15 is biphasic.

4.4 Energy Band Alignment and Charge Transfer Pathway in Triphase

TiO₂ Nanotubes

4.4.1 PL spectra in detail

The high energy emission in the region from 2.65 eV to 3.4 eV (Figure 4.4a and Figure 4.6) can be either due to the self trapped excitons located at TiO₆ octahedra or due to the near band edge emission. As our samples are composed of different phases, the deconvolution is necessary for the further insight. To perform it, the PL spectra of TiO₂ nanotubes synthesized at different voltages are considered due to the distinguishable difference in their intensities. The emission spectra of T-9.5, T-10.2, T-11 and T-12 samples are deconvoluted in this region after background subtraction and are represented in Figure 4.7. The peak parameters such as peak centre and area are shown in Table 4.1. It can be seen

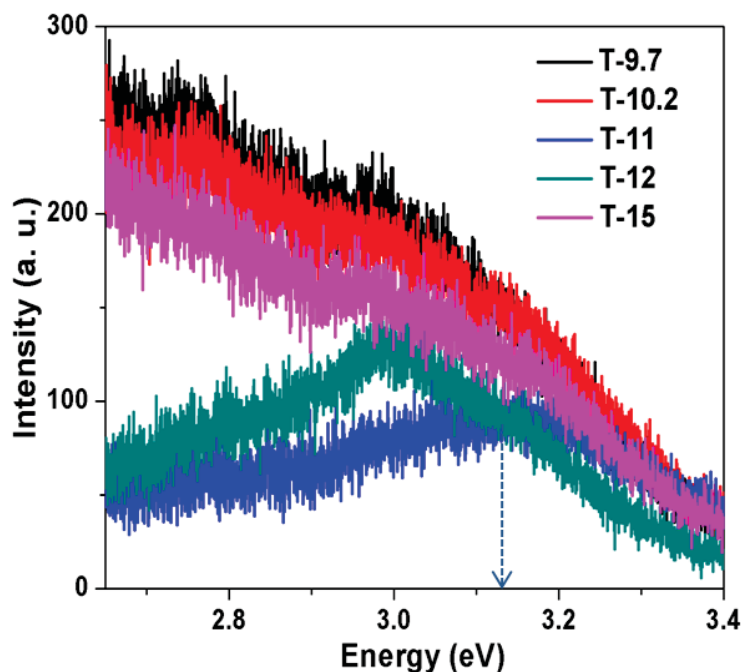


Figure 4.7 A close look of the PL spectra in band gap region from 2.6 to 3.4 eV

from Table 4.1 and Figure 4.7, that only two peaks are fitted into the spectra of T-9.5 and T-10.2, whereas three peaks are required to fit the spectra of T-11 and T-12. The strong emission which appears around 3 eV is dominant in all the samples can be attributed to the allowed indirect transition from the edge to the centre of the Brillouin zone of anatase namely $X_{2b} \rightarrow \Gamma_{1b}$ (3.05 eV) as calculated by Daude et al²⁵³. The band gap estimated from Tauc plot of T-9.5 which is majorly anatase is also calculated to be 3.05 eV. Therefore the value 3.05 eV can be considered as the band gap of anatase phase present in all the samples. The estimated band gap of anatase is lower than the usually reported value 3.2 eV which may be due to the lack of crystallinity (in the case of T-9.5 and T-10.2)¹⁹⁹ and due to the presence of multiple phases as in the case of T-11 and T-12²²².

Our observation of the lowest energy emission around 2.8 eV in the deconvoluted PL spectra of the samples cannot be considered as the typical energy transition $X_{1a} \rightarrow \Gamma_{1b}$ (2.91 eV) in anatase phase proposed by Daude et al²⁵³ as the values are very different. It is also observed that the area of the peak around 2.8 eV is very low in T-9.5 whereas it increased nearly 12 times in T-10.2 and exists in rest of the samples with small variation in area. This leads us to the idea that the peak may be due to the near edge transition in rutile phase which in itself a direct band gap semiconductor. Therefore the low intensity of the 2.8 eV peak in T-9.5 can be attributed to the residual amount of rutile present in the sample as observed in XRD (Figure 3.2). The red shifted rutile peak from the reported value of 2.98 eV may be because of the small crystallite size of rutile in the nanotube²⁵⁴. The peak centered at around 3.2 eV occurring in T-11 and T-12 samples can be attributed either to the band edge transition/lowest energy indirect transition in brookite phase present in the sample or due to

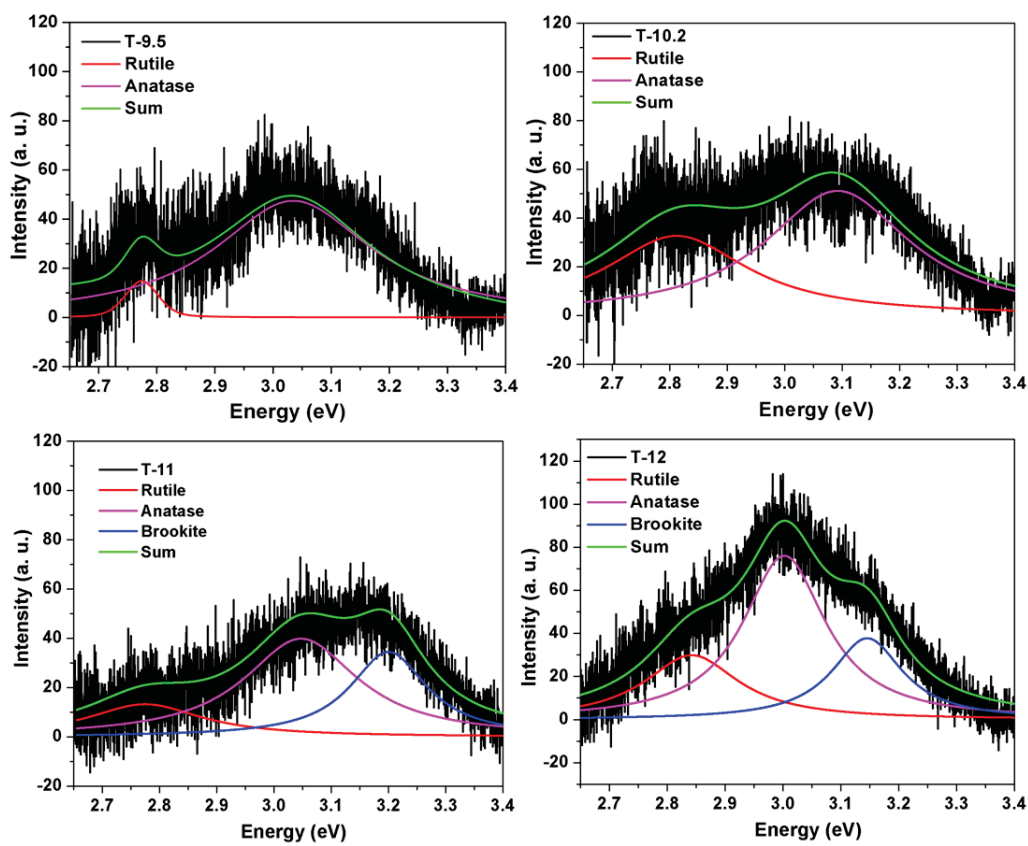


Figure 4.8 Deconvoluted PL spectra of selected TiO₂ nanotubes synthesized at different voltages in the region from 2.6 eV to 3.4 eV

Table 4.1 Deconvoluted peak parameters of PL spectra of selected TiO₂ nanotubes synthesized at different voltages

Sample	T-9.5		T-10.2		T-11		T-12	
	Centre	Area	Centre	Area	Centre	Area	Centre	Area
Peak 1	2.77	1.23	2.81	15.5	2.77	5.08	2.84	9.26
Peak 2	3.03	24.28	3.07	24.53	3.04	15.13	3.02	20.79
Peak 3	-	-	-	-	3.2	8.83	3.19	8.84

the high energy emission of anatase due to the transition $\Gamma_3 \rightarrow X_{1b}$ (3.19 eV) as proposed by Daude et al. However, it is noted that the 3.2 eV peak is absent in T-9.5 and T-10.2 where the brookite phase is absent (confirmed by XRD). Also there are many literatures in which the band gap of brookite is calculated to be in the range of 3.1 to 3.4 eV^{183,240,255-258}. So it is concluded that the peak at 3.2 eV is arising from the band edge transition in brookite phase present in the sample. Thus, it can be roughly estimated from the deconvolution of the PL spectra that the band gap of anatase, rutile and brookite in the triphasic T-11 sample are around 3 eV, 2.8 eV and 3.2 eV respectively

4.4.2 Synchrotron valence band edge analysis

Figure 4.9 shows the UPS spectrum of T-11 sample after background subtraction recorded using incident photon energy of 27 eV. It can be seen that for the VB spectra (low binding energy side, shown in the expanded view) there are three leading edges of the VB (VB onsets). The density of states observed in Figure 4.9 in 0-1 eV region can be attributed to occupied defects states due to partial population of Ti *3d* states²⁵⁹⁻²⁶¹. This is also evident from the O *1s* core level spectra of the sample T-11 (Figure 4.4b), which clearly indicates the presence of oxygen vacancy. The intersection point of the tangents to the leading edge of the VB onset and the zero line is taken as the VB onset point. The points of intersections of the linearly extrapolated tangents with the binding energy axis are found to be 1.85, 2.71 and 2.9 eV.

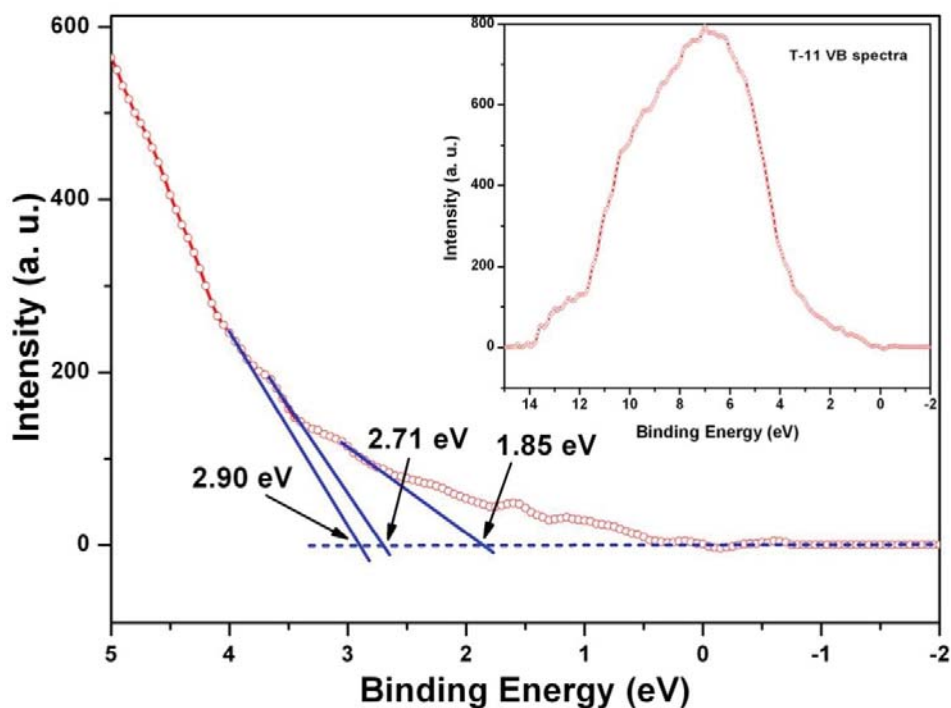


Figure 4.9 Synchrotron photoelectron valence band spectra of T-11

4.4.3 Possible band diagrams

The obtained VB edge values from UPS spectra are 1.85, 2.71 and 2.9 eV. However labeling these VB edge values to the specific phases of T-11 sample is difficult as we have got a single band gap value from DRS. Hence to obtain a clear picture on the VB edges of anatase, rutile and brookite phases in T-11, the assistance of deconvoluted PL spectra are sought. The estimated band gap values of anatase, rutile and brookite phases in T-11 from the deconvoluted PL spectra (Figure 4.8 and Table 4.1) are 3.04, 2.77 and 3.2 eV respectively. The VB edges obtained from the UPS analysis (Figure 4.9) are 1.85, 2.71 and 2.9 eV, which are actually the energy gap between the FL and the VB maxima of the respective phases. According to the compatibility of these two sets of values, the rutile VB edge can be fixed as 1.85 eV as the other values (2.71 and 2.90 eV) gives either near zero or

negative values when subtracted from the band gap of rutile ie 2.77 eV. Therefore two cases are to be considered to draw a band diagram of T-11. They are: case I - fixing anatase VB edge as 2.71 eV and brookite edge as 2.9 eV and case II- fixing anatase edge as 2.9 eV and brookite edge as 2.71 eV. The band diagrams resulted out of these assumptions, are depicted in Figure 4.10. The probable electron transfer pathway for case I, deduced from Figure 4.10a, is rutile to anatase to brookite and the holes transfer in reverse direction. Similarly, the probable electron transfer pathway for case II based on Figure 4.10b, is from rutile to brookite to anatase with holes transfer in opposite direction.

It can be seen that the gap between CB edge and FL of anatase in case II is very less (0.14 eV) compared to that of brookite in case I (0.3 eV) from Figure 4.10. For efficient hydrogen production, the CB edge must be more negative than the reduction potential of H^+ to H_2 ($E_{H^+/H_2} = 0$ V vs. NHE at pH = 0) ²⁶². Hence the electron transfer pathway corresponding to case I (Figure 4.10a) can be considered as the probable one. The overall peak position of PL spectra (the sharp peak in the range of 2.6 eV to 3.4 eV) of T-11 (Figure 4.7) is observed at 3.14 eV which is around the band gap value of brookite. This high emission intensity around brookite can be attributed to the large recombination at brookite phase compared to anatase and rutile phases. This can happen when electrons get accumulated in brookite due to their transfer from rutile to anatase to brookite after excitation by light. A similar transfer pathway is suggested by Kaplan et al¹⁶⁰ as the charge separation is enhanced by the synergistic effect of anatase and rutile as recognized by already reported literatures¹⁶ and due to the preferential oxidation reaction at brookite phases. It is also reported by Scanlon et al¹⁸⁴ that the photogenerated electrons flow from rutile to anatase due to the high electron affinity of anatase in an anatase-rutile composite

whose band gap is significantly lowered. From these observations, it can be concluded that the transfer pathway of electrons in ARB system is from rutile to anatase to brookite.

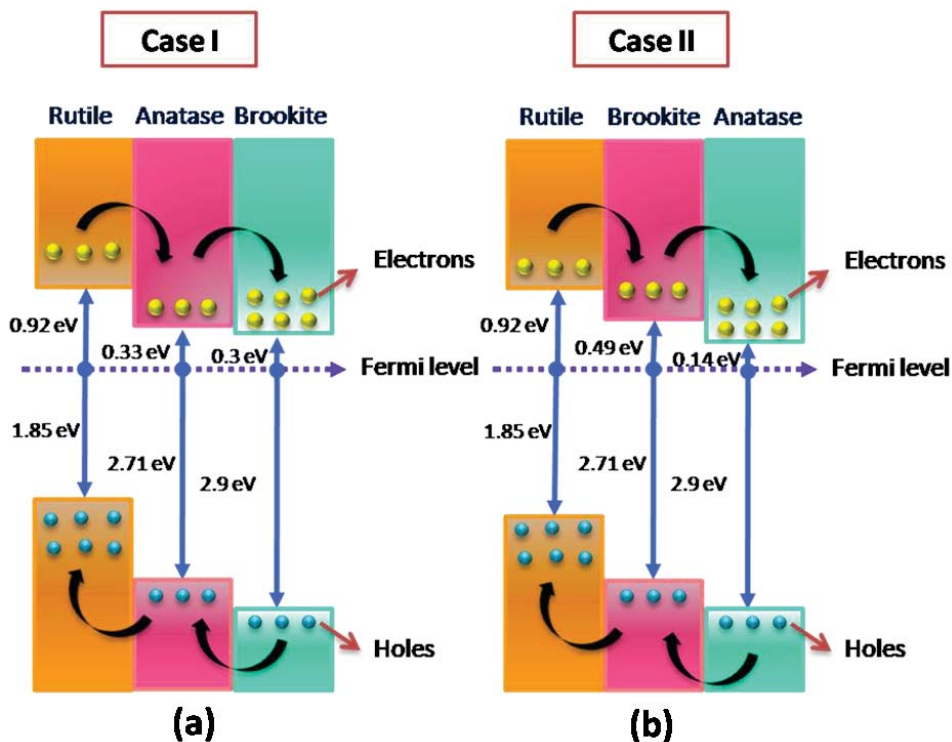


Figure 4.10 Possible band edge positions of T-11 (a) Case I and (b) Case II

The overall peak position of T-12 in Figure 4.7 is at 3 eV which is close to the band gap of anatase ascertained from the deconvolution of PL spectra. This indicates the possibility of higher electron hole recombination in the anatase phase of T-12 sample. A comparison of the deconvoluted PL peak areas of T-11 and T-12 samples (Table 3.1) reveal that the peak area corresponding to the rutile and anatase phases (around 2.8 eV and 3 eV) in T-12 is high compared to T-11; whereas, the peak area corresponding to brookite phase (around 3.2 eV) is almost equal. Therefore it is clear that the relatively-high anatase rutile phase content in T-12 (Table 3.1) causes high charge recombination at anatase and rutile

phases, which substantially decrease the rate of electron transfer to brookite leading to the low photocatalytic efficiency of T-12 compared to T-11.

4.5 Summary

In summary, the present study demonstrates facile synthesis of anatase-rutile-brookite TiO₂ nanotubes and its application in photocatalytic hydrogen generation. The efficiency of triphase TiO₂ in hydrogen generation is compared with anatase-rutile / anatase-brookite and anatase TiO₂ nanotubes. It is found that the triphase TiO₂ is more efficient compared to biphasic and single phase TiO₂ nanotubes in photocatalytic hydrogen generation as evident from both of their values obtained by samples synthesized at different voltages and different electrolyte concentrations. The transfer pathway of charge carriers in triphase TiO₂ nanotubes are determined using deconvolution of PL spectra and VB edge analysis. It is demonstrated that the excited electron transfers from rutile to anatase to brookite in triphase TiO₂.

Photocatalytic Hydrogen Generation Efficiency of Doped Triphase Heterojunctions and Their Band Alignment

The two important factors that affect visible light assisted water splitting ability of TiO₂ are its charge recombination and large band gap. Smooth charge transfer pathways for effective charge separation with tuned band gap for visible light absorption, can be achieved by having large number of nitrogen doped heterojunctions of TiO₂ polymorphs. In Chapter 3, the synthesis of nitrogen doped triphase TiO₂ nanotubes, corresponding to different nitrogen concentrations, are discussed. The present chapter reports the first demonstration of nitrogen doped triphase (anatase-rutile-brookite) TiO₂ nanotubes as sun light active photocatalyst for hydrogen generation with high solar to hydrogen conversion efficiency. In addition, the band alignment and charge transfer pathways in nitrogen doped TiO₂ with triphase heterojunctions are delineated.

5.1 Introduction

The potential of triphase TiO₂ nanotubular structures in photocatalytic hydrogen generation is clearly demonstrated in the previous chapter. In order to extend the photo-absorption to visible light regime, nitrogen has been successfully doped in triphase TiO₂ nanotubes whose synthesis procedures and characterization are presented in Chapter 3. Now, it is essential to study the ability of N-doped triphase TiO₂ in splitting water to generate hydrogen. In addition, it is also required to compare its hydrogen generation ability with nitrogen doped biphasic system as it's the most commonly studied heterostructure. In Chapter 3, it is seen that the change in nitrogen concentration alters the phase composition of nanotubes from ARB to AR. In the present chapter, the hydrogen generation efficiency of nitrogen doped triphase and biphasic TiO₂ nanotubes, obtained using the synthesis technique described in Chapter 3, is presented and compared with that of pristine triphase TiO₂ nanotubes. The effects of nitrogen doping on band structure and sunlight/visible light assisted hydrogen generation efficiency are studied in detail.

5.2 Photocatalytic Hydrogen Generation

Nitrogen doped triphasic TiO₂ nanotubes (N-TiO₂), corresponding to different nitrogen concentrations are synthesized using RBA technique having 0.5, 1.5, 3 and 4.5 wt% hydrazine hydrate as nitrogen source in the electrolyte solution. The resultant samples are labeled as NT-0.5, NT-1.5, NT-3 and NT-4.5 (Section 3.3). The nitrogen concentration present in NT-0.5, NT-1.5, NT-3 and NT-4.5 are estimated to be 0.19, 0.29, 0.37 and 0.48 at % respectively from the N 1s spectra obtained from XPS analysis whose details are given in

later sections. The hydrogen generation experiments are carried out for all the N-TiO₂ photocatalysts along with pristine triphase TiO₂ nanotubes (T-ARB) in water/ethanol mixture under one sun conditions. The experimental details are given in Chapter 2. The hydrogen generation results are depicted in Figure 5.1. It is clear from Figure 5.1 that the volume of hydrogen generation of TiO₂ polymorphs increased after nitrogen doping. The hydrogen generation efficiency of the given photocatalyst is in the order of NT-1.5 > NT-0.5 > NT-3 > NT-4.5 > T-ARB. The hydrogen generation of T-ARB after 4 hours of light irradiation is estimated to be 2 mmol/g. The maximum hydrogen generation of 15.2 mmol/g is produced by NT-1.5 polymorph after 4 hours of light illumination. It is already clear from Chapter 3 that NT-0.5, NT-1.5 and NT-3 possess triphasic nature whereas NT-4.5 is biphasic (Figure 3.12).

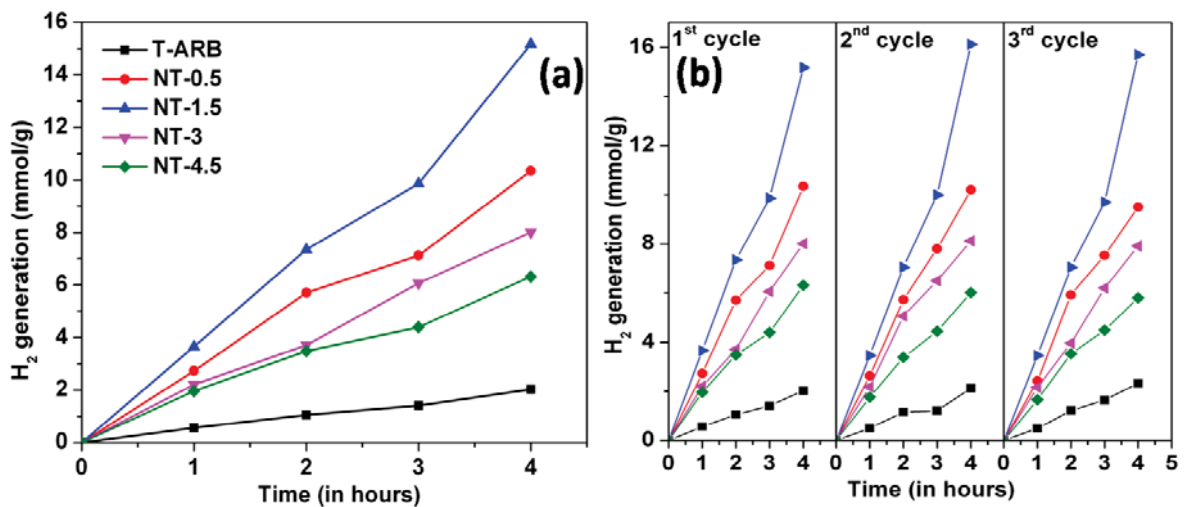


Figure 5.1 (a) Cumulative hydrogen generation of T-ARB and N-TiO₂ and (b) verification of their stability under one sun condition with ethanol as sacrificial agent. The area of illumination is 12 cm².

Sample NT-1.5 exhibits better efficiency compared to NT-0.5 (10.3 mmol/g for 4 hrs of light illumination) because of higher nitrogen content. The lower efficiency of NT-3 (8 mmol/g for 4 hrs of light illumination) compared to NT-0.5 and NT-1.5 despite its higher nitrogen doping is attributed to its low three phase content. The brookite content in NT-3 is very less that it acts almost like biphasic TiO₂. The hydrogen generation efficiency is lowest for NT-4.5 (6.3 mmol/g for 4 hrs of light illumination) which is attributed to the absence of brookite phase; which likely leads to lower charge separation because of lower number of bulk heterojunctions and hence low activity.

To verify the reusability and the long term stability of the photocatalyst, H₂ generation measurements were carried out in 3 cycles (Figure 5.1b). All three cycles shows the same trend as well as the same range of values of hydrogen generation for different photocatalysts. Thus, reusability of N-TiO₂ photocatalysts is discerned from the results.

The STH conversion efficiency of the samples T-ARB, NT-0.5, NT-1.5, NT-3 and NT-4.5 (for 10 mg of photocatalyst taken) is calculated to be 0.03, 0.17, 0.2, 0.13 and 0.1 % respectively.

5.3 Charge Separation Efficiency

To ascertain the improvement in charge separation due to band alignment in multiphase system, MS analysis is performed under UV light for pristine and N-TiO₂ nanotubes in 0.5 M Na₂SO₄ electrolyte as explained in Chapter 2. Figure 5.2 represents the MS plots, from which E_{fb} is calculated using the MS relation¹⁶ (Equation 2.14).

All samples exhibit a positive slope in MS plots, as expected for n-type semiconductors. The observed cathodic shift in E_{fb} is in the order of NT-1.5 > NT-0.5 > NT-3 > NT-4.5 > T-ARB. The hydrogen generation values also follows the same trend (Figure 5.1). When TiO₂ is irradiated, the upward shift of the FL enhances the charge separation at the semiconductor/electrolyte interface. The resultant electrons in CB and holes in the VB take part in the redox reaction^{218,246}.

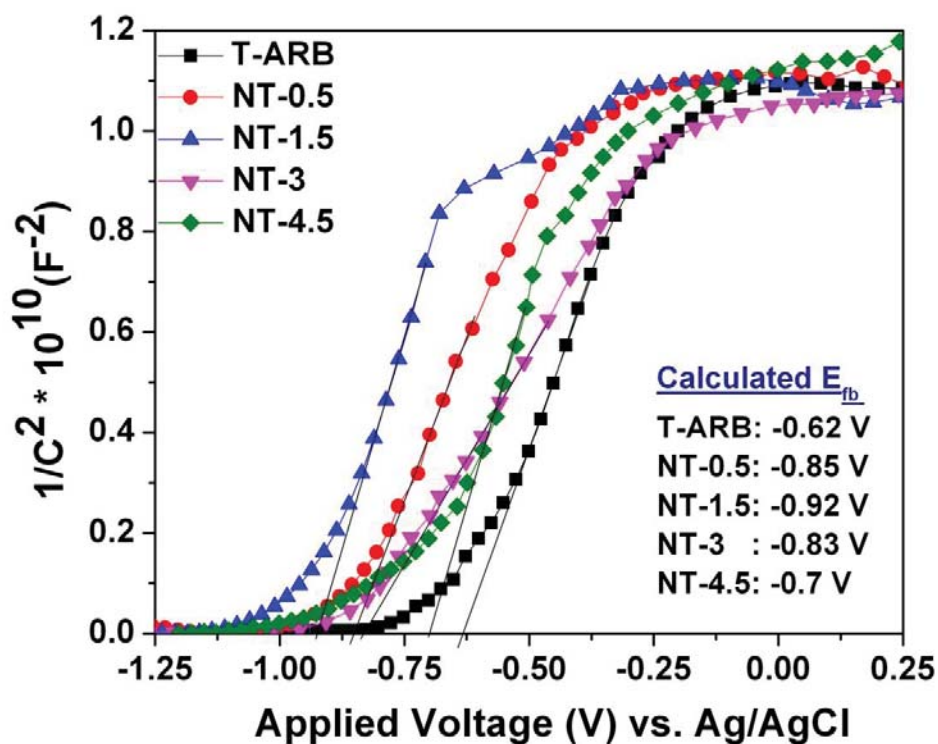


Figure 5.2 MS plots of T-ARB and N-TiO₂ nanotubes in 0.5M Na₂SO₄ at a frequency of 1 KHz, under UV illumination

In a multi-phase system, under UV illumination, the excited charge carriers transfer from one phase to another leading to a higher shift in the FL towards the CB edge. The degree of FL shift depends on the number of phase junctions present⁸⁰. In the present case,

shift in FL is affected by two factors viz. N doping and phase composition. The T-ARB sample exhibits low E_{fb} among all the samples after irradiation, because the FL shift is contributed only by triphase composition as there is no N doping. As we can see from the E_{fb} values, the nitrogen doped triphase samples such as NT-0.5, NT-1.5 and NT-3 possess same range of values compared to N-doped biphasic NT-4.5. This indicates that the charge separation is better in case of nitrogen doped triphase samples.

The highest E_{fb} is observed in NT-1.5 which is the best photo active sample as discerned from hydrogen generation experiments. The crystallite size analysis indicates that NT-1.5 (Table 3.3) possess overall smaller crystallite size of anatase, rutile and brookite compared to other doped triphase samples (NT-0.5 and NT-3). This smaller crystallite size would lead to more number of bulk heterojunctions and is expected to assist in effective charge separation. This is reflected in the Mott-Schotky plots presented above (NT-1.5 > NT-0.5 > NT-3). Further, the presence of all three phases in close proximity in NT-1.5, as observed from the HRTEM analysis (Figure 3.15c and d), makes it an efficient photocatalyst for water splitting.

5.4 Energy Band Alignment and Charge Transfer Pathway in N-Doped Triphase TiO₂ Nanotubes

5.4.1 XPS and UPS analysis

To investigate the change in surface bonding of TiO₂ induced by nitrogen doping, XPS analysis is performed for all the samples which are deconvoluted and presented in Figure 5.3a. The Ti 2*p* core level spectrum of all samples, deconvoluted using CasaXPS,

exhibited Ti $2p$ spin-orbit doublet centered at binding energies 458.6 and 464.1 eV, that corresponds to Ti $2p_{3/2}$ and Ti $2p_{1/2}$ core levels of Ti^{4+} species, respectively. Our observation is in agreement with the literature^{241,263}. In addition, the presence of shoulder peaks around 456.8 and 462 eV indicate the presence of Ti^{3+} in pristine T-ARB as well as in N-TiO₂ samples. The area of Ti^{3+} peak increases with increase in N doping by 7.8% in NT-0.5, 13% in NT-1.5, 23% in NT-3 and 24.7 % in case of NT-4.5 compared to that in T-ARB. The localization of charge carriers generated due to oxygen vacancy formation at Ti^{4+} could be the cause for the reduction of Ti^{4+} to Ti^{3+} .

The O $1s$ spectra of all the samples are deconvoluted into two peaks which are centered at 529.8 and 531 eV which are represented in Figure 5.3b. The O $1s$ spectra of pristine TiO₂ centered around 529.8 eV corresponding to the lattice oxygen. In addition to this lattice oxygen signature peak, a shoulder can be discerned at higher binding energies, whose area increases with increase in nitrogen doping (Figure 5.4a). The shoulder peak at 531 eV occurring in nitrogen doped polymorphs is attributed to the surface hydroxyl group (Ti-OH)¹⁶. The quantity of OH species increases initially with increase in nitrogen doping however it remains unaltered at higher degree of nitrogen doping as in the case of NT-3 and NT-4.5 (Figure 5.4a). The area of the peak at 531 eV increases by 6% in NT-0.5, 11% in case of NT-1.5 and 19% (average) in case of NT-3 and NT-4.5 respectively compared to that in T-ARB.

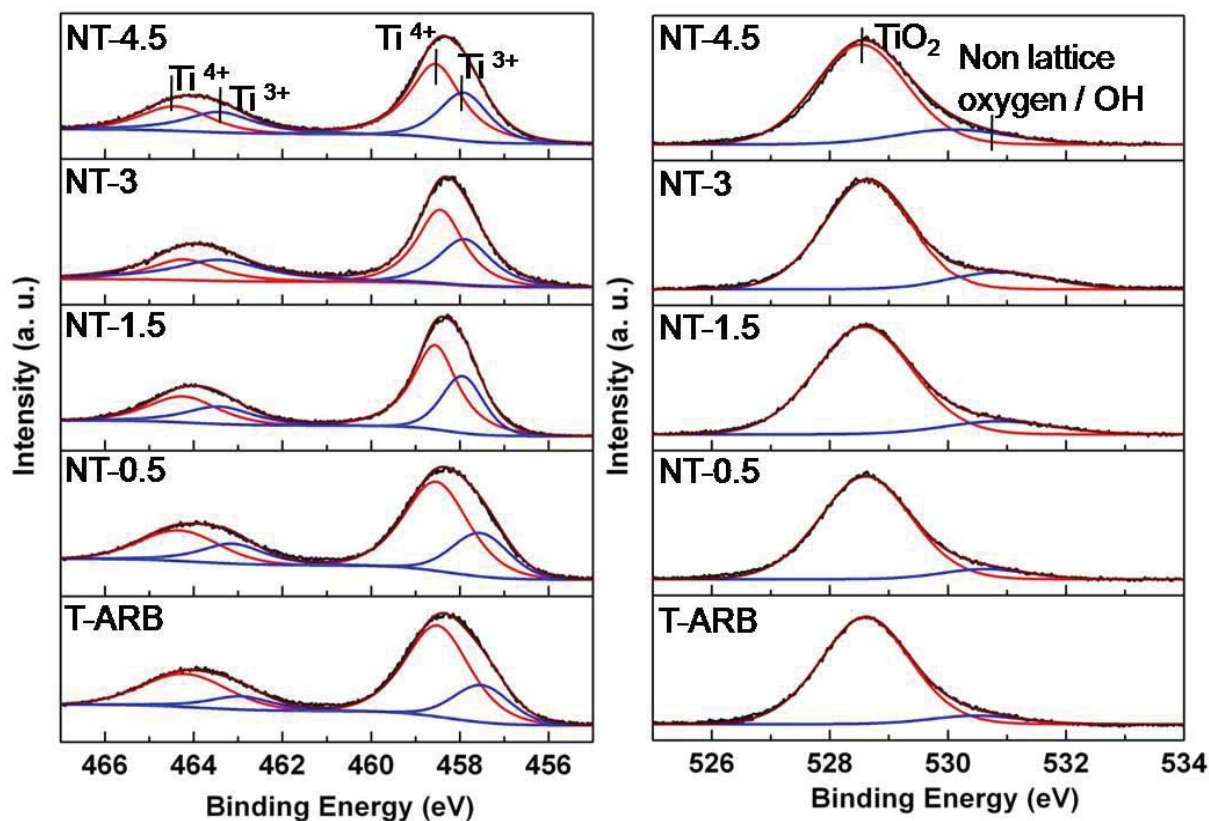


Figure 5.3 Deconvolution of (a) Ti 2*p* and (b) O 1*s* spectra of T-ARB and N-TiO₂ nanotubes

Incorporation of nitrogen into the lattice results in the formation of oxygen vacancies in order to maintain charge neutrality. The oxygen vacancies at the surface take the form of missing oxide ions in the bridging oxygen row (bridging oxygen vacancies in the form: Ti³⁺ - V_o - Ti³⁺ where V_o denotes the oxygen vacancy) leading to the formation of co-ordinatively unsaturated Ti³⁺ ions. These Ti³⁺ ions have distorted coordination geometry, because of adjacent oxide ion vacancies. They have a tendency to form additional coordination and therefore, the oxygen vacancies act as adsorption sites for organic and water molecules thereby playing an important role in the photo-oxidation²⁶⁴.

When water molecules come in contact with nanotube surface, they are adsorbed at the bridging oxygen vacancies to form Ti – OH - Ti bridge^{264,265}. The bridging hydroxyl groups are in close proximity to adsorbed water molecules and hence form, through hydrogen bonding, hydrated bridging OH²⁶⁶. The hydrated bridging OH groups offer a channel for the transfer of photo-generated holes, giving rise to 2H⁺, Ti-OH and Ti-O⁻ species²⁶⁶. The generated H⁺ species are reduced to H₂ by the photo-generated electron and the two adjacent Ti-O⁻ species couple to form surface peroxide. With increase in nitrogen doping, oxygen vacancy concentration increases which in turn increases hydrated bridging OH group resulting in enhanced hole assisted photo-catalytic reaction.

However, in the present study, the expected trend is not observed. An initial increase in hydrogen generation with increase in N-doping followed by decrease in hydrogen generation is observed. The initial increase in hydrogen generation can be attributed to the increase in light absorption due to nitrogen doping, the presence of bulk heterojunctions due to the inter band states, in addition, to the increase in surface hydroxyl group. Although, the increase in nitrogen concentration increases the photo-absorption and surface hydroxyls, the subsequent reduction in hydrogen generation with increase in N-doping is observed. This can be attributed to the decrease in three phase content with increase in N-doping and only two phases (anatase-rutile) are present at highest N-concentration (NT-4.5). This shows that in N-doped samples, the effect of phase content overshadows the effect of surface hydroxyl group. Presence of N-doping can be understood from the high resolution N 1s spectra analyzed for pristine and N-doped samples which are represented in Figure 5.4b. The peaks are positioned around 398.7 in all the samples which correspond to doped nitrogen, which is consistent with our previous report and other reports found in literature^{102,267-269}.

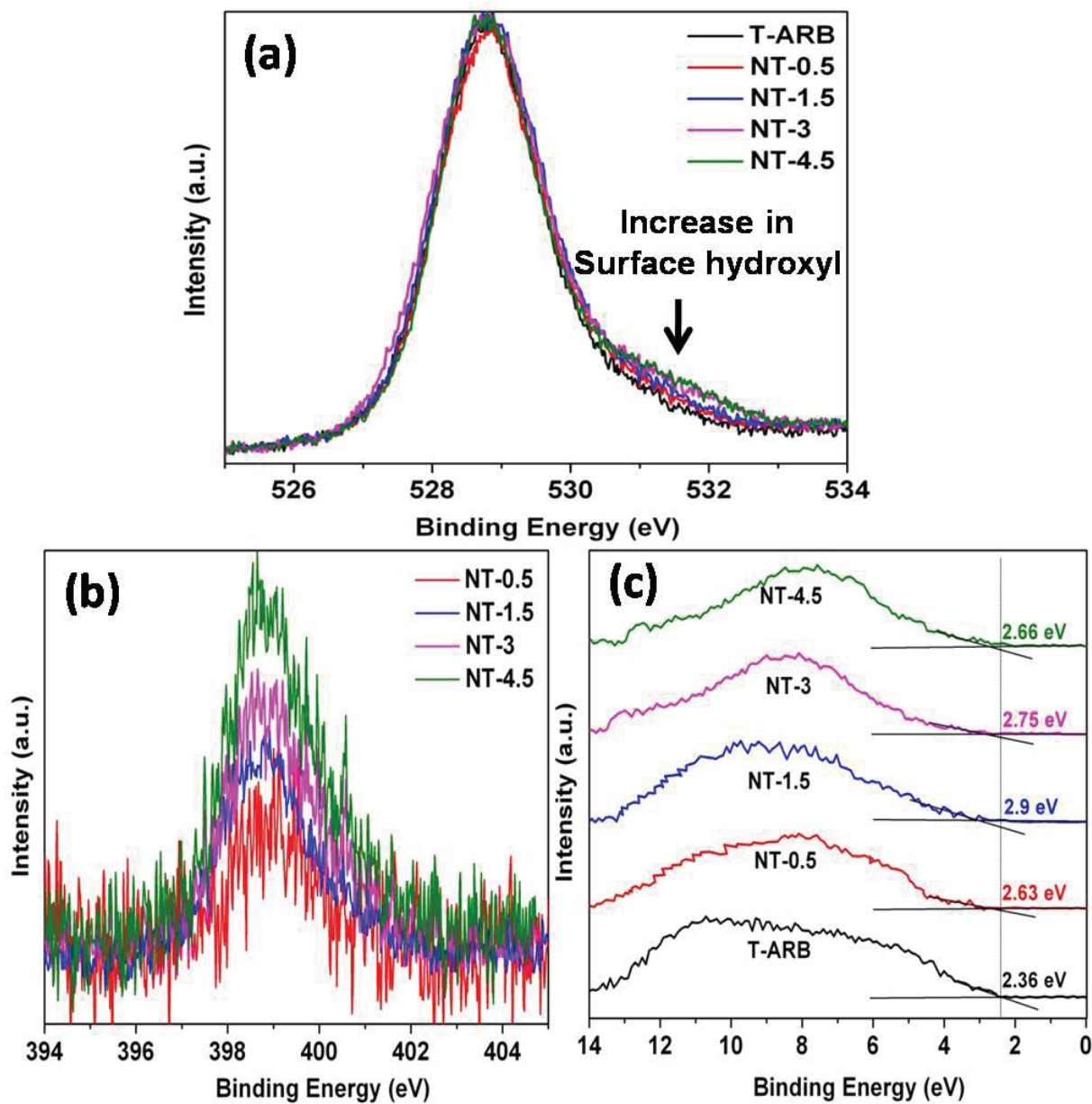


Figure 5.4 (a) O 1s, (b) N 1s and (c) UPS spectra of T-ARB and N-TiO₂ nanotubes

The N 1s peak intensity gradually increases from NT-0.5 to NT-4.5 which confirms that the quantity of nitrogen doping in TiO₂ crystal increases with increase in hydrazine hydrate concentration. The nitrogen content in NT-0.5, NT-1.5 and NT-4.5 are calculated to be of 0.19, 0.29, 0.37 and 0.48 at % respectively.

In order to identify the effect of nitrogen doping on VB offsets, UPS analysis was performed for all the samples. Figure 5.4c shows that the UPS spectra of both pristine and N-TiO₂ samples. The obtained VB edge values of the samples are listed in label of Figure 5.4c. It is noticed that as we increase the nitrogen content, the gap between the VB edge to FL increases from T-ARB until NT-1.5, whereas it starts to decrease with the further increase in nitrogen doping (as for the case of NT-3 and NT-4.5). However it is noticed in band gap analysis from DRS that the band gap decreases with nitrogen doping. The results indicate that the FL shifts towards CB edge until the doping is at 0.29% (NT-1.5), then it starts to shift away from the CB edge as in the case of NT-3 and NT-4.5 where the nitrogen doping is high. This can be attributed to the change in phase composition upon nitrogen doping which changes the FL position⁸⁰. As in the case of low nitrogen doping, the Ti³⁺ defects states and N 2*p* density start to increase. At higher nitrogen doping, it is observed that the Ti³⁺ defects are unaltered whereas the N 2*p* states grow denser. This should in turn decrease the gap between the FL and VB edge at higher N doping. However it is not observed so in our case. This is due to the presence of multiple phases, where the FL is near to CB edge in triphase system and it start to shift away from CB edge when the triphase system is converted to biphasic system. The results coincide with the MS results where we see similar pattern in E_{fb} . Thus phase composition plays a major role in hydrogen generation reactions as triphase increases the charge pair separation compared to biphasic system.

5.4.2 Photoluminescence

PL spectra of pristine and N-TiO₂ nanotubes are shown in Figure 5.5. The PL spectra can be divided into two regions viz. region 1.8 to 2.7 eV and 2.7 to 3.4 eV. The PL intensity in the former region is due to the defects present in the samples, whereas the later is due to

the band edge emission⁸⁰. All samples exhibited a secondary peak emission in the range of 1.8 to 2.7 eV. The peak around 2.1 eV is due to oxygen vacancy related defects in addition to the under-coordinated Ti acting as electron traps^{247,248}. The peak around 2.3 eV is due to the surface defects caused by oxygen deficiency and the associated Ti^{3+} ions²⁴⁸⁻²⁵¹. For pristine TiO_2 , the intensities of secondary peaks are nearly equal to that of main emission peaks (around 3 eV). For N- TiO_2

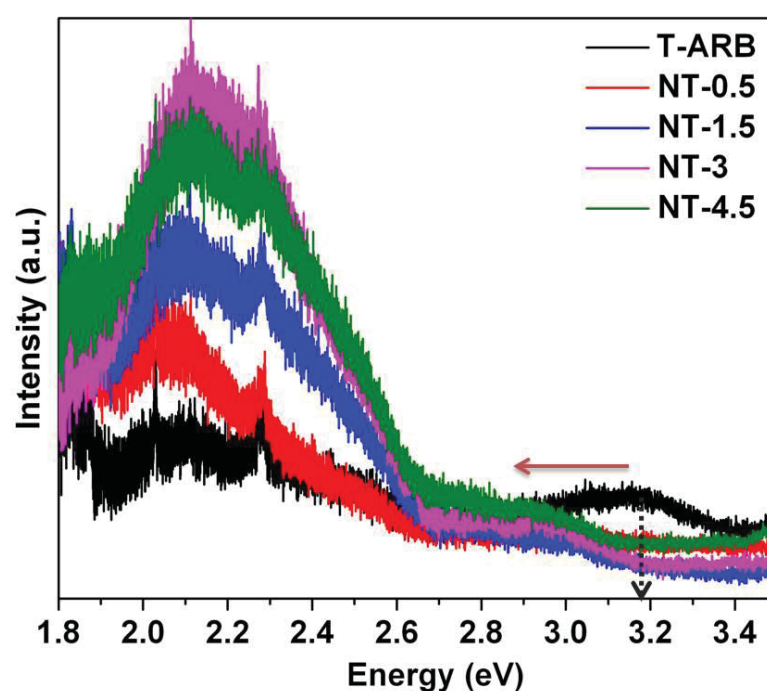


Figure 5.5 PL spectra of T-ARB and N- TiO_2 nanotubes

polymorph the relative intensity of the secondary peaks is enhanced remarkably, when compared with the main emission peaks. This demonstrates the formation of oxygen defects in the TiO_2 lattice as an effect of nitrogen doping. It is also observed that the defects in TiO_2 increase as we increase the nitrogen doping precursor concentration from 0.5 to 3 wt% and then it remains almost constant from 3 to 4.5 wt%. This study proves that nitrogen doping is accompanied by the formation of oxygen vacancies. Even though the higher intensity PL of

N-TiO₂ samples in this region indicates a high radiative recombination of charge pairs, the majority of non-radiative recombination that releases phonons, in general, is a major pathway for the photogenerated charge annihilation in TiO₂ (as in indirect band gap semiconductors)¹⁴⁶. It is already proved that N-TiO₂ possesses better photocatalytic activity compared to pristine TiO₂. Therefore, the results demonstrates that the N-TiO₂ have a lower non-radiative recombination rate compared to pristine T-ARB.

When we compare the band edge emission region in the spectra (2.7 to 3.4 eV) for all the samples, it is observed that T-ARB has highest emission which is indicative of high recombination. It is observed that the main emission peak is shifted to lower energy for the N-doped samples which indicates that there is a decrement in band gap (pointed in Figure 5.5). The main emission peak of doped TiO₂ polymorphs are in the order of NT-4.5 > NT-3 > NT-0.5 > NT-1.5. The low PL main emission intensity of N-TiO₂ is indicative of the forbidden recombination of photogenerated electrons and holes. It is clearly observed that NT-1.5 is having the lowest emission and the band edge emission peak intensity of all the samples inversely follows the trend observed in hydrogen generation efficiency ie lowest emission tends to higher hydrogen generation. However, higher nitrogen doping as in the case of NT-3 and NT-4.5 creates lot of vacancies which tends to behave as recombination centers hence increases the recombination rate thus leading to poor hydrogen generation efficiency. The highest recombination is observed in NT-4.5 which may be due to either high nitrogen doping whose defect states act as recombination centers or due to the difference in number of phases present. It is already noted that the emission peak intensity due to defects in the former region of PL spectra of NT-4.5 and NT-3 are almost similar. Therefore the most probable reason for high band edge emission intensity of NT-4.5 is due

to its biphase nature that decreases the rate of electron-hole pair separation hence increases the recombination compared to NT-3. From the above results it is clear the defects created are saturated with increase in nitrogen doping (as in NT-3 and NT-4.5) but affect the phase composition leading to ARB to AR transformation.

5.4.3 Effect of N doping in triphase TiO₂ nanotubes

Combining the results of the above analysis, a schematic diagram to illustrate the effect of nitrogen doping in triphasic TiO₂ in comparison with pristine T-ARB has been derived and is depicted in Figure 5.6. The growth of Ti³⁺ and N 2p states are clearly depicted in the figure. The

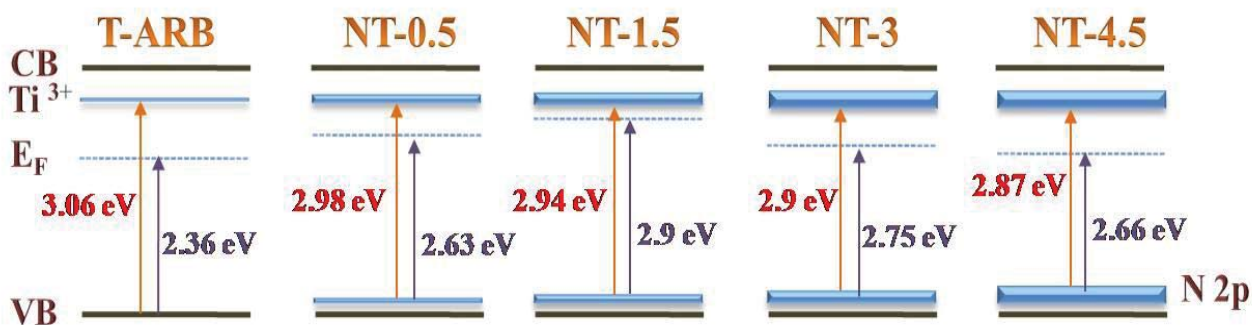


Figure 5.6 Effect of nitrogen doping in triphase TiO₂ nanotubes

presence of oxygen vacancies generated under the synthesis conditions in T-ARB gives rise to Ti³⁺ level below the CB. When T-ARB is doped with nitrogen as in NT-0.5 and NT-1.5, the Ti³⁺ state and N 2p state grow denser, leading to the decrement in band gap and increment in shift of E_F towards CB. At higher nitrogen doping, as in case of NT-3 and NT-4.5, the density of Ti³⁺ states reach a saturation level, as evident from O 1s (Figure 5.4a) and PL spectra (Figure 5.5). The increase in N 2p density of states leads to further decrement of band gap in these samples. However the FL shifts away from the CB edge as seen from MS

analysis. This is due to the decrement in brookite phase concentration in NT-3 and its absence in NT-4.5.

5.4.4 Charge transfer mechanism

From UPS analysis, it is clear that there is alteration in VB edge due to N doping. It is also clear that the nitrogen doping increased Ti^{3+} defects as confirmed from XPS and PL spectra analysis. Based on the above analysis of N-TiO₂ in comparison with pristine T-ARB, the schematic for the effective photocatalytic charge transfer mechanism in NT-1.5 is proposed (Figure 5.7). Because of the synthesis conditions and nitrogen doping, Ti^{3+} levels are formed below the CB edge and N 2p states appear above the VB edge of each phase as depicted in Figure 5.7. When NT-1.5 is photo-irradiated, the electrons in VB and N 2p states of each phase absorb photoenergy and excited to their CB and Ti^{3+} states depending upon the absorbed photoenergy that varies from UV to Visible light.

Since the CB and VB edge positions of anatase, rutile and brookite are different; the Ti^{3+} and N 2p levels in one phase will be close to CB and VB of the adjacent phase respectively. This paves way for easy transfer of excited charge carriers thereby increasing the charge separation. The excited electron transfer pathway in triphase system is assumed to be from rutile to anatase to brookite⁸⁰. The excited electrons in Ti^{3+} state of rutile phase transfers to anatase CB, whereas electrons in Ti^{3+} transfers to brookite CB leading to the high life time of charge carriers which will be available for hydrogen generation reactions. In addition the excited electron in the CB of each phase transfers to its adjacent phase. Similarly, the holes in VB and N 2p of one phase flow in reverse direction through VB and N 2p states of adjacent phase. Thus more number of charge carriers will be available for hydrogen generation reactions. The presence of Ti^{3+} defect states and N 2p in triphase TiO₂ appears to

make a significant difference in catalytic activity. This is why we notice 7.5 times of hydrogen generation in NT-1.5 compared to pristine triphase TiO₂ (T-ARB).

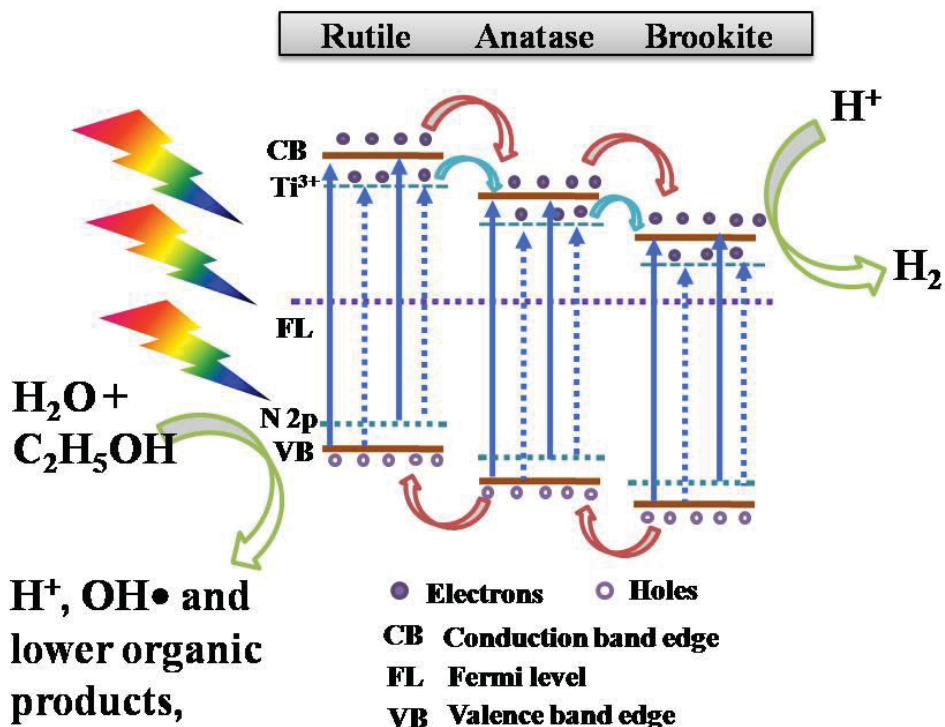


Figure 5.7 Schematic diagram for efficient charge transfer mechanism in NT-1.5

5.4.5 Synchrotron valence band edge spectra

In our previous study on T-ARB (Chapter 4)⁸⁰, the angle resolved photoelectron spectroscopy (ARPES) using synchrotron radiation with incident photon energy of 27 eV is used to probe its VB features, whose results are represented here again in Figure 5.8a. Three leading edges (VB onsets) of the VB are observed. The points of intersections of the linearly extrapolated tangents along these edges with the binding energy axis are found to be 1.85, 2.71 and 2.9 eV. Each of these values corresponds to VB edge of one of the three phases present in the sample. Thus synchrotron UPS fetched us a clear resolution in the VB edge

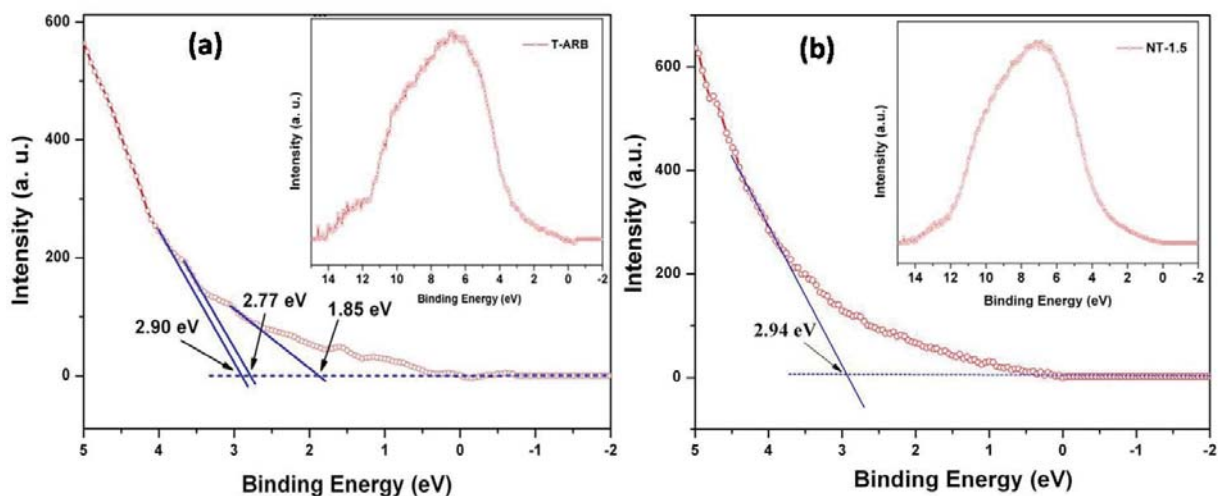


Figure 5.8 Synchrotron valence band spectra of (a) T-ARB; and (b) NT-1.5

features of triphasic T-ARB. Hence in order to distinguish the modified VB edge features, the synchrotron UPS is performed for NT-1.5 whose results are given in Figure 5.8b. There is no clear resolution of three leading edge VB onsets as observed in case of T-ARB (Figure 5.8a). Only one VB onset value is obtained which is around 2.94 eV. The absence of clear resolution in the VB onsets in the UPS spectra corresponding to NT-1.5 in contrast to that of T-ARB is due to the presence of N $2p$ states above the VB of each phase which are closely coupled as depicted in Figure 5.7.

5.5 Summary

The hydrogen generation efficiencies of N-TiO₂ nanotubes are evaluated in comparison with pristine triphase TiO₂. The highest solar hydrogen generation (15.2 mmol/g) obtained by NT-1.5 is due to the optimum nitrogen doping in triphase structure. This value is 7.5 times higher than that of pristine triphase TiO₂ and 2.4 times higher than nitrogen doped biphasic (AR) TiO₂. The variation in density of intra-band states (Ti³⁺ / oxygen vacancies and N $2p$ states) with increase in nitrogen doping are found to be critical

in tuning the photocatalytic activity of TiO₂ nanotubes. The presence of Ti³⁺ states below the CB edges of each phase and N 2*p* states above VB edge of each phase reduced the band gap making it visible light active photocatalyst. In addition, it facilitated easy transfer of photo-excited charge carriers to the neighbor phase CB, thereby reducing recombination rate and enhancing hydrogen generation efficiency. Thus, bulk heterojunctions among the three phases present in the nanotubes with intra-band defect states is shown to enhance the photocatalytic activity tremendously. Our study also confirms the theory that three phase system is efficient in photocatalysis compared to two phase system.

Hydrogen Annealed Triphasic TiO₂ Nanotubes and Their Photocatalytic Activity

In chapters 3 and 5, synthesis, photocatalytic hydrogen generation and charge transfer pathway of visible light active nitrogen doped triphase titania are discussed. One probable drawback of doping metal/non-metal ions into titania is that the dopants can act as recombination centers. Hence the modification of titania to make it visible light active without the need of external doping is appreciated. In this regard, hydrogen annealing (hydrogenation) of triphase TiO₂ nanotubes is carried out whose synthesis procedure is discussed in Chapter 3. The present chapter deals with the photocatalytic hydrogen generation efficiency in comparison to pristine triphase TiO₂ nanotubes under solar light illumination. The possible band alignment and charge transfer pathway is discussed.

6.1 Introduction

In the previous chapter, nitrogen doping in triphase TiO₂ nanotubes to enhance the visible light absorption of triphase TiO₂ are discussed. However the introduction of foreign atoms into TiO₂ lattice can be disadvantageous as the dopants themselves acts as recombination centers. Therefore it is always advantageous to induce native defects rather than external doping. Hydrogenation of TiO₂ to obtain black titania for visible light photocatalysis has got wide attention due to the absence of foreign atoms and creation of native defects. In this regard, the hydrogenation of triphase TiO₂ polymorphs was carried out whose characterizations are given in Chapter 3. The present chapter focuses on the evaluation of photocatalytic hydrogen generation efficiencies of hydrogenated triphase TiO₂ nanotubes. It is demonstrated that the generated defect states in each phase in the triphase system facilitate visible light absorption and easy transfer of excited charge carriers from one phase to the neighbor phase without recombining, thus enhancing the hydrogen generation efficiency. The work is carried out with an aim to build an ideal photocatalyst by exploiting the multiphase junctions towards charge separation and visible light absorption.

6.2 Photocatalytic Hydrogen Generation

The photocatalytic hydrogen generation experiments of the pristine TiO₂ nanotubes (T-ARB) and that annealed in hydrogen atmosphere at 250 and 450 °C (H-250 and H-450) as well as in air at 250 and 450 °C (represented as Air-250 and Air-450) are carried out in water, containing ethanol as a sacrificing agent. The H₂ generation rate at different time intervals are depicted in Figure 6.1. It is noticed that the hydrogen generated by

hydrogenated TiO_2 is greater than the pristine TiO_2 . The highest hydrogen evolution of 27 mmol/g is observed for H-450, whereas it is 12 and 1.7 mmol/g for H-250 and pristine triphase T-ARB respectively, after 4 hours of light irradiation. The air annealed samples shows better efficiencies than pristine T-ARB due to the improved crystallinity; however the rate is not equivalent to that of H-250 and H-450. It is therefore clear from the comparison of hydrogen generation capability of hydrogen annealed and air annealed triphase TiO_2 nanotubes that the improvement in crystallinity of the triphase samples plays only a small role in water splitting. The huge difference in hydrogen generation of hydrogenated samples compared to that of air annealed samples can be attributed to the presence of native defects.

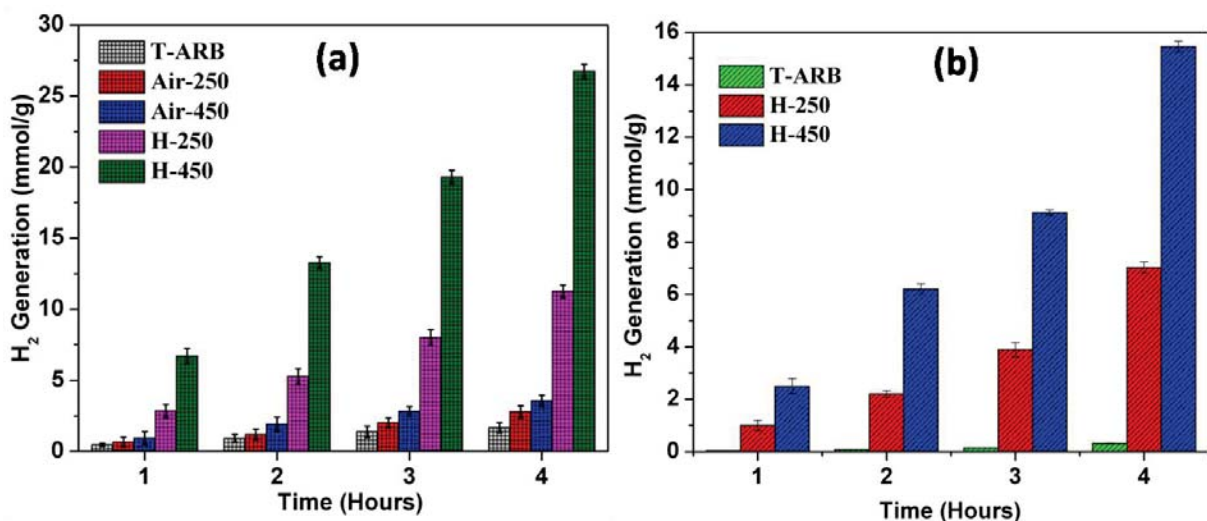


Figure 6.1 Cumulative hydrogen generation of T-ARB and hydrogenated TiO_2 under (a) one sun conditions and (b) visible light with ethanol as sacrificial agent (The error bars in the figure are standard error values of three tests). The area of illumination is 12 cm^2 .

These defects in hydrogenated samples decrease the band gap leading to enhanced absorption of incident light. In addition, the presence of triphase junctions aid the efficient charge transport across junctions and thereby inhibiting the electron hole pair

recombination, paving way for enhanced photocatalytic activity. In order to understand the role of visible light absorption of hydrogenated TiO₂ samples, the hydrogen generation experiments are performed under visible light irradiation (obtained using visible band pass filter) whose results are plotted in Figure 6.1b. It is evident that the hydrogenated samples perform better than pristine T-ARB, which is attributed to the extended photo-absorption tail from 400 - 550 nm of hydrogenated samples (Figure 3.20). It is expected that H-250 and H-450 should deliver nearly the same amount of hydrogen due to their almost near band gap values and absorption tail. However, the visible light hydrogen generation results follows the pattern H-450 > H-250 > T-ARB similar to the hydrogen generation values obtained under one sun condition. This is because of the high density of Ti³⁺ states in H-450. Among the hydrogenated triphase samples, H-450 is best at its efficiency generating around 16 times of hydrogen under one sun condition and around 50 times of hydrogen under visible light irradiation when compared to that of pristine TiO₂. The high efficiency of H-450 can be attributed to the high crystallinity, high percentage of defects and low band gap as confirmed from XRD and DRS (discussed in Chapter 3) as well as PL and XPS (discussed in following sections). The STH conversion efficiency of 10 mg of samples such as T-ARB, H-250, H-450, Air-250 and Air-450 tested under AM 1.5G is calculated to be 0.03, 0.19, 0.44, 0.06 and 0.6 % respectively.

6.3 Charge Separation Efficiency

To ascertain the improvement in charge separation due to favorable band alignment in hydrogenated triphase system compared to pristine triphase TiO₂, MS analysis is performed under UV light for T-11, H-250 and H-450 samples in 0.5 M Na₂SO₄ electrolyte.

Figure 6.2 represents the MS plots, from which E_{fb} is calculated using the MS relation in Equation 2.14¹⁶ and the calculated E_{fb} values are given in Figure 6.2.

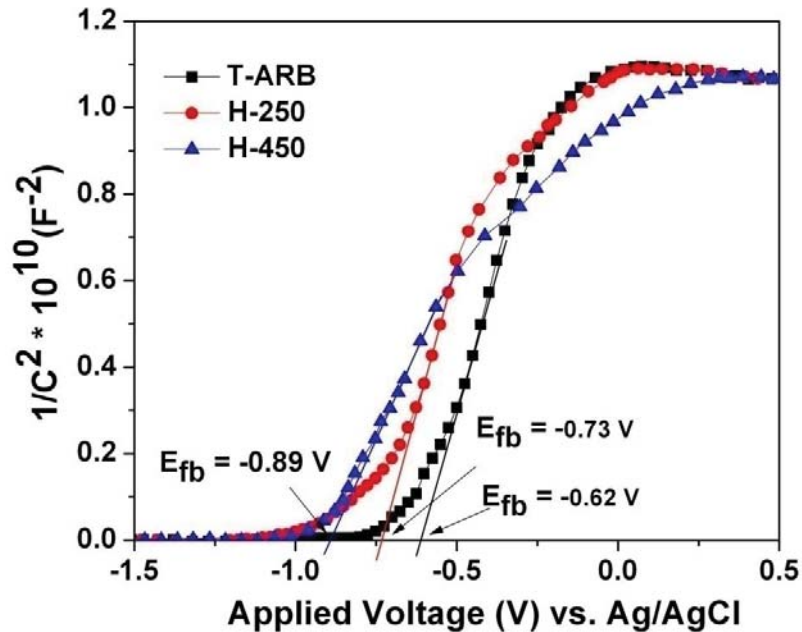


Figure 6.2 MS plots of T-ARB and hydrogenated TiO₂ in 0.5M Na₂SO₄ at a frequency of 1 KHz, under UV illumination

All samples exhibit a positive slope in MS plots, as expected for n-type semiconductors. The observed cathodic shift in E_{fb} is in the order H-450 > H-250 > T-11. It is already discussed in previous chapters that when TiO₂ is irradiated, the upward shift of the FL enhances the charge separation at the semiconductor/electrolyte interface leading higher degree of band bending at the TiO₂ surface compared to that in dark. The electrons in CB and holes in the VB take part in the redox reaction^{218,246}. It is already proved in our previous discussion that more the phase junctions more the band bending (E_{fb}) and hence better charge separation. In addition to that, the Ti³⁺ defects states (ascertained from EPR analysis in following section) generated due to hydrogen annealing lead to the facile transfer of

charge carriers from one phase to another reducing their recombination thereby increasing their life time. This further shifts the FL towards CB edge leading to higher E_{fb} . The MS results clearly indicate that the charge separation is better in H-450 compared to H-250 and T-ARB, leading to higher hydrogen generation efficiency as observed in Figure 6.1.

6.4 Energy Band Alignment and Charge Transfer Pathway in Hydrogenated Triphase TiO₂ Nanotubes

6.4.1 XPS and UPS analysis

To investigate the change in surface bonding of TiO₂ nanotubes induced by hydrogenation, XPS analysis was performed and is depicted in Figure 6.3. The Ti 2*p* core level spectrum of T-ARB showed two peaks centered at binding energies 458.6 and 464.1 eV, corresponding to the Ti 2*p*_{3/2} and Ti 2*p*_{1/2} core levels, respectively, of Ti⁴⁺ species. Our observation is in agreement with the reported literature^{204,263}. The spectrum remains unaltered upon hydrogenation as noticed in Figure 6.3a. The O 1*s* spectra of pristine TiO₂ centered around 529.8 eV corresponding to the lattice oxygen is observed as shown in Figure 6.3b. However the hydrogenated samples exhibit broader O 1*s* spectra with an additional shoulder at higher binding energy compared to that of pristine TiO₂. The O 1*s* spectra of H-250 and H-450 can be deconvoluted into two peaks centered at 529.8 and 531 eV. The shoulder peak at 531 eV is attributed to surface hydroxyl group (Ti-OH)¹⁶. The O 1*s* spectra analysis confirms the formation of hydroxyl group on triphase TiO₂ surface. The quantity of OH species varies with respect to hydrogenation temperature. Some literatures mention that the hydrogenation of titania has effect on its CB^{218,270} while VB offset remains unaltered and the other few reported the effect to be in reverse^{143,233}. In order to identify the

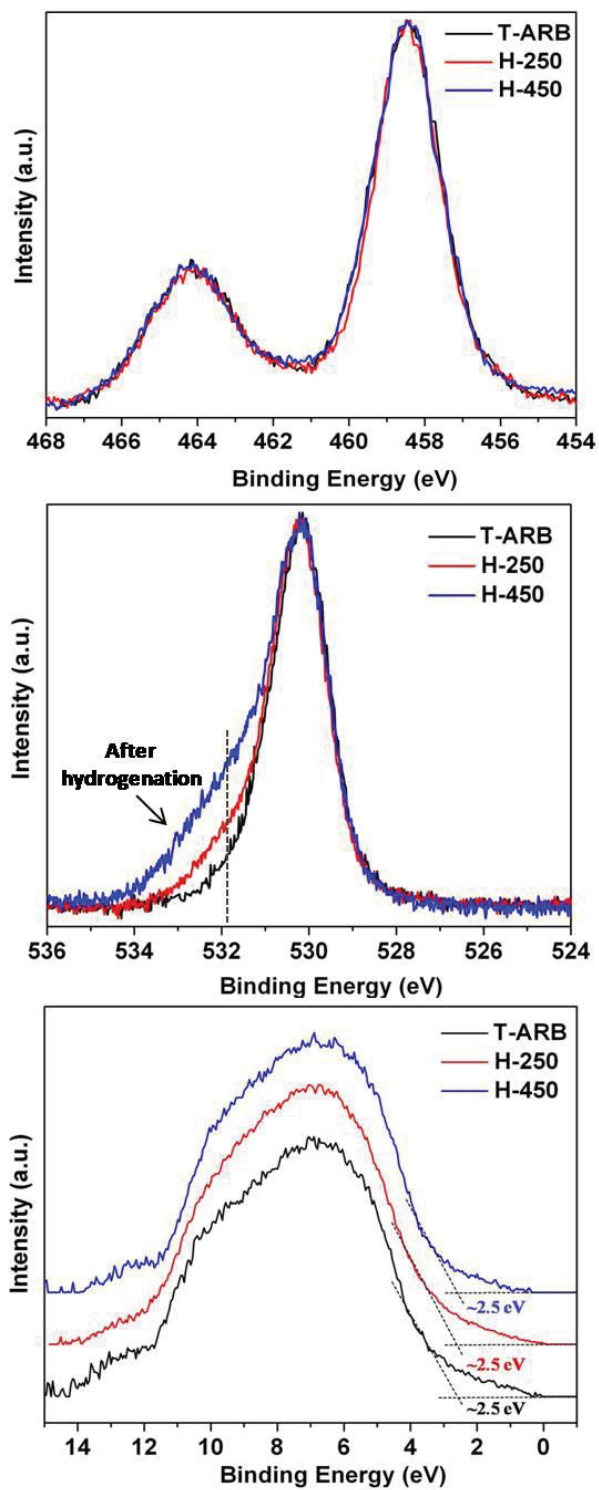


Figure 6.3 (a) Ti 2*p*, (b) O 1*s* and (c) UPS spectra of T-ARB and hydrogenated TiO₂

effect of hydrogenation on VB offsets, UPS analysis was performed for all the samples. Figure 6.3c shows the UPS spectra of both pristine and hydrogenated TiO₂ samples. It is noticed that all the three samples look similar in the leading edge of the VB (low binding energy side) arriving to the conclusion that hydrogenation of TiO₂ having anatase-rutile-brookite phase composition doesn't lead to changes in VB offset. However it is noticed that there is a decrease in band gap of hydrogenated samples from UV-Vis absorbance spectra analysis (Figure 3.20). Therefore it is concluded that the hydrogenation leads to the changes in CB offset rather than VB.

6.4.2 Photoluminescence

The PL spectra of pristine and hydrogenated TiO₂ polymorphs are carried out to study the photophysics of the photogenerated charge carriers (Figure 6.4). It is observed from Figure 6.4 that the main emission peak of pristine TiO₂ appears around 3.14 eV which is attributed to the emission of bandgap transition. Whereas, the main emission peak of H-250 and H-450 is shifted to 2.9 eV in an average (shown clearly in Inset of Figure 6.4). This may be due to the presence of defect states into the band gap of hydrogenated TiO₂. This is evident from the DRS that the band gap is decreased after hydrogen annealing (Figure 3.20). The PL emission intensity in the band gap region (from 2.7 – 3.4 eV) of hydrogenated TiO₂ are less compared to that of pristine sample, which indicate that the recombination rate of photogenerated electrons and holes had been inhibited considerably in H-250 and H-450, because of the formation of oxygen vacancies which served as electron capture traps, thus enhancing the charge separation significantly²¹². All samples exhibited a secondary peak emission in the region from 1.8 to 2.7 eV. The peak around 2.1 eV is due to oxygen vacancy related defects in addition to the under-coordinated Ti acting as electron traps^{247,248}. The

peak around 2.3 eV is due to the surface defects caused by oxygen deficiency and the associated Ti^{3+} ions²⁴⁸⁻²⁵¹. For pristine TiO_2 , the intensities of secondary peaks are nearly equal to that of main emission peaks (around 3 eV). However, for H-250 and H-450, the relative intensity of the secondary peaks is enhanced remarkably, compared to the main peaks. This demonstrates the formation of oxygen defects in the TiO_2 lattice after hydrogenation.

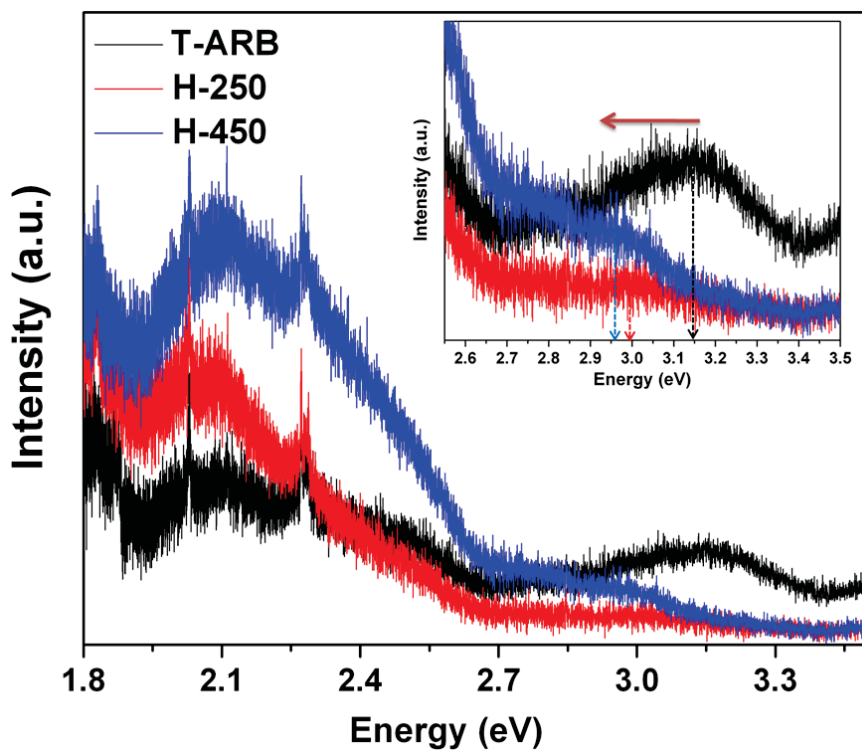


Figure 6.4 PL spectra of T-ARB and hydrogenated TiO_2 (The inset shows the PL spectra in the region from 2.6 to 3.5 eV)

The higher PL intensity of hydrogenated TiO_2 samples in this region compared to pristine TiO_2 even though indicate high radiative recombination of charge pairs, the majority of non radiative recombination that releases phonons is a major pathway for the photogenerated charge annihilation in TiO_2 (as in indirect band gap semiconductors)¹⁴⁶. It is seen already

that these slightly hydrogenated TiO₂ possess better photocatalytic activity compared to pristine TiO₂. Hence the results demonstrate that the hydrogenated TiO₂ have a lower non-radiative recombination rate compared to pristine T-ARB.

6.4.3 EPR analysis

EPR spectra of all the samples are analyzed (Figure 6.5) to further investigate the concentration and distribution of defects in pristine and hydrogenated TiO₂, as it is highly sensitive to detect paramagnetic species containing unpaired electrons. The EPR analysis is performed at room temperature to detect Ti³⁺ or oxygen vacancies present in the samples. The pristine T-ARB shows a pronounced signal at $g = 2.0131$ which is usually assigned to surface O⁻ species generated from the interaction of O₂ with the surface Ti³⁺ species associated with surface

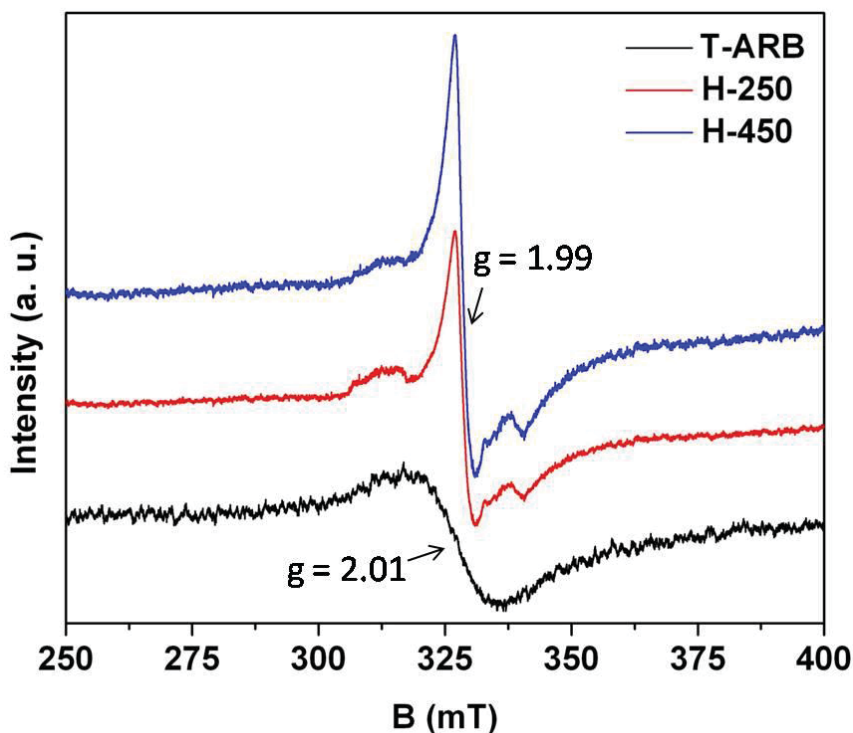


Figure 6.5 EPR spectra of T-ARB and hydrogenated TiO₂

oxygen vacancies²⁴⁵. In H-250, a strong signal is observed at $g = 1.99$ in addition to the surface O^- signal. This strong signal is attributed to the paramagnetic Ti^{3+} defects present in the sample.²⁶⁸ Similarly, it is observed in H-450 that the same signal is enhanced suggesting the presence of large quantity of Ti^{3+} defects compared to H-250. The Ti^{3+} centers are formed due to the elimination of adsorbed oxygen species via the formation of OH species which desorbs from the surface as H_2O at elevated temperatures leaving behind the oxygen vacancies with Ti^{3+} species. It is expected that the signal at $g = 2.0131$ also increases in intensity with respect to hydrogenation temperature as the surface Ti^{3+} generated during hydrogenation, will adsorb O_2 resulting in O^- species on the surface. But in this case it remains the same as that of T-ARB. This indicates that Ti^{3+} is located majorly in the bulk of TiO_2 ²⁴⁵. Therefore it is evident that the hydrogenation leads to the formation of Ti^{3+} in the bulk whose quantity varies proportionally to the hydrogenation temperature as evident from the difference in peak intensity at $g = 1.99$.

6.4.4 Charge transfer mechanism

From UPS analysis (Figure 6.3c), it is clear that there is no change in VB edge. It is also clear that the hydrogenation increased Ti^{3+} defects as confirmed from PL spectra (Figure 6.4) and EPR (Figure 6.5) analysis. Based on the above analysis, the schematic for the effective photocatalytic charge transfer mechanism in H-450 is proposed (Figure 6.6). As our samples are comprised of anatase, rutile and brookite phases, the Ti^{3+} defects are generated in each phase due to hydrogen annealing. This gives rise to the generation of Ti^{3+} defect states below the CB edge of all the three phases as depicted in Figure 6.6. When the sample H-450 is photoexcited, the electrons in each phase either jumps to its CB edge or to its Ti^{3+} defect state depending on the light energy. The electron transfer pathway in triphase

is assumed to be from rutile to anatase to brookite¹⁶⁰ as inspired from the previous analysis of triphase TiO₂ in Chapter 4. Due to the difference in band edge alignment of different phases, the presence of Ti³⁺ defect state in each phase occupies the position such that it will be nearer or equivalent to the CB edge of adjacent phase. Therefore the electrons excited to the Ti³⁺ defect state are preferentially transferred to adjacent phase CB rather than recombining with holes, thus facilitating the

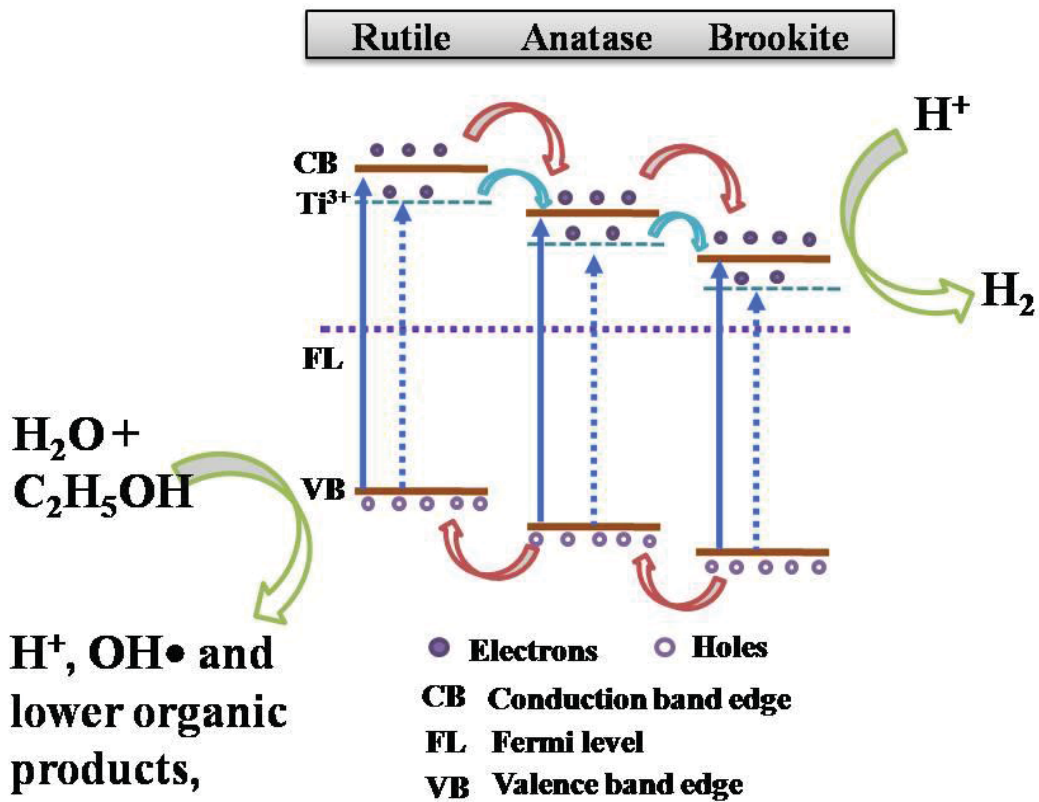


Figure 6.6 Schematic diagram for efficient charge transfer mechanism in H-450

charge transfer. Thus excited electrons in Ti³⁺ state of rutile phase transfers to anatase CB, whereas electrons in Ti³⁺ anatase transfers to brookite CB leading to enhanced life time of charge carriers which will be available for hydrogen generation reactions. In addition the excited electron in the CB of each phase transfers to its adjacent phase. Thus more number

of charge carriers will be available for hydrogen generation reactions. The presence of Ti^{3+} defect states in triphase TiO_2 appears to make a significant difference in catalytic activity. That is why we observe 16 times of hydrogen generation in H-450 compared to pristine triphase TiO_2 (T-ARB) despite the samples being only slightly hydrogenated.

6.5 Summary

In summary, the enhancement in photocatalytic reactivity is noticed in TiO_2 nanotubes annealed in hydrogen at different temperatures. The triphase TiO_2 sample annealed at 450 °C is best at its efficiency generating around 16 times of hydrogen under one sun condition and 50 times of hydrogen under visible light irradiation than that of pristine TiO_2 . The above results show that the slightly hydrogenated triphase TiO_2 nanotubes can, without the need of a cocatalyst, be intrinsically activated to have high H_2 evolution rate in photocatalytic hydrogen generation. This is due to the presence of generated defect states below the CB edge of each phase facilitating the easy transfer of excited electrons to the neighbor phase CB without recombining, as well as making it visible light active. In general the present findings imply that an optimal hydrogen treatment of multiphase TiO_2 nanotubes can result in high quantum efficient visible light active photocatalyst. These investigations might provide new insights into the photocatalytic ability of hydrogenated triphase TiO_2 and pave way for further studies on defective triphase metal oxides for visible light photocatalytic applications.

Summary and Scope of Future Work

In the previous chapters, the synthesis of triphase TiO₂ nanotubes and its nitrogen doped and hydrogenated variants are discussed in detail. In addition, their photocatalytic efficiencies in water splitting to generate hydrogen are thoroughly analyzed. Similarly, their charge transfer characteristics are also delineated. The present chapter summarizes the important results of the previous chapters. At the end of the chapter, the scope of future work is suggested.

7.1 Conclusions

The present thesis reports a novel synthesis method of band gap engineered triphase TiO₂ nanotubes and their potential application in photocatalytic hydrogen generation. The influence of experimental parameters such as change in synthesis voltage and electrolyte concentration, nitrogen doping and hydrogen annealing on structure, morphology, phase composition and photocatalytic efficiency of triphase TiO₂ nanotubes are discussed in detail in the previous chapters. The key results are summarized below:

1. Using Rapid Breakdown Anodization (RBA) technique, a simple and novel method, single, biphasic and triphase TiO₂ nanotubes are synthesized. Increase in synthesis potential results in phase evolution from single phase (anatase) to biphasic (AR) to triphase (ARB) in TiO₂ nanotubes. Similarly, the increase in electrolyte concentration results in phase transformation from triphase (ARB) to biphasic (AB) TiO₂ nanotubes. Doping of nitrogen into the triphase TiO₂ nanotubes resulted in phase transformation from triphase (ARB) to biphasic (AR) composition with increase in nitrogen content. However, hydrogen annealing of triphase TiO₂ nanotubes until 450 °C didn't induce any phase transformation rather it enhanced the crystallinity. Thus it is concluded that the synthesis of triphase TiO₂ nanotubes is highly sensitive to experimental conditions leading to variation in phase composition and crystallinity.

2. In all the sample variants, all the phases are present in each nanotube giving rise to bulk and surface heterojunctions. The obtained TiO₂ nanotubes are in the size range of 30 to 120 nm. The presence of all the three phases in single entity provides enhanced charge transfer

among the phases, which in turn enhances the water splitting reaction generating more hydrogen.

3. The band gap of TiO₂ nanotubes and its variants, obtained using different synthesis voltage and electrolyte concentration, is found to be independent of phase composition, thus possessing nearly same range of value. Hence the difference in photocatalytic hydrogen generation activity observed among the synthesized TiO₂ samples are not due to absorption phenomena rather it solely depends on phase composition. On the other hand, the band gap decreases with increase in nitrogen doping in triphase TiO₂ nanotubes from 3.06 to 2.87 eV thus extending its absorption tail to visible region. Similarly, the band gap of hydrogenated TiO₂ also decreases from 3.1 to 2.95 eV. Thus the adopted modifications such as nitrogen doping and hydrogenation resulted in extension of the absorption tail of the triphase TiO₂ nanotubes, making them visible light active.

4. In photocatalytic hydrogen generation under solar illumination, the synthesized triphase TiO₂ nanotubes are found to be 1.6 times efficient than that of biphasic (anatase-rutile) nanotubes, 1.25 times that of anatase-brookite nanotubes and twice that of anatase TiO₂ nanotubes. Thus more number of phases (triphase) in a single entity (nanotube) enhances the photo excited charge transfer and separation leading to more hydrogen generation. Similarly, the best sample among the synthesized nitrogen doped triphase TiO₂ nanotubes showed around 7.5 times better hydrogen generation efficiency than that of pristine triphase TiO₂ nanotubes and around 2.5 times that of nitrogen doped anatase-rutile nanotubes under one sun illumination. The hydrogen generation efficiency obtained by the best sample among hydrogenated triphase TiO₂ nanotubes is found to be 16 times more efficient than that of

pristine triphase TiO₂ nanotubes under one sun illumination. Thus the hydrogen generation by solar water splitting is enhanced in multiple folds due to band engineering of TiO₂ by introducing three phase junctions as well as by adding defect states into the band gap of triphase TiO₂. It is found that, among the modifications adopted to obtain visible light activity in triphase TiO₂, hydrogenation is found to be a better method for enhancing the photocatalytic activity compared to nitrogen doping. This is due to the presence of minimal recombination centres compared to that in N-TiO₂.

5. In addition to the investigation of photocatalytic efficiency of triphase TiO₂ nanotubes, its charge transfer characteristics are also studied. For the first time, a band diagram is proposed for ARB system with the possible electron transfer pathway using PL spectra and synchrotron VB edge analysis. It is found that the photoexcited charge transfer takes place from rutile to anatase to brookite in triphase TiO₂. The introduction of defect states into the band gap of triphase TiO₂ enhances the charge separation because of low energy difference among defect states and the band edges leading to enhanced hydrogen generation as in the case of nitrogen doped and hydrogenated TiO₂.

Thus the thesis work opens up a new route for the synthesis of band engineered triphase TiO₂ nanotubes and its potential application in solar hydrogen generation in comparison with the widely studied biphasic and single phase TiO₂.

7.2 Future aspects

The literature on triphase TiO₂ nanotubes for any applications is limited. This is mainly because of the constraints on its synthesis as it requires stringent experimental conditions and also due to the high sensitivity of triphase form of TiO₂ which induces phase

change. In view of the above, the present thesis work that introduced the simple technique for the facile synthesis of triphase TiO_2 in nanotubular form is of high significance. It is also proved that the triphase TiO_2 nanotubes can perform better compared to conventional biphasic and single phase TiO_2 . In addition, the basic modifications carried out to enhance the visible light activity of these triphase nanotubes, proved to enhance hydrogen generation in many folds. Even though the thesis work covers all the basic areas to understand the triphase TiO_2 , still it has lot of scope for improvement. The following are the suggestions:

1. The triphase TiO_2 and its variants synthesized by RBA technique can be utilized in other applications such as Dye Sensitized Solar Cells (DSSC), degradation of organic pollutants, dye degradation, biomedical applications such as antibacterial activity etc, in place of conventional biphasic and single phase TiO_2 .
2. The triphase system can be doped / loaded with other elements such as metals, non-metals, quantum dots etc to study the photocatalytic efficiency and its effect on phase composition.
3. The triphase TiO_2 can be merged with other suitable semiconductors or with few layer 2D nanosheets such as graphene, graphitic carbon nitride, molybdenum bisulfide etc. for enhancing the water splitting ability.
4. Apart from engineering the triphase TiO_2 nanotubes for photocatalytic applications, the basic studies such as crystal properties, lifetime of charge carriers, interface structure, band alignment and charge transfer properties etc can be carried out in detail using suitable experimental techniques such as synchrotron based XRD, XAFS, XANES; time resolved spectroscopic techniques, positron annihilation spectroscopy, etc.

5. In addition, theoretical modeling of triphase system can be carried out to compare the difference between the theoretical and the experimental results, for a deep understanding.

Thus there is lot of scope for improving this material in order to obtain a practicable photocatalyst.

References

1. Johnston, B., *et al.*, *Technovation* (2005) **25** (6), 569
2. Ball, M., and Wietschel, M., *International Journal of Hydrogen Energy* (2009) **34** (2), 615
3. Dunn, S., *International Journal of Hydrogen Energy* (2002) **27** (3), 235
4. Momirlan, M., and Veziroglu, T. N., *International Journal of Hydrogen Energy* (2005) **30** (7), 795
5. Grimes, C. A., *et al.*, Hydrogen Generation by Water Splitting. In *Light, Water, Hydrogen: The Solar Generation of Hydrogen by Water Photoelectrolysis*, Grimes, C. A., *et al.*, (eds.) Springer US, Boston, MA, (2008), pp 35
6. Hou, Z., *et al.*, *International Journal of Hydrogen Energy* (2006) **31** (5), 555
7. Hotza, D., and Diniz da Costa, J. C., *International Journal of Hydrogen Energy* (2008) **33** (19), 4915
8. Solomon, B. D., and Banerjee, A., *Energy Policy* (2006) **34** (7), 781
9. Gaya, U. I., and Abdullah, A. H., *Journal of Photochemistry and Photobiology C: Photochemistry Reviews* (2008) **9** (1), 1
10. Kudo, A., and Miseki, Y., *Chemical Society Reviews* (2009) **38** (1), 253
11. Navarro Yerga, R. M., *et al.*, *ChemSusChem* (2009) **2** (6), 471
12. Rajeshwar, K., *J. Appl. Electrochem.* (1985) **15** (1), 1
13. Rajeshwar, K., *Journal of Applied Electrochemistry* (2007) **37** (7), 765
14. Emeline, A. V., *et al.*, *The Journal of Physical Chemistry B* (2005) **109** (39), 18515
15. Matsumoto, Y., *J. Solid State Chem.* (1996) **126** (2), 227
16. Preethi, L. K., *et al.*, *International Journal of Hydrogen Energy* (2016) **41** (14), 5865
17. Melvin, A. A., *et al.*, *Nanoscale* (2015) **7** (32), 13477
18. Fujishima, A., and Honda, K., *Nature* (1972) **238** (5358), 37
19. Ni, M., *et al.*, *Renewable and Sustainable Energy Reviews* (2007) **11** (3), 401
20. Fan, Y., *et al.*, *Frontiers of Chemistry in China* (2009) **4** (4), 343
21. Shockley, W., and Queisser, H. J., *Journal of Applied Physics* (1961) **32** (3), 510
22. Navarro Yerga, R. M., *et al.*, Chapter 3 - Hydrogen Production from Water Splitting Using Photo-Semiconductor Catalysts A2 - Gandía, Luis M. In *Renewable Hydrogen Technologies*, Arzamendi, G., and Diéguez, P. M., (eds.) Elsevier, Amsterdam, (2013), pp 43
23. Young, J. L., *et al.*, *Nature Energy* (2017) **2**, 17028
24. Sivaranjani, K., *et al.*, *ChemCatChem* (2014) **6** (2), 522
25. *Advanced Functional Materials* (2009), NA
26. Zhu, L., *et al.*, (2015) **5**, 11609
27. Sun, L., *et al.*, *International Journal of Applied Ceramic Technology*, n/a
28. Wang, F., *et al.*, *The Journal of Physical Chemistry C* (2012) **116** (16), 8901
29. Wang, F., *et al.*, *ChemCatChem* (2012) **4** (4), 476
30. Tamirat, A. G., *et al.*, *Nanoscale Horizons* (2016) **1** (4), 243
31. Luan, P., *et al.*, *Physical Chemistry Chemical Physics* (2015) **17** (7), 5043
32. Sato, J., *et al.*, *Journal of the American Chemical Society* (2005) **127** (12), 4150
33. Gu, Q., *et al.*, *Advanced Materials Interfaces* (2016) **3** (4), 1500631
34. Kang, D., *et al.*, (2017) **2**, 17043

35. Wang, J., *et al.*, *Physical Chemistry Chemical Physics* (2016) **18** (25), 17029
36. Dong, Y., *et al.*, *ACS Sustainable Chemistry & Engineering* (2015) **3** (10), 2429
37. Qiu, F., *et al.*, *Nano Letters* (2016) **16** (9), 5347
38. Sigle, D. O., *et al.*, *The Journal of Physical Chemistry Letters* (2015) **6** (7), 1099
39. Haifeng, S., *et al.*, *Journal of Physics D: Applied Physics* (2009) **42** (12), 125402
40. Hong, Y., *et al.*, *Journal of Materials Chemistry A* (2015) **3** (26), 13913
41. Lee, G.-J., *et al.*, *Renewable Energy* (2016) **89**, 18
42. Tabata, M., *et al.*, *The Journal of Physical Chemistry C* (2010) **114** (25), 11215
43. Hong, E., *et al.*, *Journal of Industrial and Engineering Chemistry* (2014) **20** (5), 3869
44. Han, B., and Hu, Y. H., *Energy Science & Engineering* (2016) **4** (5), 285
45. Nurlaela, E., *et al.*, *Materials for Renewable and Sustainable Energy* (2016) **5** (4), 18
46. Grewe, T., and Tüysüz, H., *ACS Applied Materials & Interfaces* (2015) **7** (41), 23153
47. Kato, H., and Kudo, A., *Catalysis Today* (2003) **78** (1), 561
48. Saito, K., *et al.*, *Dalton Transactions* (2011) **40** (15), 3909
49. Garcia-Esparza, A. T., *et al.*, *ChemSusChem* (2013) **6** (1), 168
50. Ikeda, S., *et al.*, *Catal Lett* (2004) **98** (4), 229
51. Wang, W., *et al.*, *Chemical Society Reviews* (2015) **44** (15), 5371
52. Hartley, C. L., *et al.*, *Inorganic Chemistry* (2016) **55** (17), 8865
53. Eckenhoff, W. T., *et al.*, *Biochimica et Biophysica Acta (BBA) - Bioenergetics* (2013) **1827** (8), 958
54. Kumar, S. G., and Devi, L. G., *The Journal of Physical Chemistry A* (2011) **115** (46), 13211
55. Hanaor, D. A. H., and Sorrell, C. C., *Journal of Materials Science* (2011) **46** (4), 855
56. Antony, R. P., *et al.*, *Int. J. Hydrogen Energy* (2012) **37** (10), 8268
57. Naldoni, A., *et al.*, *Ultrason. Sonochem.* (2013) **20** (1), 445
58. Zhao, B., *et al.*, *Chem. Commun.* (2009) (34), 5115
59. Di Paola, A., *et al.*, *Catalysts* (2013) **3** (1), 36
60. Dubrovinskaia, N. A., *et al.*, *Physical Review Letters* (2001) **87** (27), 275501
61. Muscat, J., *et al.*, *Physical Review B* (2002) **65** (22), 224112
62. Arlt, T., *et al.*, *Physical Review B* (2000) **61** (21), 14414
63. Ren, R., *et al.*, *Journal of Materials Science* (2000) **35** (23), 6015
64. Valeria, C. F., *et al.*, *J. Phys.: Condens. Matter* (2013) **25** (11), 115304
65. Reidy, D. J., *et al.*, *Journal of the European Ceramic Society* (2006) **26** (9), 1527
66. Riyas, S., *et al.*, *Advances in Applied Ceramics* (2007) **106** (5), 255
67. Janes, R., *et al.*, *Dyes and Pigments* (2004) **62** (3), 199
68. Hakan Gürel, H., *et al.*, Modelling of Heterostructures for Low Dimensional Devices. In *Low-Dimensional and Nanostructured Materials and Devices: Properties, Synthesis, Characterization, Modelling and Applications*, Ünlü, H., *et al.*, (eds.) Springer International Publishing, Cham, (2016), pp 1
69. Oskam, G., *et al.*, *The Journal of Physical Chemistry B* (2003) **107** (8), 1734
70. Zhang, H., and F. Banfield, J., *Journal of Materials Chemistry* (1998) **8** (9), 2073
71. Mills, A., *et al.*, *Chem. Soc. Rev.* (1993) **22** (6), 417
72. Anandan, S., and Yoon, M., *Journal of Photochemistry and Photobiology C: Photochemistry Reviews* (2003) **4** (1), 5

73. Hoffmann, M. R., *et al.*, *Chemical Reviews* (1995) **95** (1), 69
74. Chen, X., and Mao, S. S., *Chemical Reviews* (2007) **107** (7), 2891
75. Luo, J., *et al.*, *Sol. Energy Mater. Sol. Cells* (2010) **94** (3), 501
76. Hafez, H. S., *Mater. Lett.* (2009) **63** (17), 1471
77. Guo, S., *et al.*, *Catal. Commun.* (2009) **10** (13), 1766
78. Atabaev, T. S., *et al.*, *Results in Physics* (2016) **6**, 373
79. Fang, W. Q., *et al.*, *Chemistry – A European Journal* (2014) **20** (36), 11439
80. Preethi, L. K., *et al.*, *Applied Catalysis B: Environmental* (2017) **218**, 9
81. Cai, J., *et al.*, *ACS Applied Materials & Interfaces* (2015) **7** (6), 3764
82. Avasare, V., *et al.*, *International Journal of Energy Research* (2015) **39** (12), 1714
83. Tiginyanu, I. M., *et al.*, 3.11 - Nanostructures of Metal Oxides A2 - Bhattacharya, Pallab. In *Comprehensive Semiconductor Science and Technology*, Fornari, R., and Kamimura, H., (eds.) Elsevier, Amsterdam, (2011), pp 396
84. Mandal, S. S., and Bhattacharyya, A. J., *Talanta* (2010) **82** (3), 876
85. Zhang, X., *et al.*, *Water Research* (2009) **43** (5), 1179
86. Liu, X., *et al.*, *Materials Science and Engineering: A* (2002) **326** (2), 235
87. Qu, Y., *et al.*, *Applied Surface Science* (2010) **257** (1), 151
88. Sangchay, W., *et al.*, *Procedia Engineering* (2012) **32**, 590
89. Vinodgopal, K., and Kamat, P. V., *Solar Energy Materials and Solar Cells* (1995) **38** (1), 401
90. Kontos, A. I., *et al.*, *Thin Solid Films* (2007) **515** (18), 7370
91. Ubonchonlakate, K., *et al.*, *Procedia Engineering* (2012) **32**, 656
92. Guo, Y., *et al.*, *Thin Solid Films* (2007) **515** (18), 7117
93. Lee, H., *et al.*, *Powder Technology* (2011) **214** (1), 64
94. Chen, Y.-C., *et al.*, *Water Research* (2011) **45** (14), 4131
95. Zhao, C., *et al.*, *Applied Surface Science* (2006) **252** (20), 7415
96. Manera, M. G., *et al.*, *Sensors and Actuators B: Chemical* (2012) **161** (1), 869
97. Yoo, K. S., *et al.*, *Catalysis Communications* (2005) **6** (4), 259
98. Babu, V. J., *et al.*, *Materials Letters* (2011) **65** (19), 3064
99. Seo, H. O., *et al.*, *Radiation Physics and Chemistry* (2012) **81** (3), 290
100. Mitchell, D. R. G., *et al.*, *Thin Solid Films* (2003) **441** (1), 85
101. Antony, R. P., *et al.*, *J. Solid State Chem.* (2011) **184** (3), 624
102. Antony, R. P., *et al.*, *The Journal of Physical Chemistry C* (2012) **116** (31), 16740
103. Li, J., *et al.*, *Analytica Chimica Acta* (2008) **625** (1), 63
104. Moriguchi, I., *et al.*, *Solid State Ionics* (2005) **176** (31), 2361
105. Liang, H., *et al.*, *Journal of Rare Earths* (2009) **27** (3), 425
106. Fang, J., *et al.*, *Applied Surface Science* (1997) **119** (3), 237
107. Lee, K.-M., *et al.*, *Solar Energy Materials and Solar Cells* (2009) **93** (11), 2003
108. Thiruvengkatachari, R., *et al.*, *Korean Journal of Chemical Engineering* (2008) **25** (1), 64
109. Saadoun, L., *et al.*, *Applied Catalysis B: Environmental* (1999) **21** (4), 269
110. Carp, O., *et al.*, *Progress in Solid State Chemistry* (2004) **32** (1), 33
111. Bard, A. J., *The Journal of Physical Chemistry* (1982) **86** (2), 172
112. Linsebigler, A. L., *et al.*, *Chemical Reviews* (1995) **95** (3), 735
113. Nada, A. A., *et al.*, *International Journal of Hydrogen Energy* (2005) **30** (7), 687
114. Kawai, T., and Sakata, T., *Nature* (1979) **282** (5736), 283

115. Chen, X., *et al.*, *Chemical Reviews* (2010) **110** (11), 6503
116. Piskunov, S., *et al.*, *The Journal of Physical Chemistry C* (2015) **119** (32), 18686
117. Wang, M. C., *et al.*, *Journal of Alloys and Compounds* (2009) **473** (1), 394
118. Dholam, R., *et al.*, *International Journal of Hydrogen Energy* (2009) **34** (13), 5337
119. Takaoka, G. H., *et al.*, *Vacuum* (2008) **83** (3), 679
120. Sadanandam, G., *et al.*, *International Journal of Hydrogen Energy* (2013) **38** (23), 9655
121. Wang, L., *et al.*, *Journal of Saudi Chemical Society* (2015) **19** (5), 595
122. Wenfang, Z., *et al.*, *Journal of Physics D: Applied Physics* (2010) **43** (3), 035301
123. Tian, M., *et al.*, *International Journal of Hydrogen Energy* (2014) **39** (25), 13448
124. Liu, Y., *et al.*, *Journal of Nanoscience and Nanotechnology* (2009) **9** (2), 1514
125. Liu, Q., *et al.*, *International Journal of Hydrogen Energy* (2015) **40** (5), 2107
126. Shin, S. W., *et al.*, *The Journal of Physical Chemistry C* (2015) **119** (24), 13375
127. Yang, Y., *et al.*, *RSC Advances* (2015) **5** (113), 93635
128. Quesada-González, M., *et al.*, *ACS Applied Materials & Interfaces* (2016) **8** (38), 25024
129. Long, R., and English, N. J., *Physical Review B* (2011) **83** (15), 155209
130. Borgarello, E., *et al.*, *Journal of the American Chemical Society* (1982) **104** (11), 2996
131. Ibhaddon, A., and Fitzpatrick, P., *Catalysts* (2013) **3** (1), 189
132. Long, R., and English, N. J., *Applied Physics Letters* (2009) **94** (13), 132102
133. Long, R., and English, N. J., *Chemical Physics Letters* (2009) **478** (4), 175
134. Wang, Y., *et al.*, *The Journal of Physical Chemistry C* (2008) **112** (17), 6620
135. Gai, Y., *et al.*, *Physical Review Letters* (2009) **102** (3), 036402
136. Bettinelli, M., *et al.*, *Journal of Hazardous Materials* (2007) **146** (3), 529
137. Han, X., and Shao, G., *The Journal of Physical Chemistry C* (2011) **115** (16), 8274
138. Yu, C., and Yu, J. C., *Catal Lett* (2009) **129** (3), 462
139. Sakai, Y. W., *et al.*, *Vacuum* (2008) **83** (3), 683
140. Asahi, R., *et al.*, *Science* (2001) **293** (5528), 269
141. Irie, H., *et al.*, *The Journal of Physical Chemistry B* (2003) **107** (23), 5483
142. Ihara, T., *et al.*, *Applied Catalysis B: Environmental* (2003) **42** (4), 403
143. Chen, X., *et al.*, *Science* (2011) **331** (6018), 746
144. Chen, X., *et al.*, *Chemical Society Reviews* (2015) **44** (7), 1861
145. Liu, N., *et al.*, *Nano Lett* (2014) **14** (6), 3309
146. Yan, Y., *et al.*, *Journal of Materials Chemistry A* (2014) **2** (32), 12708
147. Cui, H., *et al.*, *Journal of Materials Chemistry A* (2014) **2** (23), 8612
148. Diebold, U., *Surface Science Reports* (2003) **48** (5–8), 53
149. Zhang, C., *et al.*, *The Journal of Physical Chemistry C* (2012) **116** (37), 19807
150. Cai, M., *et al.*, *Journal of Materials Chemistry A* (2013) **1** (15), 4885
151. Wang, Y., *et al.*, *Applied Catalysis B: Environmental* (2011) **104** (3–4), 268
152. Feng, C., *et al.*, *Applied Catalysis B: Environmental* (2012) **113**, 61
153. Charanpahari, A., *et al.*, *Applied Catalysis A: General* (2012) **443**, 96
154. Zhang, P., *et al.*, *Journal of Hazardous Materials* (2012) **237**, 331
155. Zhang, Z., *et al.*, *Journal of Hazardous Materials* (2008) **158** (2), 517
156. Yang, M., *et al.*, *Applied Catalysis A: General* (2012) **433**, 26
157. Wang, Y., *et al.*, *Catalysis Science & Technology* (2013) **3** (7), 1703

158. Kamat, P. V., *The Journal of Physical Chemistry Letters* (2012) **3** (5), 663
159. Licht, S., *The Journal of Physical Chemistry B* (2001) **105** (27), 6281
160. Kaplan, R., *et al.*, *Applied Catalysis B: Environmental* (2016) **181**, 465
161. Li, G., and Gray, K. A., *Chem. Phys.* (2007) **339** (1–3), 173
162. Zhao, H., *et al.*, *Journal of Materials Chemistry A* (2013) **1** (28), 8209
163. Mutuma, B. K., *et al.*, *J. Colloid Interface Sci.* (2015) **442**, 1
164. Xu, H., and Zhang, L., *The Journal of Physical Chemistry C* (2009) **113** (5), 1785
165. Li, W., *et al.*, *The Journal of Physical Chemistry C* (2008) **112** (51), 20539
166. Bickley, R. I., *et al.*, *Journal of Solid State Chemistry* (1991) **92** (1), 178
167. Hurum, D. C., *et al.*, *The Journal of Physical Chemistry B* (2003) **107** (19), 4545
168. Scotti, R., *et al.*, *Chemistry of Materials* (2008) **20** (12), 4051
169. Puddu, V., *et al.*, *Applied Catalysis B: Environmental* (2010) **94** (3), 211
170. Leghari, S. A. K., *et al.*, *Chemical Engineering Journal* (2011) **166** (3), 906
171. Zhang, Y., *et al.*, *Catal Lett* (2010) **139** (3), 129
172. Fehse, M., *et al.*, *Journal of Power Sources* (2013) **231**, 23
173. Tay, Q., *et al.*, *The Journal of Physical Chemistry C* (2013) **117** (29), 14973
174. Li, G., and Gray, K. A., *Chemistry of Materials* (2007) **19** (5), 1143
175. Shi, L., and Weng, D., *Journal of Environmental Sciences* (2008) **20** (10), 1263
176. Wu, M., *et al.*, *Langmuir* (1999) **15** (26), 8822
177. Shen, X., *et al.*, *Journal of Hazardous Materials* (2011) **192** (2), 651
178. Zachariah, A., *et al.*, *The Journal of Physical Chemistry C* (2008) **112** (30), 11345
179. Bojinova, A., *et al.*, *Materials Chemistry and Physics* (2007) **106** (2), 187
180. Liao, Y., *et al.*, *Journal of Materials Chemistry* (2012) **22** (16), 7937
181. Mahdjoub, N., *et al.*, *Journal of Photochemistry and Photobiology A: Chemistry* (2010) **210** (2–3), 125
182. Luís, A. M., *et al.*, *Materials Chemistry and Physics* (2011) **125** (1–2), 20
183. Di Paola, A., *et al.*, *Colloids and Surfaces A: Physicochemical and Engineering Aspects* (2008) **317** (1–3), 366
184. Scanlon, D. O., *et al.*, *Nat Mater* (2013) **12** (9), 798
185. Cullity, B. D., and Stock, S. R., *Elements of X-ray Diffraction*. Prentice Hall: 2001
186. Scherrer, P., *Nachrichten von der Gesellschaft der Wissenschaften zu Göttingen* (1918), 98
187. Zhang, H., and Banfield, J. F., *The Journal of Physical Chemistry B* (2000) **104** (15), 3481
188. Raman, C. V., and Krishnan, K. S., *Nature* (1928) **121**, 501
189. Martínez-Castañón, G. A., *et al.*, *Materials Letters* (2005) **59** (4), 529
190. Tauc, J., *Materials Research Bulletin* (1970) **5** (8), 721
191. Tauc, J., *et al.*, *physica status solidi (b)* (1966) **15** (2), 627
192. Radecka, M., *et al.*, *Trends in Inorganic Chemistry* (2006) **9**, 81
193. Murphy, A. B., *Appl. Opt.* (2007) **46** (16), 3133
194. Wooten, F., Chapter 5 - INTERBAND TRANSITIONS. In *Optical Properties of Solids*, Academic Press(1972), pp 108
195. Patra, K. K., and Gopinath, C. S., *ChemCatChem* (2016) **8** (20), 3294
196. Liao, C.-H., *et al.*, *Catalysts* (2012) **2** (4), 490
197. Lopez, T., *et al.*, *Journal of Sol-Gel Science and Technology* (2001) **22** (1), 99
198. Wei, F., *et al.*, *Chemical Engineering Journal* (2008) **144** (1), 119

199. Di Paola, A., *et al.*, *The Journal of Physical Chemistry C* (2009) **113** (34), 15166
200. Zhou, W., *et al.*, *Journal of Materials Chemistry* (2010) **20** (29), 5993
201. Joo, J., *et al.*, *The Journal of Physical Chemistry B* (2005) **109** (32), 15297
202. Bharad, P. A., *et al.*, *Nanoscale* (2015) **7** (25), 11206
203. Antony, R. P., *et al.*, *The Journal of Physical Chemistry C* (2013) **117** (13), 6851
204. Sathish, M., *et al.*, *Chemistry of Materials* (2005) **17** (25), 6349
205. Kiran, V., and Sampath, S., *Nanoscale* (2013) **5** (21), 10646
206. Rahul, T. K., and Sandhyarani, N., *Nanoscale* (2015) **7** (43), 18259
207. Sambandam, B., *et al.*, *ACS Sustainable Chemistry & Engineering* (2015) **3** (7), 1321
208. Yang, G., *et al.*, *J. Mater. Chem.* (2010) **20** (25), 5301
209. Lu, D., *et al.*, *Nanoscale Research Letters* (2014) **9** (1), 272
210. Gai, L., *et al.*, *CrystEngComm* (2012) **14** (22), 7662
211. Choi, W., *et al.*, *The Journal of Physical Chemistry* (1994) **98** (51), 13669
212. Jiang, X., *et al.*, *The Journal of Physical Chemistry C* (2012) **116** (42), 22619
213. Bessergenev, V. G., *et al.*, *Applied Catalysis A: General* (2015) **500**, 40
214. Samiee, M., and Luo, J., *Materials Letters* (2013) **98**, 205
215. Batakrushna, S., *et al.*, *Journal of Physics D: Applied Physics* (2014) **47** (23), 235304
216. Leshuk, T., *et al.*, *ACS Applied Materials & Interfaces* (2013) **5** (6), 1892
217. Liu, N., *et al.*, *Nano Letters* (2014) **14** (6), 3309
218. Wang, G., *et al.*, *Nano Lett.* (2011) **11** (7), 3026
219. Fahim, N. F., and Sekino, T., *Chem. Mater.* (2009) **21** (9), 1967
220. Hahn, R., *et al.*, *Electrochemistry Communications* (2007) **9** (5), 947
221. Swamy, V., *et al.*, *Applied Physics Letters* (2006) **89** (16), 163118
222. Torimoto, T., *et al.*, *Physical Chemistry Chemical Physics* (2002) **4** (23), 5910
223. Madras, G., *et al.*, *Journal of the American Ceramic Society* (2007) **90** (1), 250
224. Li, W., *et al.*, *Journal of Applied Physics* (2004) **96** (11), 6663
225. Wang, C.-C., and Ying, J. Y., *Chemistry of Materials* (1999) **11** (11), 3113
226. Chandana, R., *et al.*, *Journal of Physics D: Applied Physics* (2009) **42** (20), 205101
227. Ye, X., *et al.*, *Nanostructured Materials* (1997) **8** (7), 919
228. Ding, K., *et al.*, *Langmuir* (2010) **26** (12), 10294
229. Gribb, A. A., and Banfield, J. F., *American Mineralogist* (1997) **82** (7-8), 717
230. Penn, R. L., and Banfield, J. F., *American Mineralogist* (1998) **83** (9-10), 1077
231. Choi, H. C., *et al.*, *Vibrational Spectroscopy* (2005) **37** (1), 33
232. Gupta, S. K., *et al.*, *Journal of Raman Spectroscopy* (2010) **41** (3), 350
233. Naldoni, A., *et al.*, *Journal of the American Chemical Society* (2012) **134** (18), 7600
234. Wei-Dong, Z., *et al.*, *Nanotechnology* (2012) **23** (45), 455204
235. Gribb, A. A., and Banfield, J. F., *Am. Mineral.* (1997) **82**, 717
236. Hu, Y., *et al.*, *Journal of the European Ceramic Society* (2003) **23** (5), 691
237. Zhu, S.-C., *et al.*, *Journal of the American Chemical Society* (2015) **137** (35), 11532
238. Zhang, J., *et al.*, *The Journal of Physical Chemistry B* (2006) **110** (2), 927
239. Zhang, W. F., *et al.*, *Journal of Physics D: Applied Physics* (2000) **33** (8), 912
240. Li, J.-G., *et al.*, *The Journal of Physical Chemistry C* (2007) **111** (13), 4969
241. Sivaranjani, K., and Gopinath, C. S., *Journal of Materials Chemistry* (2011) **21** (8), 2639

242. Palomino-Merino, R., *et al.*, *Opt. Mater.* (2015) **46**, 345
243. Zhang, Y., *et al.*, *Journal of the American Ceramic Society* (2011) **94** (12), 4157
244. Jiang, X., *et al.*, *J. Alloys Compd.* (2011) **509** (8), L137
245. Yu, X., *et al.*, *ACS Catalysis* (2013) **3** (11), 2479
246. Bessegato, G. G., *et al.*, Enhancement of Photoelectrocatalysis Efficiency by Using Nanostructured Electrodes. In *Modern Electrochemical Methods in Nano, Surface and Corrosion Science*, Aliofkhaezai, M., (ed.) InTech, Rijeka, (2014), p Ch. 10
247. Vásquez, G. C., *et al.*, *The Journal of Physical Chemistry C* (2013) **117** (4), 1941
248. Mercado, C. C., *et al.*, *The Journal of Physical Chemistry C* (2012) **116** (19), 10796
249. Lei, Y., *et al.*, *Applied Physics Letters* (2001) **78** (8), 1125
250. Ghosh, S., *et al.*, *The Journal of Physical Chemistry C* (2013) **117** (16), 8458
251. Melvin, A. A., *et al.*, *ChemistrySelect* (2016) **1** (5), 917
252. Hongchao, Z., *et al.*, *Nanotechnology* (2014) **25** (27), 275603
253. Daude, N., *et al.*, *Physical Review B* (1977) **15** (6), 3229
254. Lin, H., *et al.*, *Applied Catalysis B: Environmental* (2006) **68** (1–2), 1
255. Grätzel, M., and Rotzinger, F. P., *Chemical Physics Letters* (1985) **118** (5), 474
256. Štengl, V., and Králová, D., *Materials Chemistry and Physics* (2011) **129** (3), 794
257. Reyes-Coronado, D., *et al.*, *Nanotechnology* (2008) **19** (14), 145605
258. Shen, X., *et al.*, *Journal of Materials Science* (2012) **47** (15), 5743
259. Rumaiz, A. K., *et al.*, *Solid State Communications* (2007) **144** (7), 334
260. Kumarasinghe, A. R., *et al.*, *The Journal of Chemical Physics* (2007) **127** (11), 114703
261. Sánchez-Sánchez, C., *et al.*, *Surface Science* (2013) **608**, 92
262. Zhu, J., and Zäch, M., *Current Opinion in Colloid & Interface Science* (2009) **14** (4), 260
263. Naik, B., *et al.*, *The Journal of Physical Chemistry C* (2010) **114** (45), 19473
264. Ketteler, G., *et al.*, *The Journal of Physical Chemistry C* (2007) **111** (23), 8278
265. Wendt, S., *et al.*, *Science* (2008) **320** (5884), 1755
266. Liu, F., *et al.*, *Journal of the American Chemical Society* (2017) **139** (29), 10020
267. Palgrave, R. G., *et al.*, *J. Mater. Chem.* (2009) **19** (44), 8418
268. Zuo, F., *et al.*, *Journal of the American Chemical Society* (2010) **132** (34), 11856
269. Hanzu, I., *et al.*, *ECS Transactions* (2011) **35** (6), 21
270. Wang, Z., *et al.*, *Advanced Functional Materials* (2013) **23** (43), 5444

LIST OF FIGURES

Figure No.	Figure caption	Page No.
1.1	Schematic representation of photocatalytic water splitting	6
1.2	Crystalline structures of (a) anatase, (b) brookite and (c) rutile	10
1.3	Schematic of (i) undoped (ii) cationic and (iii) anionic doped TiO ₂	18
2.1	Schematic of potentiostatic RBA technique	30
2.2	Schematic representation of XRD	31
2.3	Schematic of Raman scattering process	35
2.4	Schematic of the effect of high energy e^- beam interaction with the material	37
2.5	Different modes of TEM	39
2.6	Photoluminescence in direct and indirect band gap semiconductors	44
2.7	Schematic of photoelectron emission	46
2.8	Difference in information depth for XPS and UPS	48
2.9	Energy levels for an electron spin ($m_s = \pm 1/2$) under magnetic field	50
2.10	Band bending of (a) n-type and (b) p-type semiconductor in equilibrium with redox potential of electrolyte.	52
2.11	Effect of varying the applied potential on band edges in the interior of a n-type semiconductor (a) $E > E_{fb}$ (b) $E = E_{fb}$ and (c) $E < E_{fb}$	54
2.12	Photocatalytic hydrogen generation test done under AM 1.5 illumination (100 mW/cm^2) for 10 mg of photocatalyst in 40 ml aqueous ethanol solution	56
3.1	(a) Schematic representation of synthesis of TiO ₂ nanotubes; (b) A tentative reaction route of the synthesis with respect to voltage	65
3.2	XRD patterns of TiO ₂ nanotubes synthesized at different voltages	66
3.3	Synchrotron XRD patterns of TiO ₂ nanotubes synthesized at different voltages	67
3.4	Raman spectra of TiO ₂ photocatalysts synthesized at different voltages.	69
3.5	FESEM images of (a) T-9.5, (b) T-10.2, (c) T-11, (d) T-12, (e) T-15 and (f) the perpendicular view of T-11 nanotubes in which the tubular openings are visible	71
3.6	Bright field images of (a) T-11 and (b) T-12; (c), (d) HRTEM images of T-11	72
3.7	KM plot of TiO ₂ nanotubes synthesized at different voltages	73
3.8	XRD patterns of TiO ₂ nanotubes synthesized at different electrolyte concentration	75
3.9	Raman spectra of TiO ₂ photocatalysts synthesized at different electrolyte concentration	76
3.10	FESEM images of (a) T-0.07, (b) T-0.12 and (c) T-0.15; HRTEM images of	77

	(d) T-0.07, (e) T-0.12 and (f) T-0.15	
3.11	KM plots of TiO ₂ nanotubes synthesized at different electrolyte concentration	79
3.12	XRD patterns of T-ARB and N-TiO ₂ nanotubes	81
3.13	Raman Spectra of T-ARB and N-TiO ₂ nanotubes	83
3.14	FESEM images of T-ARB and selected N-TiO ₂ nanotubes	84
3.15	TEM bright field image: (a) T-ARB and (b) NT-1.5; HRTEM images: (c) T-ARB (d) NT-1.5 and (e) NT-4.5	85
3.16	KM plots of T-ARB and N-TiO ₂ nanotubes	86
3.17	XRD patterns of T-ARB and hydrogenated TiO ₂ nanotubes	88
3.18	Raman Spectra of T-ARB and hydrogenated TiO ₂ nanotubes	90
3.19	FESEM images of (a) T-ARB and (b) H-450; (c) TEM bright field image of T-ARB, (d) HRTEM of single nanotube of T-ARB; HRTEM images of (e) H-250 and (f) H-450; SAED patterns of (g) T-ARB and (h) H-450	91
3.20	UV-Vis absorbance spectra of T-ARB and hydrogenated TiO ₂ nanotubes (Inset: Band gap values calculated from the Kubelka-Munk plots)	92
4.1	Cumulative hydrogen generation of triphasic TiO ₂ synthesized at different voltages under one sun conditions with ethanol as sacrificial agent (The error bars in the figure are standard error values of three tests)	100
4.2	Cumulative hydrogen generation of triphasic TiO ₂ synthesized at different electrolyte concentration under one sun conditions with ethanol as sacrificial agent (The error bars in the figure are standard error values of three tests)	102
4.3	MS plots of TiO ₂ nanotubes synthesized at different voltages in 0.5M Na ₂ SO ₄ at a frequency of 1 KHz, under UV illumination	104
4.4	(a) PL spectra TiO ₂ nanotubes synthesized at different voltages (b) O1s XPS spectra comparison of T-11 and T-12	105
4.5	MS plots of TiO ₂ nanotubes synthesized at different electrolyte concentration in 0.5M Na ₂ SO ₄ at a frequency of 1 KHz, under UV illumination	107
4.6	PL spectra of TiO ₂ nanotubes synthesized at different electrolyte concentration	108
4.7	A close look of the PL spectra in band gap region from 2.6 eV to 3.4 eV	109
4.8	Deconvoluted PL spectra of selected TiO ₂ nanotubes synthesized at different voltages in the region from 2.6 eV to 3.4 eV	111
4.9	Synchrotron photoelectron valence band spectra of T-11	113
4.10	Possible band edge positions of T-11 (a) Case I and (b) Case II	115
5.1	Cumulative hydrogen generation of T-ARB and N-TiO ₂ under one sun conditions with ethanol as sacrificial agent	120
5.2	MS plots of T-ARB and N-TiO ₂ nanotubes in 0.5M Na ₂ SO ₄ at a frequency	122

	of 1 KHz, under UV illumination	
5.3	Deconvolution of (a) Ti 2 <i>p</i> and (b) O 1 <i>s</i> spectra of T-ARB and N-TiO ₂ nanotubes	125
5.4	(a) O 1 <i>s</i> , (b) N 1 <i>s</i> and (c) UPS spectra of T-ARB and N-TiO ₂ nanotubes	127
5.5	PL spectra of T-ARB and N-TiO ₂ nanotubes	129
5.6	Effect of nitrogen doping in triphase TiO ₂ nanotubes	131
5.7	Schematic diagram for efficient charge transfer mechanism in NT-1.5	133
5.8	Synchrotron valence band spectra of (a) T-ARB; and (b) NT-1.5	134
6.1	Cumulative hydrogen generation of T-ARB and hydrogenated TiO ₂ under (a) one sun conditions and (b) visible light with ethanol as sacrificial agent (The error bars in the figure are standard error values of three tests)	140
6.2	MS plots of T-ARB and hydrogenated TiO ₂ in 0.5M Na ₂ SO ₄ at a frequency of 1 KHz, under UV illumination	142
6.3	(a) Ti 2 <i>p</i> , (b) O 1 <i>s</i> and (c) UPS spectra of T-ARB and hydrogenated TiO ₂	144
6.4	PL spectra of T-ARB and hydrogenated TiO ₂ (The inset shows the PL spectra in the region from 2.6 to 3.5 eV)	146
6.5	EPR spectra of T-ARB and hydrogenated TiO ₂	147
6.6	Schematic diagram for efficient charge transfer mechanism in H-450	149

LIST OF TABLES

Table No.	Table caption	Page No.
1.1	Physical and structural properties of anatase, brookite and rutile phases	10
3.1	Quantification and crystallite size of individual phases in TiO ₂ nanotubes synthesized at different voltages	68
3.2	Quantification and crystallite size of individual phases in TiO ₂ nanotubes synthesized at different electrolyte concentration	75
3.3	Quantification and crystallite size of individual phases in T-ARB and N-TiO ₂ nanotubes	81
3.4	Quantification and crystallite size of individual phases in T-ARB and hydrogenated TiO ₂ nanotubes	88
4.1	Deconvoluted peak parameters of PL spectra of selected TiO ₂ nanotubes synthesized at different voltages	111

LIST OF ABBREVIATIONS

CB	Conduction Band
CBM	Conduction Band Maximum
VB	Valence Band
VBM	Valence Band Maximum
FL	Fermi Level
ARB	Anatase-Rutile-Brookite
AR	Anatase-Rutile
AB	Anatase-Brookite
XRD	X-ray Diffraction
TEM	Transmission Electron Microscopy
HRTEM	High Resolution Transmission Electron Microscopy
SAED	Selected Area Electron Diffraction
FESEM	Field Emission Transmission Electron Microscopy
XPS	X-ray Photoelectron Spectroscopy
UV	Ultra-Violet
UPS	Ultra-violet Photoelectron Spectroscopy
PL	Photoluminescence
RBA	Rapid Breakdown Anodization
DC	Direct Current
BSE	Back Scattered Electron
SE	Secondary Electron
E_g	Band Gap
E_k	Kinetic Energy
DRS	Diffuse Reflectance Spectroscopy
KM	Kubelka-Munk
MS	Mott-Schottky
EPR	Electron Paramagnetic Resonance Spectroscopy
E_{fb}	Flatband potential
N-TiO₂	Nitrogen doped TiO ₂